

MATER. TEHNOL.	LETNIK VOLUME	43	ŠTEV. NO.	5	STR. P.	231–274	LJUBLJANA SLOVENIJA	SEP.–OCT. 2009
-------------------	------------------	----	--------------	---	------------	---------	------------------------	-------------------

## VSEBINA – CONTENTS

### *PREGLEDNI ČLANKI – REVIEW ARTICLES*

#### **Finite-difference methods for simulating the solidification of castings**

Simulacija strjevanja z metodo končnih razlik

V. Grozdanič ..... 233

### *IZVIRNI ZNANSTVENI ČLANKI – ORIGINAL SCIENTIFIC ARTICLES*

#### **Pressureless reactive sintering of TiAl-TiC and Ti<sub>3</sub>Al-TiC composites**

Reakcijsko sintranje kompozitov TiAl-TiC in Ti<sub>3</sub>Al-TiC pri atmosferskem tlaku

V. Kevorkijan, S. D. Škapin ..... 239

#### **An optical-emission-spectroscopy characterization of oxygen plasma during the oxidation of aluminium foils**

Karakterizacija kisikove plazme med oksidacijo aluminijevih folij z optično emisijsko spektroskopijo

N. Krstulović, U. Cvelbar, A. Vesel, S. Milošević, M. Mozetič ..... 245

#### **Effect of ageing a two-phase Fe-NiCrMo alloy on the strain hardening at room temperature and at 290 °C**

Vpliv staranja dvofazne zlitine Fe-NiCrMo na deformacijsko utrjevanje pri sobni temperaturi in pri 290 °C

R. Celin, J. Vojvodič Tuma, B. Arzenšek ..... 251

#### **Identification of material properties of quasi-unidirectional carbon-epoxy composite using modal analysis**

Identifikacija materialnih lastnosti za kvazienosmerni kompozit ogljik-epoksi z modalno analizo

R. Zemčik, R. Kottner, V. Laš, T. Plundrich ..... 257

#### **Re-oxidation phenomena during the filtration of steel by means of ceramic filters**

Reoksidacijski procesi med filtriranjem jekla s keramičnimi filtri

K. Stránský, J. Bažan, J. Dobrovská, A. Rek, D. Horáková ..... 261

#### **The use of response surface methodology for prediction and analysis of surface roughness of AISI 4140 steel**

Uporaba metodologije odgovora površine za napoved in analizo hrapavosti pri jeklu AISI 4140

F. Kahraman ..... 267

### *STROKOVNI ČLANKI – PROFESSIONAL ARTICLES*

#### **Determination of optimal ball burnishing parameters for surface hardness**

Določitev optimalnih parametrov krogličnega glajenja za povečanje trdote površine

A. Sagbas, F. Kahraman ..... 271

**17. MEDNARODNA KONFERENCA O MATERIALIH IN TEHNOLOGIJAH, 16. – 18. november, 2009, Portorož, Slovenija**

**17<sup>th</sup> INTERNATIONAL CONFERENCE ON MATERIALS AND TECHNOLOGY, 16–18 November, 2009, Portorož, Slovenia** ..... 275



## FINITE-DIFFERENCE METHODS FOR SIMULATING THE SOLIDIFICATION OF CASTINGS

### SIMULACIJA STRJEVANJA Z METODO KONČNIH RAZLIK

Vladimir Grozdanić

University of Zagreb, Metallurgical Faculty, Aleja narodnih heroja 3, 44103 Sisak, Croatia

Prejem rokopisa – received: 2008-12-15; sprejem za objavo – accepted for publication: 2009-05-12

Mathematical models of casting solidification for different geometrical complexities have been developed and checked. Special emphasis is given to the numerical finite-difference methods for solving the partial differential equations for heat conduction in two- and three-dimensions, which are the basis for the simulation of solidification. In the case of three-dimensional mathematical models, the methods of Douglas and Brian are especially efficient because they are unconditionally stable and of the second order with regard to the approximation of time and space. Both methods have a two-dimensional variant and Brian's method is identical to the implicit alternating direction method. To obtain an algorithm for the solidification with the application of implicit finite-difference methods, the system of the tri-diagonal matrix has to be solved, for which an efficient algorithm exists. In addition to the implicit methods of solving Fourier's partial differential equation of heat conduction, also the unconditionally stable explicit finite-difference methods are used. These are the methods of partial steps, the classical method, and Saul'yev's method. These methods also allow a first-order accuracy. On the basis of the quoted numerical methods for solving the partial differential equation of heat conduction, the algorithms of casting solidification of different complexity have been obtained and programmed in the computer languages ASCII FORTRAN and FORTRAN 77, and the simulation has been performed with a SPERRY 1106 computer and personal computers.

Key words: casting solidification, heat conduction method of finite differences, computer simulation

Razviti in preverjeni so bili matematični modeli za litje in strjevanje z različno geometrično kompleksnostjo. Poseben poudarek je na metodi končnih razlik za rešitev parcialnih diferencialnih enačb za prevajanje toplote v dveh in treh dimenzijah, ki so podlaga za simulacijo strjevanja. V tridimenzionalnem modelu sta posebno učinkoviti metodi po Douglasu in Brianu, ker sta nepogojno stabilni in drugega reda glede na aproksimacijo časa in prostora. Obe metodi imata tudi dvodimenzionalno varianta, Brianova metoda pa je identična z metodo implicitne alternativne diference. Za razvoj algoritma za strjevanje z metodo implicitne končne razlike je treba rešiti problem tridiagonalne matrice, za katero obstaja učinkovit algoritem. Kot dodatek implicitne metode za rešitev Fourierove parcialne diferencialne enačbe za prevajanje toplote se uporabljajo tudi nepogojno stabilne metode končnih razlik. Med njimi so metoda delnih korakov, klasična metoda in Saul'yjeva metoda, ki omogočajo, da se doseže natančnost prvega reda. Na podlagi teh numeričnih metod za rešitev parcialnih diferencialnih enačb za prevajanje toplote so bili razviti algoritmi za litje in strjevanje z različno kompleksnostjo, programirani v računalniških jezikih ASCII FORTRAN in FORTRAN 77, in izvršene simulacije z računalnikom SPERRY 1106 in na osebem računalniku.

Ključne besede: livno strjevanje, prevajanje toplote, metoda končnih razlik, računalniška simulacije

## 1 INTRODUCTION

Mathematical modelling is a scientific method that provides solutions for most foundry problems that have remained unsolved for a long time, e.g., the solidification of castings. This was made possible by the rapid development of computers and numerical methods for solving partial differential equations.

The first step in establishing the mathematical models of solidification is Fourier's partial differential equation of heat conduction. In the domain of casting the equation has been solved by considering the mould geometry and the initial and boundary conditions. During the operationalization of the mathematical model the appropriate numerical methods are used: the finite-element method (FEM) <sup>1-5</sup> and the method of finite differences (FDM) <sup>6-8</sup>. The FEM is more complicated than the FDM, and it is used for castings with a complex geometry and also for curved surfaces. The FDM may be explicit and implicit <sup>9</sup>.

For the explicit FDM the space derivative is formulated in terms of known values, whereas for the implicit FDM the space derivative is in terms of values

that are yet to be computed. The explicit method allows the new value of the dependent variable to be computed essentially with repeated applications of a single formula, whereas the implicit method requires the solution of a system of simultaneous equations.

The "computational molecules" for the explicit and implicit methods are illustrated in **Figure 1**. Circles are

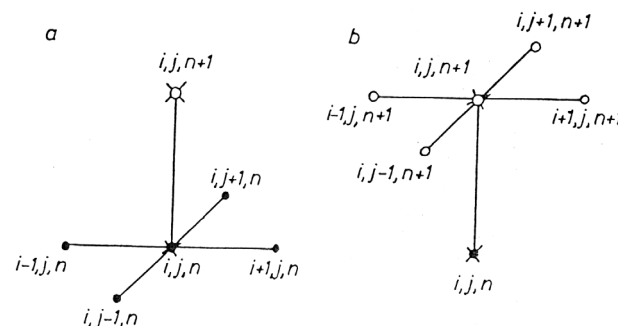


Figure 1: Computational molecules for the a) explicit and b) implicit methods

Slika 1: Računske molekule za a) eksplicitno in b) implicitno metodo

used to denote those temperatures used in formulating the space derivatives, and the crosses for those employed in the time derivative. The full circles denote values already known and the empty circles those about to be computed.

The explicit methods for solving the partial differential equation of heat conduction are usually dependent on the choice of space and time steps and are not unconditionally stable and are preferred at the operationalization of the mathematical models. However, there are some explicit methods that are unconditionally stable as well. In this work a review of the numerical methods to solve a partial differential equation of heat conduction, which has been the most frequently used during the simulation of casting solidification, is given.

## 2 MATHEMATICAL MODELS

The mathematical models of casting solidification consist of the partial differential equation of heat conduction with the appropriate initial and boundary conditions. The partial differential equation of heat conduction in the rectangular coordinate system has the form <sup>10-13</sup>:

$$\frac{\partial T}{\partial t} = a \left( \frac{\partial^2 T}{\partial x^2} + \frac{\partial^2 T}{\partial y^2} + \frac{\partial^2 T}{\partial z^2} \right) \quad (1)$$

In the cylindrical coordinate system <sup>10-13</sup>:

$$\frac{\partial T}{\partial t} = a \left( \frac{\partial^2 T}{\partial r^2} + \frac{\partial T}{r \partial r} + \frac{\partial T}{r^2 \partial \Theta^2} + \frac{\partial^2 T}{\partial z^2} \right) \quad (2)$$

And in the spherical coordinate system <sup>10-13</sup>:

$$\frac{\partial T}{\partial t} = a \left[ \frac{1}{r^2} \frac{\partial}{\partial r} \left( r^2 \frac{\partial T}{\partial r} \right) + \frac{1}{r^2 \sin \theta} \frac{\partial}{\partial \theta} \left( \sin \theta \frac{\partial T}{\partial \theta} \right) + \frac{1}{r^2 \sin^2 \theta} \frac{\partial^2 T}{\partial \varphi^2} \right] \quad (3)$$

The initial conditions were derived on the basis of the system of thermal balance <sup>14</sup>:

$$t = 0 \quad T = T_s$$

$$T_i = \frac{\rho_m C_{pm} T_L + \rho_K C_{pK} T_s + \rho_m \Delta H_f}{\rho_m C_{pm} + \rho_K C_{pK}} \quad (4)$$

The analytical solution of the partial differential equation of heat conduction for the case of the thermal contact of two semi-infinite media is <sup>15</sup>:

$$t = 0 \quad T = T_s$$

$$T_{if} = T_s + \frac{T_L - T_s}{1 + \frac{K_K}{K_m} \sqrt{\frac{a_m}{a_k}}} \quad (5)$$

The boundary conditions are of the fourth kind and in a real complex system the mould-casting core-chill may be written as <sup>15</sup>:

$$K_m \frac{\partial T_m}{\partial n} = K_K \frac{\partial T_K}{\partial n} \quad (6)$$

$$K_m \frac{\partial T_m}{\partial n} = K_j \frac{\partial T_j}{\partial n} \quad (7)$$

$$K_m \frac{\partial T_m}{\partial n} = K_h \frac{\partial T_h}{\partial n} \quad (8)$$

$$K_k \frac{\partial T_K}{\partial n} = K_j \frac{\partial T_j}{\partial n} \quad (9)$$

The thermo-technical properties of a material that depend on the temperature <sup>16-18</sup> and the latent heat of crystallization are incorporated into the equation for the specific heat of the metal (the method of modified specific heat) in the following way:

$$\Delta H_f = \int_{T_s}^{T_l} (c_p^* - c_p) dT \quad (10)$$

## 3 NUMERICAL METHODS

There are two finite-difference methods for solving the three-dimensional differential equation of heat conduction in a non-stationary state: the Douglas method <sup>6</sup> and Brian's method <sup>19</sup>. The first method is a modification of the Crank-Nicolson method <sup>6</sup> that was proposed by Douglas:

$$\frac{1}{2} \partial_x^2 (T_{i,j,k}^* + T_{i,j,k}^n) + \partial_y^2 T_{i,j,k}^n + \partial_z^2 T_{i,j,k}^n = \frac{1}{a_{i,j,k,n}} \frac{T_{i,j,k}^* - T_{i,j,k}^n}{\Delta t} \quad (11)$$

$$\frac{1}{2} \partial_x^2 (T_{i,j,k}^* + T_{i,j,k}^n) + \frac{1}{2} \partial_y^2 (T_{i,j,k}^{**} + T_{i,j,k}^n) + \partial_z^2 T_{i,j,k}^n = \frac{1}{a_{i,j,k,n}} \frac{T_{i,j,k}^{**} - T_{i,j,k}^n}{\Delta t} \quad (12)$$

$$\frac{1}{2} \partial_x^2 (T_{i,j,k}^* + T_{i,j,k}^n) + \frac{1}{2} \partial_y^2 (T_{i,j,k}^{**} + T_{i,j,k}^n) + \frac{1}{2} \partial_z^2 (T_{i,j,k}^{n+1} + T_{i,j,k}^n) = \frac{1}{a_{i,j,k,n}} \frac{T_{i,j,k}^{n+1} - T_{i,j,k}^n}{\Delta t} \quad (13)$$

The second method is a modification of the Douglas-Racford method <sup>20</sup>, and according to Brian it is the most efficient method for the numerical integration of a three-dimensional equation of heat conduction:

$$\partial_x^2 T_{i,j,k}^* + \partial_y^2 T_{i,j,k}^n + \partial_z^2 T_{i,j,k}^n = \frac{1}{a_{i,j,k,n}} \frac{T_{i,j,k}^* - T_{i,j,k}^n}{\Delta t/2} \quad (14)$$

$$\partial_x^2 T_{i,j,k}^* + \partial_y^2 T_{i,j,k}^{**} + \partial_z^2 T_{i,j,k}^n = \frac{1}{a_{i,j,k,n}} \frac{T_{i,j,k}^{**} - T_{i,j,k}^n}{\Delta t/2} \quad (15)$$

$$\partial_x^2 T_{i,j,k}^* + \partial_y^2 T_{i,j,k}^{**} + \partial_z^2 T_{i,j,k}^{***} = \frac{1}{a_{i,j,k,n}} \frac{T_{i,j,k}^{***} - T_{i,j,k}^n}{\Delta t/2} \quad (16)$$

$$\partial_x^2 T_{i,j,k}^* + \partial_y^2 T_{i,j,k}^{**} + \partial_z^2 T_{i,j,k}^{***} = \frac{1}{a_{i,j,k,n}} \frac{T_{i,j,k}^{n+1} - T_{i,j,k}^n}{\Delta t} \quad (17)$$

In practice, Brian recommended the simpler form:

$$\partial_x^2 T_{i,j,k}^* + \partial_y^2 T_{i,j,k}^n + \partial_z^2 T_{i,j,k}^n = \frac{1}{a_{i,j,k,n}} \frac{T_{i,j,k}^* - T_{i,j,k}^n}{\Delta t/2} \quad (18)$$

$$\partial_y^2 T_{i,j,k}^{**} + \partial_z^2 T_{i,j,k}^n = \frac{1}{a_{i,j,k,n}} \frac{T_{i,j,k}^{**} - T_{i,j,k}^n}{\Delta t/2} \quad (19)$$

$$\partial_z^2 T_{i,j,k}^{n+1} + \partial_z^2 T_{i,j,k}^n = \frac{1}{a_{i,j,k,n}} \frac{T_{i,j,k}^{n+1} - T_{i,j,k}^n - 2T_{i,j,k}^{**}}{\Delta t/2} \quad (20)$$

It was proved that Brian's original method can have the following form:

$$\partial_x^2 T_{i,j,k}^* + \partial_y^2 T_{i,j,k}^n + \partial_z^2 T_{i,j,k}^n = \frac{1}{a_{i,j,k,n}} \frac{T_{i,j,k}^* - T_{i,j,k}^n}{\Delta t/2} \quad (21)$$

$$\partial_x^2 T_{i,j,k}^* + \partial_y^2 T_{i,j,k}^{**} + \partial_z^2 T_{i,j,k}^n = \frac{1}{a_{i,j,k,n}} \frac{T_{i,j,k}^{**} - T_{i,j,k}^n}{\Delta t/2} \quad (22)$$

$$\partial_x^2 T_{i,j,k}^* + \partial_y^2 T_{i,j,k}^n + \partial_z^2 T_{i,j,k}^{n+1} = \frac{1}{a_{i,j,k,n}} \frac{T_{i,j,k}^{n+1} - T_{i,j,k}^{**}}{\Delta t/2} \quad (23)$$

The general solution of Brian's modified method for general points  $(i,j,k)$  and the points on the boundary surface between the mould and the metal in a rectangular coordinate system are given in Appendix A.

The methods of Douglas and Brian are unconditionally stable and converge with the discretization error  $O[(\Delta t)^2 + (\Delta x)^2 + (\Delta y)^2 + (\Delta z)^2]$ . Both methods have a two-dimensional option, and Brian's method is identical to the implicit alternating direction (IAD) method.

The IAD method subdivides each  $\Delta t$  into two half-time steps, each of duration of  $\Delta t/2$ . The space derivatives are approximated implicitly in the  $x$ -direction and explicitly in the  $y$ -direction over the first  $\Delta t/2$ ; the procedure is reversed over the second  $\Delta t/2$  – explicitly in the  $x$ -direction and implicitly in the  $y$ -direction. In the rectangular coordinate system it may be written as <sup>14</sup>:

$$\partial_x^2 T_{i,j}^{n+1/2} + \partial_y^2 T_{i,j}^n = \frac{1}{a_{i,j,n}} \frac{T_{i,j}^{n+1/2} - T_{i,j}^n}{\Delta t/2} \quad (24)$$

$$\partial_x^2 T_{i,j}^{n+1/2} + \partial_y^2 T_{i,j}^{n+1} = \frac{1}{a_{i,j,n}} \frac{T_{i,j}^{n+1} - T_{i,j}^{n+1/2}}{\Delta t/2} \quad (25)$$

And in the case of the polar coordinate system as <sup>15</sup>:

$$\partial_r^2 T_{i,j}^n + \frac{T_{i,j+1}^n - T_{i,j-1}^n}{2r_j \Delta r} + \partial_z^2 T_{i,j}^{n+1/2} = \frac{1}{a_{i,j,n}} \frac{T_{i,j}^{n+1/2} - T_{i,j}^n}{\Delta t/2} \quad (26)$$

$$\partial_r^2 T_{i,j}^{n+1} + \frac{T_{i,j+1}^{n+1} - T_{i,j-1}^{n+1}}{2r_j \Delta r} + \partial_z^2 T_{i,j}^{n+1/2} = \frac{1}{a_{i,j,n}} \frac{T_{i,j}^{n+1} - T_{i,j}^{n+1/2}}{\Delta t/2} \quad (27)$$

The implicit alternating direction method is unconditionally stable and is of second order with regard to the discretization of time and space. In parallel with the implicit alternating direction methods, the unconditionally stable explicit methods have been developed: the partial-steps method <sup>7</sup>, the Saul'yev explicit method <sup>6,7,21-28</sup> and the "classical" method <sup>7</sup>. The partial-steps method consists of two steps, which are written as:

$$\frac{T_{i,j}^{n+1/2} - T_{i,j}^n}{\Delta t} = a_{i,j,n} \partial_x^2 T_{i,j}^{n+1/2} \quad (28)$$

$$\frac{T_{i,j}^{n+1} - T_{i,j}^{n+1/2}}{\Delta t} = a_{i,j,n} \partial_y^2 T_{i,j}^{n+1} \quad (29)$$

This method is of the first order in terms of accuracy and with the approximation error  $O[(\Delta t) + (\Delta x)^2 + (\Delta y)^2]$ .

The Saul'yev method is another efficient finite-difference procedure for approximating the solution of the two-dimensional heat-conduction equation. It relies on two explicit equations, to be used in turn over successive time steps. Each equation by itself appears to be "unbalanced", but is in fact the mirror image of the other; thus the two equations may be regarded as complementary to each other. The basic computational molecules are illustrated in **Figure 2**.

From time-level  $n$  to time-level  $n+1$  (**Figure 2a**), the derivatives are approximated as follows:

$$\frac{\partial T}{\partial t} \approx \frac{T_{i,j,n+1} - T_{i,j,n}}{\Delta t} \quad (30)$$

$$\frac{\partial^2 T}{\partial x^2} \approx \frac{T_{i-1,j,n+1} - T_{i,j,n+1} - T_{i,j,n} + T_{i+1,j,n}}{(\Delta x)^2} \quad (31)$$

$$\frac{\partial^2 T}{\partial y^2} \approx \frac{T_{i,j-1,n+1} - T_{i,j,n+1} - T_{i,j,n} + T_{i,j+1,n}}{(\Delta y)^2} \quad (32)$$

This method is also of the first order in terms of accuracy. The last method for solving the two-dimensional differential equation of heat conduction is the "classical" method with the discretization error  $O[(\Delta t) + (\Delta x)^2 + (\Delta y)^2]$ , which may be written as:

$$\frac{T_{i,j}^{n-1} - T_{i,j}^n}{\Delta t} = a_{i,j,n} (\partial_x^2 T_{i,j}^n + \partial_y^2 T_{i,j}^n) \quad (33)$$

$$\frac{T_{i,j}^{n+1} - T_{i,j}^n}{\Delta t} = a_{i,j,n} (\partial_x^2 T_{i,j}^{n+1} + \partial_y^2 T_{i,j}^{n+1}) \quad (34)$$

Based on the quoted numerical methods for solving the partial differential equation of heat conduction, algorithms for the solidification of castings of different complexity have been obtained, as shaped-steel castings (L,T,H), as a low-carbon cast-steel gear blank, as gray iron and a cast-steel flange, a cast-steel valve housing, bars, cylinders, spheres, steel rail-wheel casting, etc. <sup>14,15,29-46</sup>. The algorithms are programmed in the computer languages ASCII FORTRAN and FORTRAN 77, and

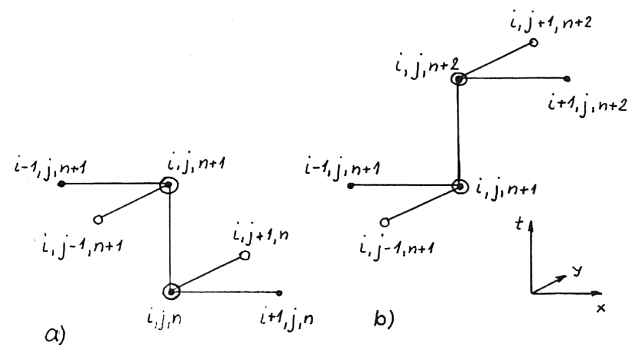


**Figure 2:** Computational molecules for the Saul'yev method. The grid points are marked with crosses, and the full circles and empty circles are used for the time, the  $x$ -direction, and the  $y$ -direction derivatives, respectively.

**Slika 2:** Računske molekule za metodu po Saul'yevu. Mrežne točke označene s križci, polnim i praznim krugovima su uporabljene za čas  $t$  i  $x$ - i  $y$ -derivate.

the simulation is performed on a SPERRY 1106 computer and on personal computers.

#### 4 CONCLUSION

Mathematical models of the casting solidification of different geometrical complexities, which are based on Fourier's differential equation of heat conduction, have been developed and investigated in this paper. To obtain satisfactory results this equation is solved by means of numerical finite-difference methods. In the case of the three-dimensional differential equation of heat conduction, two numerical methods are applied, Douglas's and Brian's, which are unconditionally stable and are of the second order with regard to the time and space approximation. For solving the two-dimensional partial differential equation of heat conduction there are especially efficient implicit alternating direction methods, which are unconditionally stable, and the explicit methods of finite differences: the partial-step method, the "classical" method and the Saul'yev method. In contrast to the implicit alternating direction methods, which are of second order with regard to the time and space approximation, the explicit methods are of first order in terms of accuracy.

#### List of symbols

$a$  – thermal diffusivity  
 $c_p$  – specific heat  
 $c_p^*$  – specific heat in interval of solidification  
 $\Delta H_f$  – latent heat of fusion  
 $K$  – coefficient of heat conduction  
 $n$  – normal  
 $r$  – coordinate  
 $t$  – time  
 $T$  – temperature  
 $T^*, T^{**}$  – successive approximations of  $T$  at the half time-step  
 $x, y, z$  – coordinate  
 Index:  
 $h$  – chill  
 $i$  – coordinate  
 $if$  – temperature on the boundary surface  
 $j$  – coordinate; core  
 $k$  – mould  
 $l$  – pouring; liquidus  
 $m$  – metal  
 $n$  – time step  
 $r$  – coordinate  
 $s$  – sand  
 $f$  – fusion  
 $x, y, z$  – coordinate

#### 5 REFERENCES

- <sup>1</sup> C. S. Krishnamoorthy, Finite Element Analysis, Theory and programming, Tata McGraw-Hill, New Delhi, 1987
- <sup>2</sup> H. R. Schwarz, Finite element methods, Academic Press, London, 1988
- <sup>3</sup> R. H. Gallagher, Finite element analysis, Prentice-Hall, Englewood Cliffs, 1975
- <sup>4</sup> R. W. Lewis, K. Morgan, H. R. Thomas, K. N. Seetharamu, The finite element method in heat transfer analysis, John Wiley, Chichester, 1996
- <sup>5</sup> K. H. Huebner, D. L. Dewhurst, D. E. Smith, T.G. Byrom, The finite element method for engineers, 4th ed., John Wiley, New York, 2001
- <sup>6</sup> B. Carnahan, H. A. Luther, J. O. Wilkes, Applied numerical methods, John Wiley, New York, 1969
- <sup>7</sup> D. A. Anderson, J. C. Tannehill, R. H. Pletcher, Computational fluid mechanics and heat transfer, Hemisphere, Cambridge, 1984
- <sup>8</sup> G. D. Smith, Numerical solution of partial differential equations, University Press, Oxford, 1974
- <sup>9</sup> V. Grozdanić, Metalurgija, 37 (1998) 4, 217–221
- <sup>10</sup> E. R. G. Eckert, R. M. Drake, Analysis of heat and mass transfer, McGraw-Hill Kogakusha, Tokyo, 1972
- <sup>11</sup> J. P. Holman, Heat transfer, 6th ed., McGraw-Hill, Singapore, 1986
- <sup>12</sup> V. P. Isachenko, V. A. Osipova, A. S. Sukomel, Heat transfer, 3rd ed., Mir Publishers, Moscow, 1980
- <sup>13</sup> J. H. Leinhard IV, J. H. Leinhard V, A heat transfer textbook, 3rd ed., Phlogiston Press, Cambridge, 2006
- <sup>14</sup> V. Grozdanić, Ljevarstvo, 34 (1992) 1, 7–11
- <sup>15</sup> V. Grozdanić, J. Črnko, Železarski zbornik, 25 (1991) 4, 149–158
- <sup>16</sup> H. D. Brody, D. Apelian (eds.), Modeling of casting and welding processes, The Metallurgical Society of AIME, Warrendale, 1981
- <sup>17</sup> P. R. Sahn, P. N. Hansen, Numerical simulation and modelling of casting and solidification processes for foundry and cast-house, CIATF, Zurich, 1984
- <sup>18</sup> R. D. Pehlke, A. Jeyarajan, H. Wada, Summary of thermal properties for casting alloys and mold materials, University of Michigan, Ann Arbor, 1982
- <sup>19</sup> P. L. T. Brian, A.I.Ch.E. Journal, 7 (1961) 3, 367
- <sup>20</sup> J. Douglas, H. H. Rachford, Trans. Amer. Math. Soc. 82 (1956), 421
- <sup>21</sup> V. K. Saul'yev, Integration of equations of parabolic type by the method of nets, MacMillan, New York, 1964
- <sup>22</sup> R. Tavakoli, P. Davami, Applied Mathematics and Computation, 181 (2006) 2, 1379–1386
- <sup>23</sup> R. Tavakoli, P. Davami, Applied Mathematics and Computation, 188 (2007) 2, 1184–1192
- <sup>24</sup> M. Dehghan, Applied Mathematics and Computation, 124 (2001) 1, 17–27
- <sup>25</sup> M. Dehghan, Computers and Mathematics with Applications, 43 (2002) 12, 1477–1488
- <sup>26</sup> M. Dehghan, Applied Mathematics and Computation, 167 (2005) 1, 28–45
- <sup>27</sup> M. Dehghan, Applied Mathematics and Computation, 147 (2004) 2, 321–331
- <sup>28</sup> Kazuhiro Fukuyo, Numerical Heat Transfer, Part B: Fundamentals, 52 (2007) 4, 341–352
- <sup>29</sup> V. Grozdanić, Metalurgija, 25 (1986) 2, 51–58
- <sup>30</sup> V. Grozdanić, Ljevarstvo, 5 (1990) 1, 3–13
- <sup>31</sup> V. Grozdanić, V. Novosel-Radović, R. Dmitrović, AFS Transactions, 100 (1992), 265–272
- <sup>32</sup> V. Grozdanić, Slevarenstvi, 40 (1992) 4, 161–162
- <sup>33</sup> V. Grozdanić, Ljevarstvo, 34 (1992) 3, 59–65
- <sup>34</sup> V. Grozdanić, Ljevarstvo, 35 (1993) 3, 59–65
- <sup>35</sup> V. Grozdanić, Metalurgija, 34 (1995) 1–2, 31–34
- <sup>36</sup> V. Grozdanić, Kovine, zlit., tehnol., 29 (1995) 5–6, 537–544
- <sup>37</sup> V. Grozdanić, AFS Transactions, 104 (1996), 9–13
- <sup>38</sup> V. Grozdanić, Metalurgija, 35 (1996) 1, 31–34
- <sup>39</sup> V. Grozdanić, Kovine, zlit., tehnol., 30 (1996) 6, 527–530
- <sup>40</sup> V. Grozdanić, Kovine, zlit., tehnol., 32 (1998) 3–4, 269–271
- <sup>41</sup> V. Grozdanić, Metalurgija, 39 (2000) 4, 285–287
- <sup>42</sup> V. Grozdanić, Mater. tehnol., 36 (2002) 3–4, 139–141
- <sup>43</sup> V. Grozdanić, Mater. tehnol., 38 (2004) 5, 241–243

<sup>44</sup> V. Grozdanić, A. Markotić, Mater. tehnol., 38 (2004) 6, 303–306

<sup>45</sup> V. Grozdanić, A. Markotić, Metalurgija, 43 (2004) 1, 45–48

<sup>46</sup> V. Grozdanić, Metalurgija, 45 (2006) 2, 103–107

**Appendix A.**

General solutions of Brian’s modified method in a rectangular coordinate system.

When the partial differential equations of heat conduction (1), representing the solidification and cooling of steel casting in a sand mould, are approximated by means of Brian’s method, the equations (21), (22) and (23) are obtained. These equations are valid for the general point  $(i,j,k)$  in the mould and casting. In equations (21)–(23),  $a_{i,j,k,n}$  is the temperature diffusivity at the point  $(i,j,k)$  at temperature  $T_{i,j,k}^n$ . The reciprocal value of the Fourier number is:

$$Z_{i,j,k,n} = \frac{(\Delta x)^2}{a_{i,j,k,n} \Delta t} \tag{35}$$

In the case of the equidistant net  $(\Delta x = \Delta y = \Delta z)$ , equations (21), (22) and (23) may be written in the following form:

$$-T_{i-1,j,k}^* + 2(Z_{i,j,k,n} + 1)T_{i,j,k}^* - T_{i+1,j,k}^* = T_{i,j-1,k}^n + T_{i,j+1,k}^n + T_{i,j,k-1}^n + T_{i,j,k+1}^n + 2(Z_{i,j,k,n} - 2)T_{i,j,k}^n \tag{36}$$

$$-T_{i-1,j,k}^{**} + 2(Z_{i,j,k,n} + 1)T_{i,j,k}^{**} - T_{i+1,j,k}^{**} = T_{i-1,j,k}^* - 2T_{i,j,k}^* + T_{i+1,j,k}^* + T_{i,j,k-1}^n + T_{i,j,k+1}^n + 2(Z_{i,j,k,n} - 1)T_{i,j,k}^n \tag{37}$$

$$-T_{i-1,j,k}^{n+1} + 2(Z_{i,j,k,n} + 1)T_{i,j,k}^{n+1} - T_{i+1,j,k}^{n+1} = T_{i-1,j,k}^* - 2T_{i,j,k}^* + T_{i+1,j,k}^* + T_{i,j,k-1}^{**} + T_{i,j,k+1}^{**} + 2(Z_{i,j,k,n} - 1)T_{i,j,k}^{**} \tag{38}$$

Equations (21)–(23) represent the approximation for the net points in the homogeneous rectangle without boundary conditions.

In the case of the boundary interface, a perfect contact between the mould and the metal is assumed. **Figure 3** illustrates the vertical boundary surface YZ between the mould (K) and the metal (M) for an approximation of the value  $T^*$  at the point  $(i,j,k)$ .

By means of the Taylor series, the temperatures  $T_{i-1,j,k}^*$  and  $T_{i+1,j,k}^*$  around  $T_{i,j,k}^*$  on the vertical boundary surface are obtained:

$$T_{i-1,j,k}^* \approx T_{i,j,k}^* - \Delta x T_{xxk}^* \frac{(\Delta x)^2}{2!} T_{xxk}^* \tag{39}$$

$$T_{i+1,j,k}^* \approx T_{i,j,k}^* + \Delta x T_{xxm}^* \frac{(\Delta x)^2}{2!} T_{xxm}^* \tag{40}$$

Where  $T_{i,j,k}^n$  represents the temperature derivation  $\partial T^* / \partial x$  for the mould (k) in the net point  $(i,j,k)$ . From equations (39) and (40), the derivation of the second order is expressed:

$$T_{xxk}^* = \frac{2}{(\Delta x)^2} (T_{i-1,j,k}^* - T_{i,j,k}^* + \Delta x T_{xxk}^*) \tag{41}$$

$$T_{xxm}^* = \frac{2}{(\Delta x)^2} (T_{i+1,j,k}^* - T_{i,j,k}^* + \Delta x T_{xxm}^*) \tag{42}$$

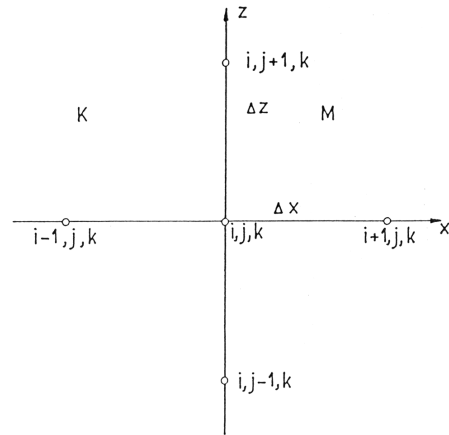


**Figure 3:** The vertical boundary surface YZ between the mould and the metal  $(\Delta x = \Delta z)$ .

**Slika 3:** Vertikalna ločilna površina YZ med kokilo in kovino  $(\Delta x = \Delta y)$

By means of Brian’s method and assuming that on the boundary interface there is a continuity of heat flow:

$$K_k T_{xk}^* = K_m T_{xm}^* \tag{43}$$

We obtain:

$$\frac{2}{(\Delta x)^2} [K_k (T_{i-1,j,k}^* - T_{i,j,k}^*) + K_m (T_{i+1,j,k}^* - T_{i,j,k}^*)] + (K_k + K_m) \partial_y^2 T_{i,j,k}^n + (K_k + K_m) \partial_z^2 T_{i,j,k}^n = \left( \frac{K_k}{a_k} + \frac{K_m}{a_m} \right) \frac{T_{i,j,k}^* - T_{i,j,k}^n}{\Delta t/2} \tag{44}$$

By dividing equation (44) with  $(K_k + K_m)/(\Delta x)^2$  and with

$$Z_{i,j,k,n} = \frac{(\Delta x)^2}{\Delta t (K_k + K_m)} \left( \frac{K_k}{a_k} + \frac{K_m}{a_m} \right) \tag{45}$$

We obtain:

$$\frac{2K_k}{K_k + K_m} T_{i-1,j,k}^* + 2(Z_{i,j,k,n} + 1)T_{i,j,k}^* - \frac{2K_m}{K_k + K_m} T_{i+1,j,k}^* = T_{i,j-1,k}^n + T_{i,j+1,k}^n + T_{i,j,k-1}^n + T_{i,j,k+1}^n + 2(Z_{i,j,k,n} - 2)T_{i,j,k}^n \tag{46}$$

By analogy, equations for the second intermediate value  $T^{**}$  (47) and the value  $T^{n+1}$  for second  $\Delta t/2$  (48) are obtained:

$$-T_{i-1,j,k}^{**} + 2(Z_{i,j,k,n} + 1)T_{i,j,k}^{**} - T_{i+1,j,k}^{**} = \frac{2K_k}{k_k + k_m} T_{i-1,j,k}^* - 2T_{i,j,k}^* + \frac{2K_m}{K_k + K_m} T_{i+1,j,k}^* + T_{i,j,k-1}^n + T_{i,j,k+1}^n + 2(Z_{i,j,k,n} - 1)T_{i,j,k}^n \tag{47}$$

$$-T_{i-1,j,k}^{n+1} + 2(Z_{i,j,k,n} + 1)T_{i,j,k}^{n+1} - T_{i+1,j,k}^{n+1} = \frac{2K_k}{k_k + k_m} T_{i-1,j,k}^* - 2T_{i,j,k}^* + \frac{2K_m}{K_k + K_m} T_{i+1,j,k}^* + T_{i,j-1,k}^{**} + T_{i,j+1,k}^{**} + 2(Z_{i,j,k,n} - 1)T_{i,j,k}^{**} \tag{48}$$

In the same way the approximations for temperatures on the vertical XZ and the horizontal XY boundary surfaces are derived.



## PRESSURELESS REACTIVE SINTERING OF TiAl-TiC AND Ti<sub>3</sub>Al-TiC COMPOSITES

### REAKCIJSKO SINTRANJE KOMPOZITOV TiAl-TiC IN Ti<sub>3</sub>Al-TiC PRI ATMOSFERSKEM TLAKU

Varužan Kevorkijan<sup>1</sup>, Srečo Davor Škapin<sup>2</sup>

<sup>1</sup>Independent Researching plc, Betnavska cesta 6, 2000 Maribor, Slovenia

<sup>2</sup>Jožef Stefan Institute, Jamova 39, 1000 Ljubljana, Slovenia  
varuzan.kevorkijan@siol.si

*Prejem rokopisa – received: 2009-03-26; sprejem za objavo – accepted for publication: 2009-06-20*

TiAl and Ti<sub>3</sub>Al based composites reinforced with volume fractions 10–50 % of TiC particles were successfully prepared by pressureless reaction sintering of reaction mixtures consisting of commercial titanium aluminide powders (TiAl with traces of Ti<sub>3</sub>Al and the single phased Ti<sub>3</sub>Al) blended with the appropriate amount of ceramic reinforcement, 5–10 % of Al powder and, in some cases, also 5 % of Ti powder added as sintering agents. The green compacts made from the blended powder mixture were reaction sintered at 1300 °C for 2 h in an Ar + 4 % H<sub>2</sub>-rich environment using a vacuum furnace. The morphology of the commercial powders and the microstructure of the as-sintered composites were studied by scanning electron microscopy and X-ray diffraction analysis.

The pressureless sintering of as-received TiAl and Ti<sub>3</sub>Al powders resulted in samples with 10–15 % of the retained porosity. On the other side, the addition of 10 % of TiC particles to the sintering mixture improved pressureless densification enabling fabrication of composite samples with >95 % of theoretical density without addition of free aluminium. In these particular cases, densification was promoted by chemical reactions between TiAl or Ti<sub>3</sub>Al and TiC leading to the formation of Al<sub>3</sub>Ti<sub>2</sub>C<sub>2</sub> and Ti<sub>3</sub>AlC secondary bonding phases, respectively. However, as it was confirmed by sintering experiments, for successful (>95 % of theoretical density) *pressureless* densification of composite samples with more than 10 vol. of TiC, the addition of 5–10 % of free aluminium and 5 % of titanium, depending on the actual amount of TiC reinforcement, was necessary. The addition of Al and Ti promotes liquid reaction sintering and the formation of secondary Ti-Al-C bonding phases in an Al-Ti co-continuous network.

The tensile properties and Vickers hardness of composite samples were measured at room temperature. The improvement in tensile properties (except elongation) and Vickers hardness was found to correlate with the amount of TiC reinforcement in the matrix.

Key words: TiAl-TiC and Ti<sub>3</sub>Al-TiC composites, pressureless reaction sintering, secondary bonding phases, microstructure, room temperature tensile properties, Vickers hardness

Z reakcijskim sintranjem smo pripravili goste kompozitne materiale (z gostoto večjo od 95 % teoretične gostote) na osnovi spojnin TiAl in Ti<sub>3</sub>Al, ojačanih z ustrezno količino keramične faze, z volumenskim deleže, Al-prahu 5–10 % in, v določenih primerih, tudi z dodatkom 5 % Ti-prahu. Uporabljen komercialni TiAl prah je vseboval sledove Ti<sub>3</sub>Al, medtem ko je bil prah Ti<sub>3</sub>Al enofazen. Dodatek prahov Al in Ti k izhodnim sestavam je omogočal boljše sintranje. Izhodne homogenizirane sestave smo enoosno stisnili v pelete in jih reakcijsko sintrali v vakuumski peči pri 1300 °C, 2 h v zaščitni atmosferi Ar + 4 % H<sub>2</sub>. Morfologijo, sestavo in velikost delcev izhodnih prahov ter mikrostrukturo pripravljenih vzorcev smo analizirali z elektronskim vrstičnim mikroskopom in energijsko disperzijsko analizo ter z rentgensko praškovo difrakcijo.

Sintrani vzorci na osnovi spojnin TiAl in Ti<sub>3</sub>Al izkazujejo od 10 % do 15% poroznosti. Pri dodatku 10 % TiC k tem spojinam pa dobimo goste vzorce z gostoto več kot 95 % teoretične. V teh sistemih potečejo med segrevanjem reakcije med TiAl oziroma Ti<sub>3</sub>Al in TiC, pri čemer nastajajo vezne sekundarne faze Al<sub>3</sub>Ti<sub>2</sub>C<sub>2</sub> in Ti<sub>3</sub>AlC. Ugotovili smo, da za pripravo gostih kompozitnih materialov z reakcijskim sintranjem (>95 % teoretične gostote) pri višjem dodatku kot 10 % TiC potrebujemo še 5–10 % Al in 5 % Ti, kar je odvisno od količine TiC. Dodana elementa Al in Ti omogočata reakcijsko sintranje v tekoči fazi in tvorbo sekundarnih veznih faz na osnovi Ti-Al-C, dispergiranih ko-kontinuirni matriki Al-Ti.

Mehanske lastnosti (natezno trdnost in trdoto) smo merili pri sobni temperaturi. Izboljšanje natezne trdnosti in Vickersova trdota sta sorazmerni, ratezek pa obratno sorazmeren večanju vsebnosti TiC v kompozitih.

Ključne besede: TiAl-TiC in Ti<sub>3</sub>Al-TiC kompoziti, reakcijsko sintranje pri atmosferskem tlaku, sekundarne vezne faze, mikrostruktura, mehanske lastnosti pri sobni temperaturi, trdota po Vickersu

## 1 INTRODUCTION

TiAl- and Ti<sub>3</sub>Al-based intermetallic-matrix composites (IMCs) reinforced with ceramic particles have several advantages over conventional titanium alloys, such as higher elastic modulus, lower density, better mechanical properties at elevated temperatures, and higher oxidation resistance<sup>1,2</sup>. However, bringing these attractive intermetallic composite matrices into commercial use largely depends upon the availability of practical and competitive processing routes. Due to difficulties in

production of IMCs by foundry methods and the high cost of powder processing, the elemental powder metallurgy (EPM) route has been gaining more and more attention. According to the EPM processing route, near-net shape IMC products can be fabricated by the consolidation and forming of blended Ti and Al elemental powders and ceramic reinforcement, followed by a subsequent reactive synthesis and sintering process. However, due to the large difference between the partial diffusion coefficients of Ti and Al, the synthesis of TiAl/Ti<sub>3</sub>Al alloys via reactive sintering follows a

mechanism in which Al atoms move into the Ti lattice, thus leading to the formation of Kirkendall diffusion pores<sup>5</sup>. Although hot isostatic pressing (HIP) and other pressure-assisted methods have been reported to be effective in eliminating the porosity of reactively sintered TiAl- and Ti<sub>3</sub>Al-based composite matrices<sup>6-9</sup>, their high cost and low production efficiency make them unsuitable for commercial use.

In the present study the assumption was made that, if sufficient reactivity in the system is provided, **pressureless** sintered TiAl- and Ti<sub>3</sub>Al-based IMCs with >95 % T. D. may be successfully obtained, starting from TiAl and Ti<sub>3</sub>Al powders mixed with suitable ceramic reinforcement (such as TiC) and sintering additives (Al and Ti powders). During high temperature pressureless sintering, TiC and Al react with the TiAl and Ti<sub>3</sub>Al matrix forming different bonding phases. These promote further densification and elimination of porosity in the system.

Thus, the aim of this study was to investigate the potential of the pressureless sintering method in fabrication of fully dense, high quality TiAl- and Ti<sub>3</sub>Al-based IMCs by applying reaction mixtures consisting of **commercial** titanium aluminide powders mixed with various amounts (volume fractions from 10 % to 50 %) of TiC ceramic particles, 5–10 % of Al and 5 % of Ti sintering agent.

## 2 EXPERIMENTAL

Composites were prepared with blending commercially available powders of either TiAl or Ti<sub>3</sub>Al with TiC powder in appropriate amounts to create titanium aluminide-based matrices with volume fractions (10, 20, 30, 40 and 50) % of TiC discontinuous reinforcement.

The powder blends were thoroughly mixed and subsequently cold compacted. In all cases, the reaction synthesis was conducted at 1300 °C for 2 h in an Ar + 4 % H<sub>2</sub>-rich environment using a vacuum furnace.

The as-synthesized composite samples were cut, machined and polished in accordance with standard procedures.

Microstructural characterization was performed by scanning electron microscopy (SEM), whereas X-ray diffraction (XRD) measurements were applied to the samples to identify the phases and their crystal structure.

The specimens for optical microscope (OM) observation were electrolytically polished in a solution of 95 % CH<sub>3</sub>COOH and 5 % HClO<sub>4</sub>, and then etched in a solution of 5 % HNO<sub>3</sub>, 15 % HF, and 80 % H<sub>2</sub>O. The main grain sizes were measured by the linear intercept method.

The specimens for XRD were abraded with SiC paper and were then subjected to diffraction using CuK<sub>α</sub> radiation.

Quantitative determination of the volume percentage of the retained porosity was performed by analysing OM and SEM micrographs of infiltrated composites using the

point counting method and image analysis and processing software.

The tensile properties (tensile strength, 0.2 % tensile yield strength and elongation) of the composite specimens were determined in accordance with the ASTM test method, E8M-96. The tensile tests were conducted on drum shaped tension-test specimens 3.5 mm in diameter and 16 mm gauge length using an automated servo-hydraulic tensile testing machine with a crosshead speed of 0.254 mm/60 s.

The Vickers hardness (*HV*) measurements were performed at room temperature on polished composite samples as an average of 15 indentations. These measurements were made on an automatic digital tester using a pyramidal diamond indenter with a facing angle of 136° A 0.025 kg indenting load, 50 μm/s load applying speed, and a 15 s load holding time.

## 3 RESULTS AND DISCUSSION

### 3.1 Morphology of titanium aluminide powders applied

The as-received powders are non-agglomerated, with well shaped individual particles having similar particles

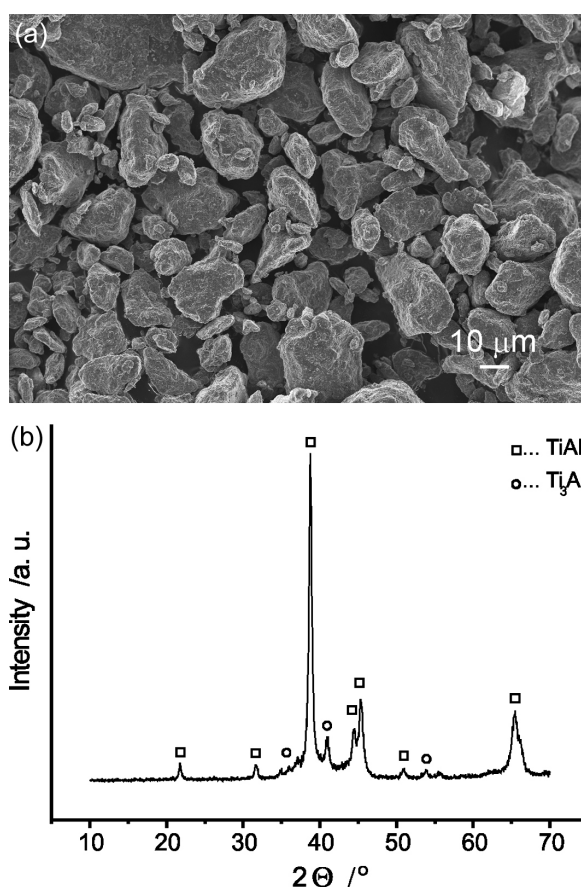


**Figure 1:** (a) SEM micrograph of as-received commercial TiAl powder and (b) XRD spectra of the TiAl powder showing traces of Ti<sub>3</sub>Al compound

**Slika 1:** (a) SEM-posnetek komercialnega prahu TiAl in (b) XRD-spekter prahu TiAl s sledmi spojine Ti<sub>3</sub>Al

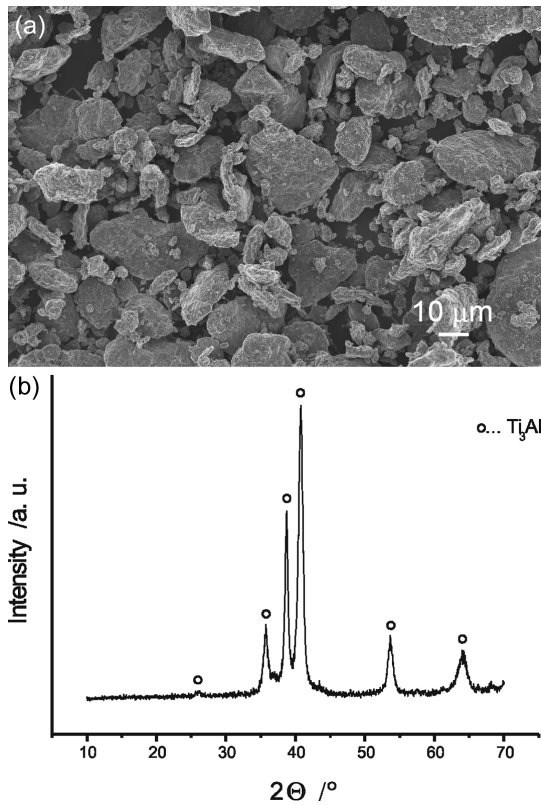


**Figure 2:** (a) SEM micrograph of as-received commercial  $Ti_3Al$  powder and (b) XRD spectra of the  $Ti_3Al$  powder  
**Slika 2:** (a) SEM-posnetek komercialnega prahu  $Ti_3Al$  in (b) XRD-spekter prahu  $Ti_3Al$

size (**Figure 1 and 2**).  $TiAl$  was with traces of  $Ti_3Al$  while  $Ti_3Al$  powder was single phase.

### 3.2 Microstructure development in IMCs reinforced with TiC

Generally, the microstructure of IMCs consists of an intermetallic matrix (based on an ordered intermetallic compound or a multiphase combination of intermetallic

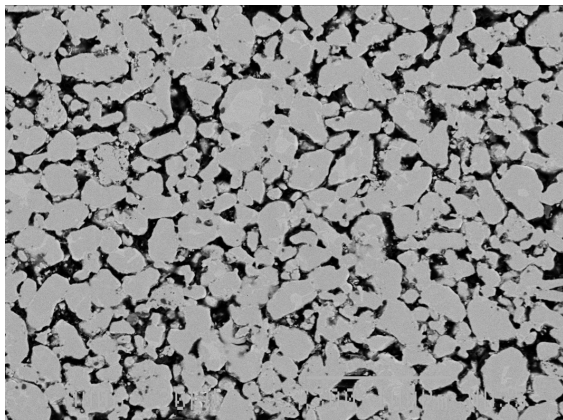


**Figure 3:** SEM micrograph of pressureless sintered non-reinforced  $TiAl$  compact. Sintering conditions:  $1300\text{ }^{\circ}C$ , 2 h  
**Slika 3:** SEM-posnetek vzorca  $TiAl$ , sintranega pri atmosferskem tlaku brez dodatkov keramične ojačitve. Pogoji sintranja:  $1300\text{ }^{\circ}C$ , 2 h

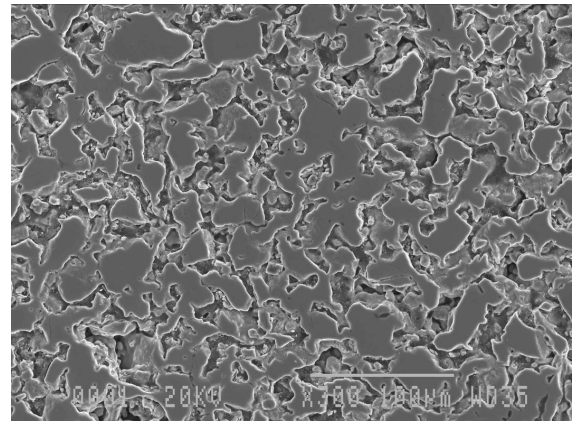


**Figure 4:** SEM micrograph of pressureless sintered non-reinforced  $Ti_3Al$  compact. Sintering conditions:  $1300\text{ }^{\circ}C$ , 2 h  
**Slika 4:** SEM-posnetek vzorca  $Ti_3Al$ , sintranega pri atmosferskem tlaku brez dodatkov keramične ojačitve. Pogoji sintranja:  $1300\text{ }^{\circ}C$ , 2 h

compounds), the ceramic particulate reinforcement and an interfacial region with the secondary phases formed during reactive sintering.

Cost-effective, pressureless densification of  $TiAl$  and  $Ti_3Al$  powders, as well as of  $TiAl$  and  $Ti_3Al$  powders blended with ceramic particulates most often results in

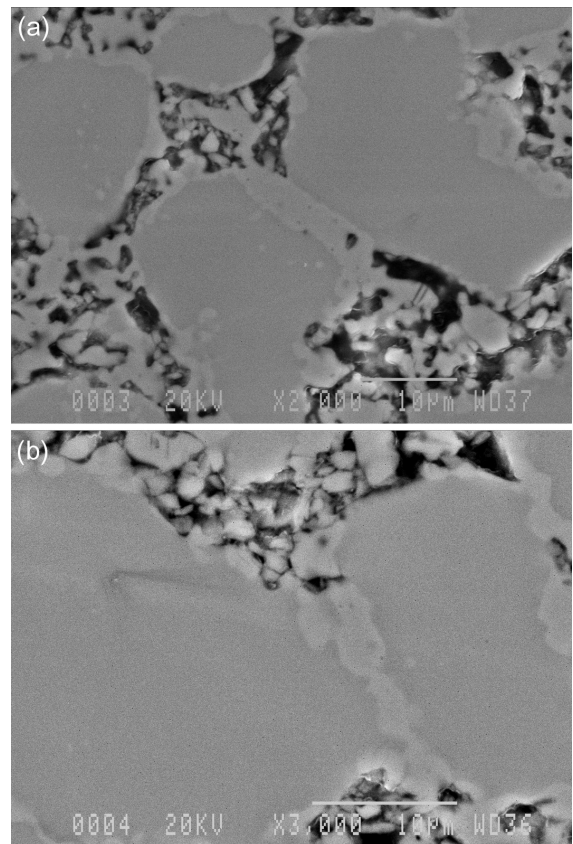


**Figure 5:** SEM micrograph of (a)  $Ti_3Al$  reactively bonded with  $Ti_3AlC$  and (b)  $TiAl$  reactively bonded with  $Al_2Ti_4C_2$  phases  
**Slika 5:** SEM posnetek (a)  $Ti_3Al$  reakcijsko vezanega s  $Ti_3AlC$  in (b)  $TiAl$  reakcijsko vezanega s fazo  $Al_2Ti_4C_2$

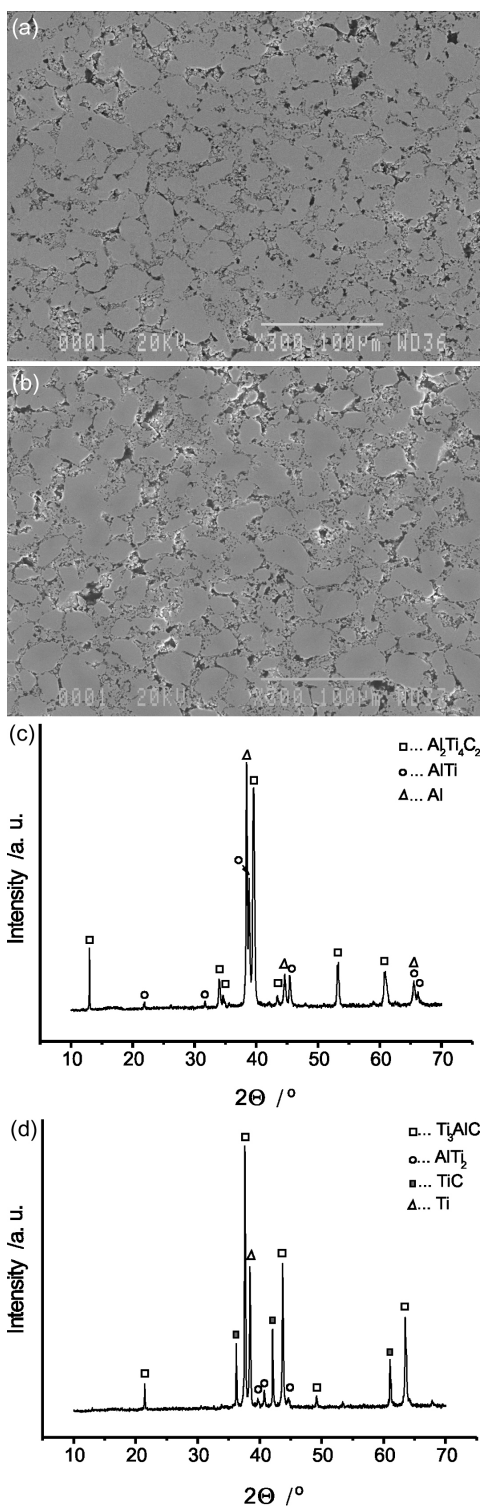


**Figure 6:** SEM micrograph of samples with the starting composition: (a) 90 % TiAl + 10 % TiC and (b) 90 % Ti<sub>3</sub>Al-10 % TiC sintered up to 95 % T. D. Sintering conditions: 1300 °C, 2 h, (c) XRD spectra of the sample with the starting composition 90 % TiAl + 10 % TiC and (d) XRD spectra of the sample with the starting composition 90 % Ti<sub>3</sub>Al + 10 % TiC

**Slika 6:** SEM-posnetek vzorcev z začetno sestavo: (a) 90 % TiAl + 10 % TiC in (b) 90 % Ti<sub>3</sub>Al-10 % TiC sintranih nad 95 % T. G. Pogoji sintranja: 1300 °C, 2 h, (c) XRD-spekter vzorca začetne sestave 90 % TiAl + 10 % TiC in (d) XRD-spekter vzorca začetne sestave 90 % Ti<sub>3</sub>Al + 10 % TiC

material that is not free of porosity. Typical microstructures of pressureless sintered non-reinforced TiAl and Ti<sub>3</sub>Al samples made from the commercial powders used in this work are presented in **Figures 3 and 4**. The samples obtained are porous (85–90 % T. D.).

However, based on the experimental results of pressureless sintering of TiAl-TiC and Ti<sub>3</sub>Al-TiC samples, it was recognized that addition of TiC improves the densification of the system, enabling pressureless fabrication of composites with more than 95 % of T. D., **Table 1**. Until the amount of TiC reinforcement in TiAl and Ti<sub>3</sub>Al based composites not overcome 10 %, pressureless sintering was completed without addition of any sintering agents. Densification was promoted by chemical reactions between TiAl or Ti<sub>3</sub>Al and the formation of Al<sub>2</sub>Ti<sub>4</sub>C<sub>2</sub> and Ti<sub>3</sub>AlC secondary phases:



As evident in **Figures 5 a,b**, the *in situ* formed Al<sub>2</sub>Ti<sub>4</sub>C<sub>2</sub> and Ti<sub>3</sub>AlC phases are involved in bonding of intermetallic grains and elimination of Kirkendall diffusion pores resulting in samples with density about 98 % T. D., **Table 1**.

The resulting microstructures of the sintered composite samples with 10 % of TiC particulate are presented in **Figure 6 a, b**.

As evident in **Figure 6 a,b**, the sintered samples possessed a near uniform distribution of equiaxial intermetallic grains, secondary phases and retained porosity. Larger pores were located mostly at the interface region, while high magnification observation revealed the presence of numerous fine pores uniformly distributed through the secondary phase, **Figure 7**.

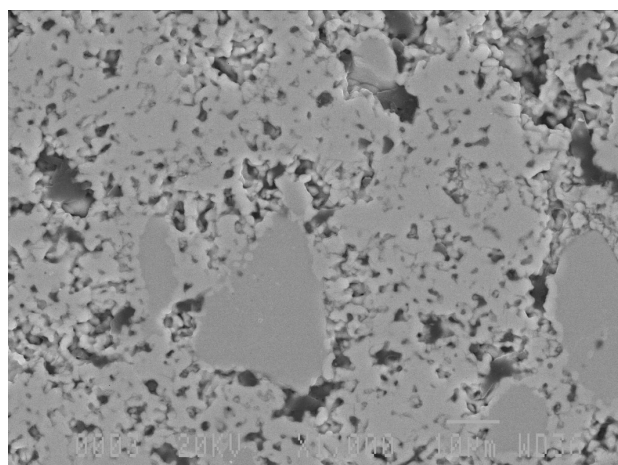


**Figure 7:** SEM micrograph of porous secondary phase between TiAl grains. Numerous fine pores are nearly uniformly distributed, including some larger ones at the interface. The grey inclusions are solidified aluminium.

**Slika 7:** SEM-posnetek porozne sekundarne faze med zrni TiAl. Številne fine pore so skoraj enakomerno razporejene, vključno z nekaterimi večjimi na fazni meji. Vključki sive barve so iz strjenega aluminija.

**Table 1:** Average room temperature tensile properties and Vickers hardness of various laboratory prepared composite samples

**Tabela 1:** Povprečne vrednosti mehanskih lastnosti, izmerjene pri sobni temperaturi in vrednosti trdote po Vickersu vzorcev kompozitov

Initial chemical composition in volume fractions (%)	Retained porosity (%)	<i>E</i> (GPa)	Tensile strength (MPa)	0.2 % tensile yield strength (MPa)	Vickers hardness (GPa)	Elongation in 50 mm (%)
90Ti <sub>3</sub> Al + 10TiC	4.1 ± 0.4	118 ± 12	474 ± 47	323 ± 32	2.9 ± 0.3	0.5 ± 0.05
75Ti <sub>3</sub> Al + 20TiC+5Al	3.9 ± 0.4	158 ± 16	518 ± 52	389 ± 39	3.6 ± 0.4	0.3 ± 0.03
60Ti <sub>3</sub> Al + 30TiC+10Al	3.6 ± 0.4	194 ± 20	547 ± 55	419 ± 42	5.8 ± 0.6	0.2 ± 0.02
50Ti <sub>3</sub> Al + 40TiC+10Al	3.3 ± 0.3	222 ± 22	596 ± 60	448 ± 45	6.2 ± 0.6	0.1 ± 0.01
40Ti <sub>3</sub> Al + 50TiC+10Al	4.4 ± 0.4	253 ± 25	619 ± 62	490 ± 49	6.5 ± 0.7	0.1 ± 0.01
90TiAl + 10TiC	4.0 ± 0.4	196 ± 20	339 ± 34	273 ± 27	2.7 ± 0.3	0.5 ± 0.05
75TiAl + 20TiC+5Al	3.8 ± 0.4	215 ± 22	368 ± 37	289 ± 29	3.2 ± 0.3	0.3 ± 0.03
70TiAl + 20TiC+10Al	3.4 ± 0.3	226 ± 23	419 ± 42	322 ± 32	5.1 ± 0.5	0.2 ± 0.02
60TiAl + 30TiC+10Al	3.9 ± 0.4	244 ± 24	453 ± 45	346 ± 35	5.6 ± 0.6	0.2 ± 0.02
50TiAl + 40TiC+10Al	4.0 ± 0.4	272 ± 27	493 ± 49	380 ± 38	6.0 ± 0.6	0.1 ± 0.01
40TiAl + 50TiC+10Al	4.2 ± 0.4	299 ± 30	516 ± 52	412 ± 41	6.4 ± 0.6	0.1 ± 0.01

In samples with 20–50 % of TiC reinforcement, successful pressureless densification was achieved only by addition of 5–10 % of free aluminium as sintering agent. The role of free aluminium was twofold: (i) it reacted with TiC forming Al-Ti-C bonding phase and (2)

provided liquid Al-Ti phase necessary for liquid reaction sintering and impregnation of pores.

The microstructure of the composites obtained, **Figure 8**, is characterized by isolated TiAl and Ti<sub>3</sub>Al

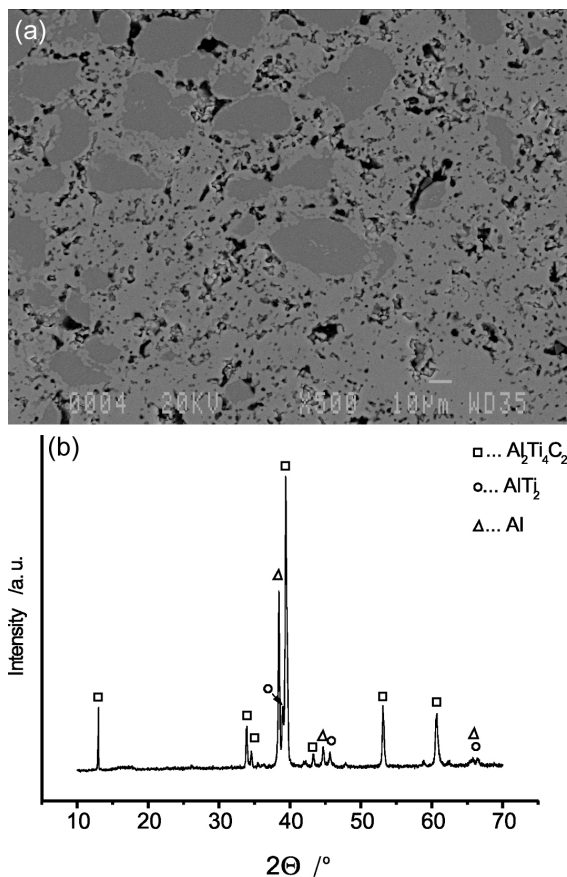


**Figure 8:** SEM micrograph and XRD spectra of the sample with the starting composition of TiAl-50 % TiC-5 % Al. The secondary formed Al<sub>2</sub>Ti<sub>4</sub>C<sub>2</sub> and AlTi<sub>2</sub> phases are porous.

**Slika 8:** SEM-posnetek in XRD-spekter vzorca začetne sestave TiAl-50 % TiC-5 % Al. Sekundarno ustvarjene faze Al<sub>2</sub>Ti<sub>4</sub>C<sub>2</sub> in AlTi<sub>2</sub> so porozne.

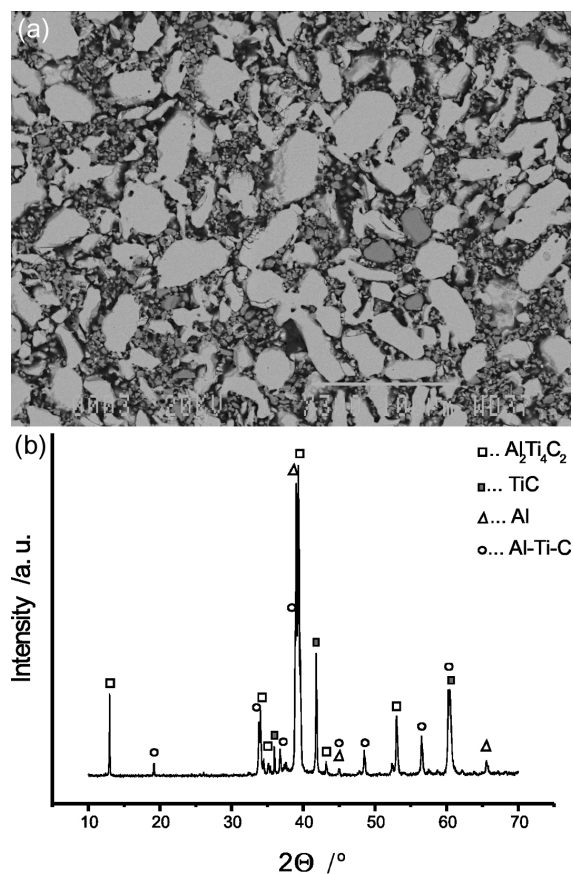


**Figure 9:** SEM micrograph and XRD spectra of TiAl-50 % Al-5 % Ti composite sample with a secondary phases well infiltrated with solidified Al-Ti alloy (dark continuous phase)

**Figure 9:** SEM posnetek in XRD-spekter vzorca začetne sestave TiAl-50 % TiC-10 % Al-5 % Ti s sekundarnimi fazami popolnoma infiltriranimi z zlitino Al-Ti (temna zvezna faza)

grains well surrounded by a secondary bonding phases and finely dispersed TiC particulates.

However, as evident in **Figure 8**, the secondary phases formed during reactive sintering of specimens with a high amount of TiC and 5 % of Al remain porous. For a more complete densification of secondary phases, the free aluminium content in the green compacts was increased to 10 % and 5 % of Ti powder was also added. The role of Ti was to promote the infiltration of an Al-Ti alloy into the porous regions of the secondary phases and the formation of TiAl and/or Ti<sub>3</sub>Al secondary intermetallics inside the pores leading to its closing.

The microstructure of samples sintered with addition of Al and Ti is shown in **Figure 9**.

### 3.3 Mechanical properties

The results of room temperature tensile tests on composite samples are listed in **Table 1**. As a result of matrix reinforcement, significant improvements in Young's modulus, tensile strength and ultimate tensile strength as well as Vickers hardness of the fabricated composites were observed, resulting in IMCs with excellent mechanical properties. These mechanical properties were found to be slightly better in composites with Ti<sub>3</sub>Al-based matrix compared to the TiAl-based matrix counterparts. Comparing the mechanical properties of composite samples with various volume fractions of ceramic particles in the matrix, it was found that Young's modulus, tensile strength, ultimate tensile strength and Vickers hardness increased while elongation decreased with an increasing fraction of ceramic reinforcement.

## 4 CONCLUSION

A study of the fabrication of TiAl- and Ti<sub>3</sub>Al-based intermetallic matrix composites (IMCs) discontinuously reinforced with 10 % to 50 % of TiC was conducted by applying conventional pressureless reactive sintering of single phase TiAl or Ti<sub>3</sub>Al powders and ceramic reinforcement. Following this cost-effective procedure, composites till 10 % of TiC reinforcement were routinely pressureless sintered to densities higher than 95 % of T. D. by solid state sintering with no sintering agents. On the contrary, in samples with more than 10 % of TiC reinforcement, the prerequisite for complete densification was the addition of small amount of Al powder or the mixture of Al and Ti powders with slight excess of Al over Ti-Al or 3Ti-Al stoichiometric composition. The elemental aluminium and titanium were involved in the formation of secondary bonding phases and liquid reaction sintering while the excess of aluminium is

necessary for complete infiltration of pores in the secondary phases formed during reactive sintering. In this way, dense composite samples with 10 % to 50 % of TiC reinforcement and a retained porosity less than 5 % were successfully obtained, revealing the significant industrial potential of this fabrication method.

Metallographic analysis of the as-densified microstructures confirmed that during densification TiAl and Ti<sub>3</sub>Al react with TiC and Al forming various secondary phases (Al<sub>2</sub>Ti<sub>4</sub>C<sub>2</sub>, Ti<sub>3</sub>AlC, AlTi<sub>2</sub>) responsible for simultaneous bonding of intermetallic grains and elimination of pores. An un-identified, continuous Ti-Al-C phase was also detected in samples sintered with addition of Al and Ti.

Regarding the room temperature tensile properties, the improvement of tensile strength, tensile yield strength and modulus was found to correlate with the amount of ceramic reinforcement in the matrix. However, quite the opposite behaviour was found regarding elongation, where the introduction of ceramic particles into the intermetallic matrix in all specimens led to a significant reduction of elasticity.

The best tensile properties (except elongation) were obtained in TiAl-TiC and Ti<sub>3</sub>Al-TiC samples with the highest amount (50 %) of ceramic reinforcement.

## Acknowledgment

This work was supported by funding from the Public Agency for Research and Development of the Republic of Slovenia, as well as the Impol Aluminium Company from Slovenska Bistrica, Slovenia, under contract No. 1000-07-219308

## 5 REFERENCES

- <sup>1</sup> Basics of Thermodynamics and phase transitions in complex intermetallics, E. B. Ferre, ed., World Scientific, Singapore, 2008, pp. 147
- <sup>2</sup> S. Djanarthany, J. C. Viala, J. Bouix: *Mater. Chem. Phys.*, 72 (2001), 301
- <sup>3</sup> E. K. Y. Fu, R. D. Rawlings, H. B. McShane, *J. Mater. Sci.*, 36 (2001), 5537
- <sup>4</sup> M. Sujata, S. Bhabgava, S. Sangal, *J. Mater. Sci. Lett.*, 16 (1997), 1175
- <sup>5</sup> F. Wenbin, H. Lianxi, H. Wenxiong, W. Erde, L. Xiaoqing, *Mater. Sci. Eng.*, 403 (2005), 186.
- <sup>6</sup> R. Martin, S. L. Kampe, J. S. Marte, T. P. Pete, *Metall. Mater. Trans. A*, 33 A (2002), 2747
- <sup>7</sup> Y. Yun-long, G. Yan-sheng, W. Hai-tao, W. Chuan-bin, Z. Lian-meng, *Journal of Wuhan University of Technology – Mater. Sci. Ed.*, 19 (2004), 1
- <sup>8</sup> T. W. Lee, C. H. Lee, *J. Mater. Sci. Lett.*, 18 (1999), 801
- <sup>9</sup> E. K. Y. Fu, R. D. Rawlings, H. B. McShane, *J. Mater. Sci.*, 26 (2001), 5542

# AN OPTICAL-EMISSION-SPECTROSCOPY CHARACTERIZATION OF OXYGEN PLASMA DURING THE OXIDATION OF ALUMINIUM FOILS

## KARAKTERIZACIJA KISIKOVE PLAZME MED OKSIDACIJO ALUMINIJEVIH FOLIJ Z OPTIČNO EMISIJSKO SPEKTROSKOPIJO

Nikša Krstulović<sup>1</sup>, Uroš Cvelbar<sup>2</sup>, Alenka Vesel<sup>2</sup>, Slobodan Milošević<sup>1</sup>,  
Miran Mozetič<sup>2</sup>

<sup>1</sup> Institute of Physics, Bijenička 46, HR-10000 Zagreb, Croatia

<sup>2</sup> Jozef Stefan Institute, Jamova 39, SI-1000 Ljubljana, Slovenia  
slobodan@ifs.hr

*Prejem rokopisa – received: 2009-06-06; sprejem za objavo – accepted for publication: 2009-06-18*

A highly reactive oxygen plasma was applied for the oxidation of aluminium foils. The plasma was created within a radio-frequency discharge operating at a power of 300 W and a frequency of 27.12 MHz. Samples of Al foils with dimensions of (20 × 40) mm were placed into the discharge chamber. During the treatment of the foils with oxygen plasma, the optical spectra were measured simultaneously with an optical spectrometer. The predominant spectral features observed during the treatment were atomic oxygen lines at 777.4 nm and 844.6 nm, atomic hydrogen lines and an OH band at 309 nm. As the oxidation took place other spectral features appeared. The major lines were Na at 589.35 nm and K at 766.5 nm and 769.9 nm. The time evolution of the Na and K peaks showed well-defined maxima after about a minute of plasma treatment. These maxima depended on the pressure in the discharge chamber. At the lowest pressure of 30 Pa the maxima appeared after about 100 s, while at a pressure of 80 Pa the maxima appeared after about 50 s. At a pressure of 120 Pa these maxima appeared after about 125 s. This behaviour was explained by the segregation of Na and K on the surface of the foil and the rapid desorption into the gas phase.

Keywords: oxygen plasma, aluminium foils, oxidation, optical emission spectroscopy

Za oksidacijo aluminijevih folij smo uporabili visoko reaktivno kisikovo plazmo, ki smo jo ustvarili z radiofrekvenčno razelektivitvijo pri frekvenci 27,12 MHz in moči 300 W. Vzorce Al-folij dimenzij 20 × 40 mm smo položili v razelektivitveno posodo in obdelali s kisikovo plazmo. Med obdelavo smo istočasno snemali optični emisijski spekter z optičnim spektrometrom. Prevladujoča spektralna posebnost obdelave so bili atomski kisikovi vrhovi pri valovnih dolžinah 777,4 nm in 844,6 nm, atomski vodikovi vrhovi ter molekulski pas OH pri 309 nm. Po začetku oksidacije folij se je pojavila tudi emisija Na pri 589,35 nm in K pri 766,5 nm ter 769,9 nm. Časovni razvoj teh vrhov je pokazal na izrazit maksimum po eni minuti obdelave. Izkazalo pa se je, da je ta maksimum odvisen od tlaka v razelektivitveni posodi. Pri najnižjem tlaku 30 Pa se je maksimum pojavil pri 100 s, medtem ko se je pri tlaku 80 Pa pri 125 s. Tako vedenje smo pojasnili s segregacijo Na in K na površino folij in njihovo hitro desorpcijo v plinsko fazo.

Ključne besede: kisikova plazma, aluminijeve folije, oksidacija, optična emisijska spektroskopija

## 1 INTRODUCTION

Commercially available aluminium foils are nowadays widely used in different industries, including the electronic and food industries. Aluminium is characterized by good electrical and thermal conductivities, and since the material is relatively inexpensive its application is very broad. However, in some cases the surface of the aluminium foil should be modified. In many cases, for example, the material would perform better if a thin film of oxide is formed on the surface. Anodic oxidation ensures the formation of such an oxide film by a process that requires special equipment which is not always available. An alternative technique is the oxidation of metals using an oxygen plasma<sup>1-6</sup>. This technique proved to work very well for several metals, including stainless steel. Since the application of such a method is interesting for the electronics industry we performed research on a modification of aluminium foils with a highly reactive oxygen plasma<sup>7-10</sup>. It was found that a

thin film of the order of 10 nm is rapidly grown on such foils. The technology should not cause any other modification of the material. In order to see whether the micro-elements are not affected by the plasma treatment we performed a systematic study of the plasma characterization during a treatment of aluminium foils. Namely, the microelements that may be depleted from the foils are presented in such a tiny concentration that they are not visible with standard techniques for surface and thin-film characterization. On the other hand, metallic atoms have low excitation energies and are thus visible by optical emission spectroscopy, even when present in extremely low concentrations<sup>11</sup>.

## 2 EXPERIMENTAL

The experiments were performed in a plasma reactor, which is schematically shown in **Figure 1**. The reactor is made from borosilicate glass with a low recombination coefficient for the reaction  $O + O \rightarrow O_2$ . The diameter of

the glass tubes presented in **Figure 1** is 40 mm. Two-sided tubes serve for the plasma characterization. One tube is terminated with a quartz window, while the other one is used for mounting a catalytic probe <sup>12-14</sup>. The samples are fixed on a thermocouple probe and placed in the centre of the discharge chamber, as shown in **Figure 1**. The RF coil is connected to the radiofrequency generator operating at a power of 300 W and a frequency of 27.12 MHz. On one side, the discharge chamber is pumped with a two-stage rotary pump with a nominal pumping speed of 16 m<sup>3</sup>/h, while on the other side commercially available oxygen is continuously leaked. The pressure in the experimental system is measured with an absolute pressure gauge. The ultimate pressure in the system is about 7 Pa. The residual atmosphere consists of water vapour and traces of other gases <sup>15</sup>. The optical emission spectra are detected through an optical fibre by an optical spectrometer (Ocean Optics HR 2000 CG-UV-NIR). The spectra were detected in the entire range from 200 nm to 950 nm. The spectra were taken at an integration time of 900 ms and a repetition time of 1 s. The spectral resolution of the spectrometer was 1 nm. The spectral sensitivity of the optical system was measured with a reference light source (LS-1-CAL, OceanOptics), and with a deuterium lamp for the range below 400 nm. The spectral sensitivity is almost flat in the region between 400 nm and 800 nm, but it drops significantly towards the edges <sup>15,16</sup>.

### 3 RESULTS

The samples were exposed to oxygen plasma at different pressures between 30 Pa and 120 Pa. The optical spectra were measured continuously during the plasma treatment, as explained above. Typical optical spectra are shown in **Figure 2**. **Figure 2** represents three characteristic spectra: after a) the first few seconds b) after 50 s, c) after a prolonged time (220 s)

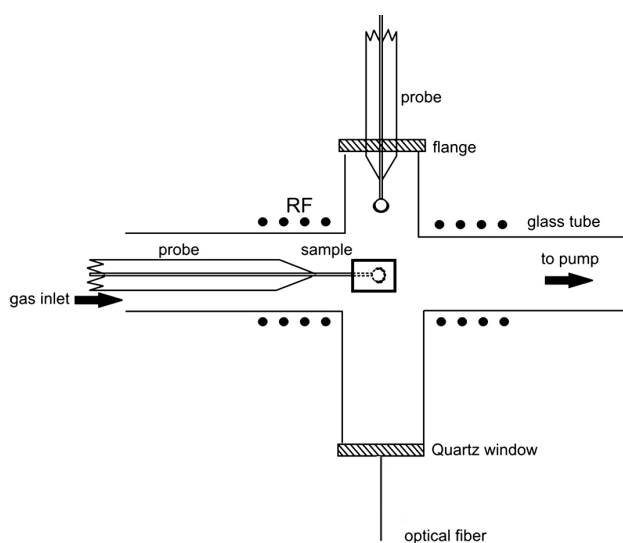


**Figure 1:** Schematics of discharge vessel  
**Slika 1:** Shema rezelektivne posode

after 50 s, c) after a prolonged treatment. The major spectral features are oxygen atom lines in the red part of the spectra and O<sub>2</sub> molecular band at 760 nm ( $b^1\Sigma_g^+ - X^3\Sigma_g^-(0,0)$ ) <sup>17</sup>. Apart from these lines, additional lines of the atomic hydrogen Balmer series and the impurity molecular OH band at 309 nm <sup>18</sup>, the N<sub>2</sub> 2<sup>nd</sup> positive band, ( $C^3\Pi_u - B^3\Pi_g$ ) around 315 nm <sup>19</sup>, and the CO Angstrom band 450–600 nm <sup>20</sup> are present. As the oxidation took place, other spectral features appeared. The major lines were Na at 589.35 nm (unresolved D-lines) and K at 766.5 nm and 769.9 nm. The time evolution of all these peaks during the plasma treatment of the Al foil is shown in **Figure 3** for the O, Na and K transitions, and in **Figure 4** for the other peaks: H $\alpha$ , CO, O<sub>2</sub>, OH. All these experiments were performed at a pressure of 80 Pa. Note that the oxygen line's intensity exhibits a local minimum, while the Na and K lines are of maximum intensity. Another set of experiments was performed at different pressures. The time at which the maximum in the sodium peak was observed is plotted in **Figure 5**.

### 4 DISCUSSION

The spectrum presented in **Figure 2 a)** is rather typical for oxygen plasma created in an experimental chamber that is sealed with rubber gaskets and never

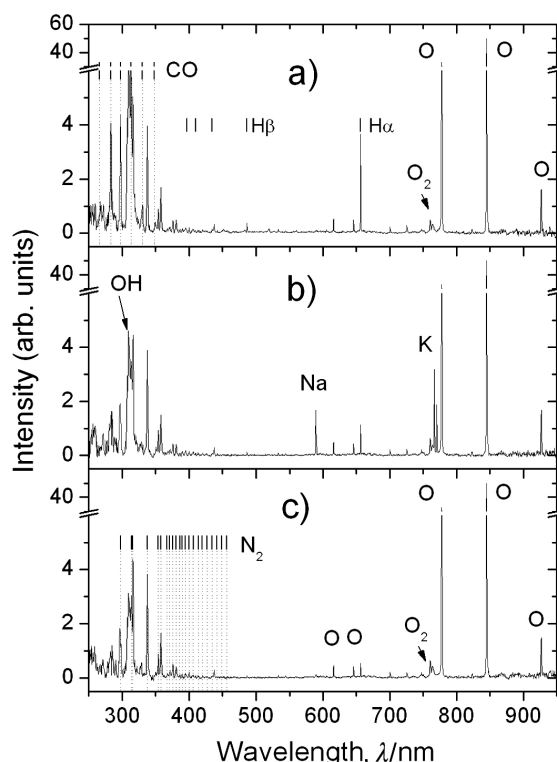


**Figure 2:** Typical optical emission spectra of the plasma in a) the first few s b) after 50 s, c) after a prolonged time (220 s). The oxygen gas pressure was 80 Pa and the discharge power 300W

**Slika 2:** Značilni optično emisijski spekter plazme v a) prvih nekaj sekundah, b) po 50 s in c) po daljšem času (220 s) pri tlaku kisika 80 Pa in razelektivni moči 300W

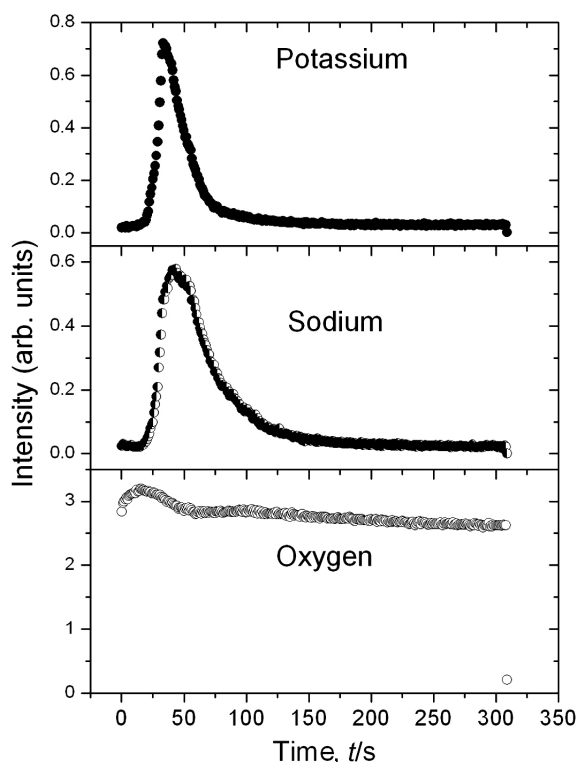


**Figure 3:** Time evolution for Oxygen 777,4 nm, Sodium 589,35 nm and Potassium 766,5 nm intensities during a plasma treatment at 80 Pa of oxygen pressure

**Slika 3:** Časovna odvisnost intenzitet vrhov kisika O 777,4 nm, natrija Na 589,35 nm in kalija K 766,5 nm pri obdelavi v kisikovi plazmi s tlakom 80 Pa

backed<sup>15,21,22</sup>. Apart from the oxygen lines we could observe the OH band in the UV range as well as the molecular nitrogen and CO bands. The relatively strong emission from the hydrogen atoms is due to the dissociation of water molecules in our plasma. The nitrogen band probably comes from a small leakage of the system, while the CO band is probably due to the oxidation of traces of organic impurities. All these spectral features decrease in intensity with an increasing treatment time, as shown in Figure 4. Such a decrease is explained by the continuous pumping of the vacuum system and, also, the relatively good oxidation of the organic impurities. More interesting is the appearance of the Na and K peaks, as is clearly shown in **Figure 2 b)**. These elements do not come from the discharge chamber because they are not observed for the case of an empty chamber. The origin of these two metals is obviously the aluminium foil. A strong maximum of these peaks is observed versus the treatment time, as shown in **Figure 3**. Such maxima are explained by the heating of the aluminium foils during the plasma treatment. Namely, the aluminium foil interacts with the oxygen atoms that are present in a large concentration in the oxygen plasma. The interaction is both physical and chemical. The major physical interaction is a heterogeneous surface recombination. At the reaction  $O + O \rightarrow O_2$  the dissociation energy is released and observed as the internal energy of the aluminium foil. The recombination coefficient definitely depends on the surface properties of the aluminium foil, as well as its temperature.

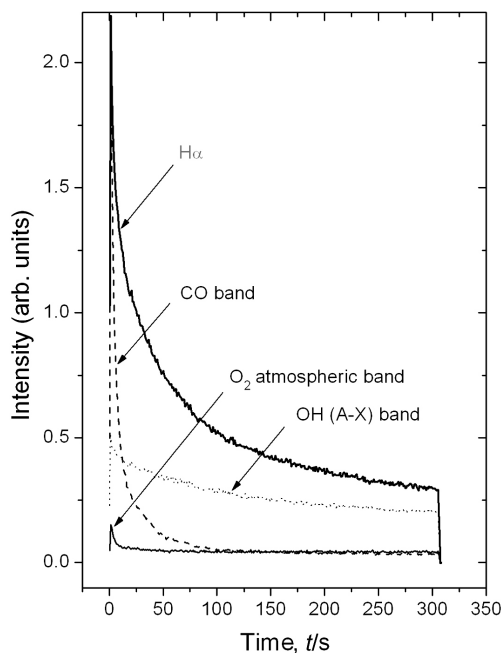


**Figure 4:** Time evolution for  $H_{\alpha}$  (656,2 nm), CO (519,3 nm),  $O_2$  (760,5 nm), OH (309 nm) intensities during a plasma treatment in 80 Pa of oxygen pressure

**Slika 4:** Časovna odvisnost intenzitet vrhov  $H_{\alpha}$  (656,2 nm), CO (519,3 nm),  $O_2$  (760,5 nm), OH (309 nm) pri obdelavi v kisikovi plazmi s tlakom 80 Pa

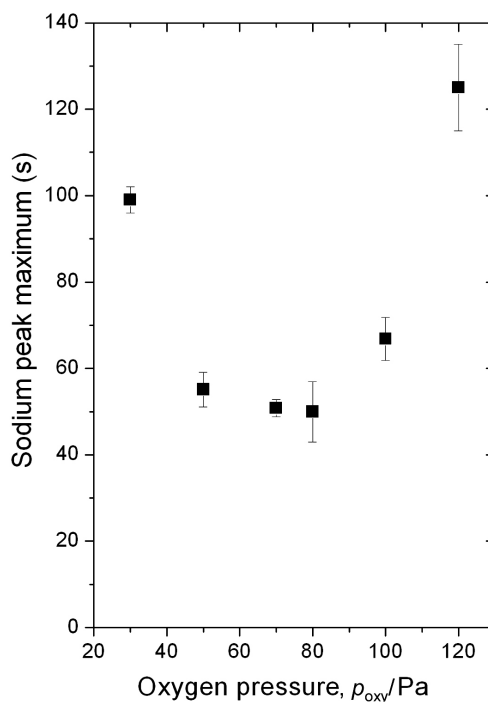


**Figure 5:** The treatment time at which the maximum of the Sodium 589,35 nm peak was achieved is plotted versus pressure

**Slika 5:** Čas obdelave v odvisnosti od tlaka, pri katerem je dosežen maksimum vrha natrija 589,35 nm

Although exact data are not available, it is generally accepted that the recombination coefficient increases with increasing temperature. This is the main heating mechanism. Apart from the physical reactions there is also a chemical reaction, e.g., the formation of a thin oxide film. Let us now discuss an extremely pronounced peak in the sodium and potassium lines versus the plasma treatment time. At first the sample temperature is low, so hardly any migration of Na and K from the bulk toward the surface is observed. However, as soon as the samples are heated to an elevated temperature, surface aggregation occurs and thus the intensity of spectral line increases with increasing temperature. After a certain treatment time the temperature is so high that the formation of an oxide film is accomplished. The oxide film represents a diffusion barrier for the migrating Na and K atoms so the concentration of these two metals in the plasma keeps decreasing. The drop in the Na and K lines is far from being sudden. This effect may be explained either by inhomogeneous oxidation or by poor pumping from the discharge region. Namely, both Na and K may adsorb on the surface of the glass chamber and desorb slowly during the continuous pumping. Let us now explain the very well pronounced minimum in the curve presented in **Figure 5**. At low pressure the density of the oxygen atoms is relatively low, so the heating by heterogeneous surface recombination is relatively poor. That is why the maximum is observed after about 100 s of plasma treatment. At high pressure, the oxygen atom density is high, but the treatment time is even longer. This effect can be explained either by good cooling of the sample due to pretty large drift velocity of the gas through our plasma reactor or by the lack of energetic ions. Namely, the kinetic energy of the ions reaching the surface of the aluminium foils depends on both the Debye length and the mean free path<sup>23,24</sup>. In the case of a short Debye length and a long mean free path the sheath around the sample is collision-less, so oxygen ions do not lose their kinetic energy. At the other extreme the ions suffer many collisions with neutrals in the sheath and lose practically all their kinetic energy. In our plasma the Debye length keeps increasing with the increasing pressure and the mean free path keeps decreasing with the increasing pressure. Obviously, the samples exposed to plasma at 30 Pa are bombarded with energetic oxygen ions, while this effect is missing at 120 Pa. In between these two extremes the ion energy is still high enough and the oxygen atom density is reasonably high to allow for rapid heating of the samples and thus the oxidation is achieved after about 50 s.

## 5 CONCLUSIONS

Samples of commercially available aluminium foils were exposed to a highly reactive oxygen plasma. The plasma was characterized by optical emission spectroscopy. We observed a rapid decrease in the concen-

tration of the impurities originally present in the discharge chamber. As the temperature of the samples was increasing we observed a rapid desorption of potassium and sodium from the samples. This desorption was explained by the migration of these two microelements from the bulk aluminium towards the surface. As an oxide film was formed on the surface, the diffusion was blocked and the intensity of Na and K spectral lines was decreasing with the increasing treatment time. Our results clearly show the applicability of optical emission spectroscopy for studying the migration of elements that are present in bulk aluminium at concentrations that cannot be detected with standard methods for the surface and thin-film characterization.

## Acknowledgements

This research was performed within the Slovenian-Croatian bilateral project BI-SLO-HR-01(2009-2010).

## 6 REFERENCES

- <sup>1</sup> M. Mozetič, U. Cvelbar, M.K. Sunkara, S. Vaddiraju, A method for the rapid synthesis of large quantities of metal oxide nanowires at low temperatures, *Advanced Materials (Weinh.)*, 17 (2005), 2138–2142
- <sup>2</sup> U. Cvelbar, K. Ostrikov, M. Mozetič, Reactive oxygen plasma-enabled synthesis of nanostructured CdO: tailoring nanostructures through plasma-surface interactions, *Nanotechnology (Bristol)*, 19 (2008), art. no. 405605
- <sup>3</sup> U. Cvelbar, Z. Chen, M.K. Sunkara, M. Mozetič, Spontaneous growth of superstructure [alpha]-Fe<sub>2</sub>O<sub>3</sub> nanowire and nanobelt arrays in reactive oxygen plasma, *Small (Weinh.)*, 4 (2008) 1610–1614
- <sup>4</sup> Z. Chen, U. Cvelbar, M. Mozetič, J. He, M. K. Sunkara Long-range ordering of oxygen-vacancy planes in [alpha]-Fe<sub>2</sub>O<sub>3</sub> nanowires and nanobelts, *Chemistry of Materials*, 20 (2008) 9, 3224–3228
- <sup>5</sup> Č. Donik, A. Kocijan, D. Mandrino, I. Paulin, M. Jenko, B. Pihlar, Initial oxidation of duplex stainless steel, *Applied Surface Science*, 255 (2009), 7056–7061
- <sup>6</sup> K. Ostrikov, Reactive plasmas as a versatile nanofabrication tool, *Reviews of Modern Physics*, 77 (2005), 489–511
- <sup>7</sup> U. Cvelbar, M. Mozetič, Behaviour of oxygen atoms near the surface of nanostructured Nb<sub>2</sub>O<sub>5</sub>, *Journal of Physics D: Applied Physics*, 40 (2007), 2300–2303
- <sup>8</sup> Z. Lj. Petrović, M. Šuvakov, Ž. Nikitović, S. Dujko, O. Šašić, J. Jovanović, G. Malović, V. Stojanović, Kinetic phenomena in charged particle transport in gases, swarm parameters and cross section data, *Plasma Sources Science and Technology*, 16 (2007), S1–S12
- <sup>9</sup> A. Ricard, F. Gaboriau, C. Canal, Optical spectroscopy to control a plasma reactor for surface treatments, *Surface and Coatings Technology*, 202 (2008), 5220–5224
- <sup>10</sup> I. Levchenko, K. Ostrikov, Nanostructures of various dimensionalities from plasma and neutral fluxes, *Journal of Physics D: Applied Physics*, 40 (2007), 2308–2319
- <sup>11</sup> M. Mozetič, U. Cvelbar, A. Vesel, N. Krstulović, S. Milošević, Interaction of oxygen plasma with aluminium substrates, *IEEE Transactions on Plasma Science*, 36 (2008), 868–869
- <sup>12</sup> U. Cvelbar, K. Ostrikov, A. Drenik, M. Mozetič, Nanowire sensor response to reactive gas environment, *Applied Physics Letters*, 92 (2008), art. No. 133505

- <sup>13</sup> C. Canal et al., Density of O-atoms in an afterglow reactor during treatment of wool, *Plasma Chemistry and Plasma Processes*, 27 (2007), 404–413
- <sup>14</sup> M. Mozetič, U. Cvelbar, A. Vesel, A. Ricard, D. Babič, I. Poberaj, A diagnostic method for real-time measurements of the density of nitrogen atoms in the postglow of an Ar-N<sub>2</sub> discharge using a catalytic probe, *Journal of Applied Physics*, 97 (2005) art. no. 103308
- <sup>15</sup> U. Cvelbar, N. Krstulović, S. Milošević, M. Mozetič, Inductively coupled RF oxygen plasma characterization by optical emission spectroscopy, *Vacuum* 82 (2007), 224–227
- <sup>16</sup> Z. Kregar, N. Krstulović, S. Milošević, K. Kenda, U. Cvelbar, M. Mozetič, Inductively coupled RF oxygen plasma studied by spatially resolved optical emission spectroscopy, *IEEE Transactions on Plasma Science*, 36 (2008), 1368–1369
- <sup>17</sup> P. Macko, V. Martisovits, Vibrational population of the O<sub>2</sub>(b<sup>1</sup>Σ<sub>g</sub><sup>+</sup>) state in a low-pressure oxygen pulsed discharge, *Czech. J. of Phys.*, 51 (2001), 491–502
- <sup>18</sup> S. Pellerin; J. M. Cormier, F. Richard, K. Musiol; D. J. Chapelle, A spectroscopic diagnostic method using UV OH band spectrum, *J. Phys. D: Appl. Phys.* 29 (1996), 726–739
- <sup>19</sup> N. Britun, M. Gaillard, A. Ricard, Y. M. Kim, K. S. Kim, J. G. Han, Determination of the vibrational, rotational and electron temperatures in N<sub>2</sub> and Ar-N<sub>2</sub> RF discharge, *J. Phys. D: Appl. Phys.* 40 (2007), 1022–1029
- <sup>20</sup> C. Rond, A. Bultel, P. Boubert, B. G. Chéron, Spectroscopic measurements of nonequilibrium CO<sub>2</sub> plasma in RF torch, *Chemical Physics* 354 (2008), 16–26
- <sup>21</sup> D. Vujošević, M. Mozetič, U. Cvelbar, N. Krstulović, S. Milošević, Optical emission spectroscopy characterization of oxygen plasma during degradation of Escherichia coli, *J. Appl. Phys.*, 101 (2007), 1033051–7
- <sup>22</sup> N. Krstulović, I. Labazan, S. Milošević, U. Cvelbar, A. Vesel, M. Mozetič, Optical emission spectroscopy characterization of oxygen plasma during treatment of a PET foil, *J. Phys. D: Appl. Phys.*, 39 (2006), 3799–3804
- <sup>23</sup> S. V. Vladimirov et al., Evolution of Langmuir waves in a plasma contaminated by variable-charge impurities, *Physical Review E*, 58 (1998), 8046–8048
- <sup>24</sup> Z. Lj. Petrović, Z. M. Raspopović, S. Dujko, T. Makabe, Kinetic Phenomena in Electron Transport in Radio Frequency Fields, *Applied Surface Science*, 192 (2002), 1–25



## EFFECT OF AGEING A TWO-PHASE Fe-NiCrMo ALLOY ON THE STRAIN HARDENING AT ROOM TEMPERATURE AND AT 290 °C

### VPLIV STARANJA DVOFAZNE ZLITINE Fe-NiCrMo NA DEFORMACIJSKO UTRJEVANJE PRI SOBNI TEMPERATURI IN PRI 290 °C

**Roman Celin, Jelena Vojvodič Tuma, Boris Arzenšek**

Institute of Metals and Technology, 1000 Ljubljana, Lepi pot 11, Slovenia  
roman.celin@imt.si

*Prejem rokopisa – received: 2009-03-26; sprejem za objavo – accepted for publication: 2009-05-26*

Fe-NiCrMo alloys were aged in the temperature range 290 °C to 350 °C for the spinodal decomposition of the ferrite solid solution. The tensile properties and the Charpy notch toughness were determined at room temperature and at 290 °C. The stress-strain curves were examined and the strain-hardening exponent was determined. This exponent changed little during the increase of the ferrite hardness and it is greater at 290 °C than at room temperature. This confirms the explanation proposed for the different effect of the test temperature on the notch toughness and the tensile properties.

Key words: austenite-ferrite microstructure, mechanical properties, ferrite hardness increase, strain hardening

Zlitina Fe-NiCrMo je bila starane v razponu temperature od 290 °C do 350 °C za spinodalno razgradnjo trdne raztopine v feritu. Določene so bile razrznne lastnosti in zarezna žilavost pri sobni temperaturi in pri 290 °C. Analizirane so bile krivulje napetost – deformacija in določen eksponent deformacijske utrditve avstenita. Ta eksponent se malo spremeni zaradi povečanja trdote ferita in je večji pri 290 °C kot pri sobni temperaturi. To potrjuje razlago, zakaj so pri višji temperaturi razrznne lastnosti nižje, zarezna žilavost pa večja kot pri sobni temperaturi.

Ključne besede: mikrostruktura ferita in avstenita, mehanske lastnosti, povečanje trdote ferita, deformacijska utrditev

## 1 AIM OF THE INVESTIGATION

During the ageing of Fe-NiCrMo alloys with a microstructure of austenite and ferrite the hardness of the ferrite is increased because of the spinodal decomposition of the solid solution in ferrite into two constituents: one enriched in chromium and the second enriched in nickel. In both phases the initial  $\alpha$ -iron lattice is preserved, while the lattice parameters are modified. Both constituents accommodate with elastic internal stresses that increase the hardness and brittleness and, after magnetisation, result in alloys with a suitable chemical composition and hard magnetic properties<sup>1,2</sup>. The kinetics of the decomposition depends on the diffusional transport of atoms in the substitutional solid solution in the ferrite. The rate of diffusion depends strongly on the temperature, and for this reason, the rate of spinodal decomposition-ageing is very slow in the temperature range in which alloys of this type are operating in power plants. In the ageing process of ferrite, the solid solution in austenite is stable; it may only change with the precipitation of carbides if the content of carbon is above the solubility limit. At higher temperature, the spinodal decomposition is replaced by the formation of  $\sigma$ -phases, which greatly diminishes the ductility of the alloys<sup>3</sup>. With ageing, the properties of the alloys with a two-phase microstructure of austenite and

ferrite are changed, depending on the volume share of ferrite and the extent of its decomposition.

In investigations of this type of alloys<sup>4</sup> it was established that the change of properties was greater for an alloy with 14.5 % of  $\delta$ -ferrite than for an alloy with 8.5% of  $\delta$ -ferrite when ageing in the temperature range 300 – 400 °C, while at higher temperatures the ageing effect was smaller. These findings were confirmed<sup>5</sup>, where it was found, also, that the content of  $\delta$ -ferrite determined from the Schaeffler diagram was unreliable and that the distribution of ferrite in as-cast alloys was inhomogeneous and could vary between 1.5 and 22.5 for the same cast piece. The ageing effect on the Charpy toughness was very strong in the temperature range 303 °C to 325 °C and the initial toughness was achieved again after annealing at 550 °C. Of the several processes that could affect the alloy's properties, the main embrittlement process is that of spinodal decomposition<sup>6</sup>. A correlation was developed<sup>7</sup> for the assessment of the embrittlement and the prediction of changes in the fracture and the Charpy and tensile properties of the as-cast two-phase alloys. The use of small specimens for the investigation of in-service-aged elbows gives reliable values for the J- $\Delta a$  results on the condition that strongly deviating specimens are rejected<sup>8</sup>. The low-cycle fatigue increases rapidly with the increase of the ageing time<sup>9</sup>. In<sup>10,11</sup> these findings were confirmed with the investigations of alloys with a different volume share of ferrite.

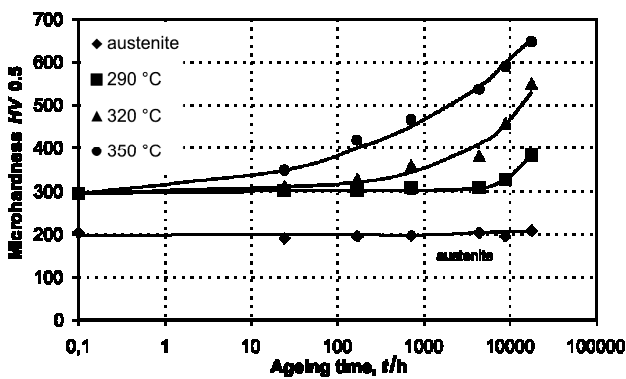


Figure 1: Effect of ageing time at 290 °C, 320 °C and 350 °C on the micro-hardness of the ferrite and austenite  
 Slika 1: Vpliv časa staranja pri 290 °C, 320 °C in 350 °C na mikrotrdoto ferita in avstenita

It was found, also, that the tensile properties of the unaged and aged alloys were lower and that the notch toughness was higher when testing at 290 °C. The aim of this work was to establish whether the difference was related to the different strain-hardening behaviour of the alloys at room temperature and at 290 °C.

In Figure 1 the effect of the ageing time and temperature on the ferrite and austenite microhardness are shown<sup>10,11</sup>. The austenite micro-hardness is not affected by the ageing, while the micro-hardness of the ferrite starts to increase after an ageing time that is shorter with higher temperature when the increase of the hardness is faster and stronger.

In Figures 2 and 3 the tensile properties and the notch toughness are given as a selection of data in<sup>10,11</sup>. After ageing and a hardness increase of the ferrite from HV 295 to about HV 650 units (an increase of the hardness by 2.15 times), the elongation and the reduction of area are decreased at both testing temperatures by about 30 %. For the average of the specimens aged for different times, the elongation and the reduction of area are lower by about 25 % at 290 °C than at room temperature.

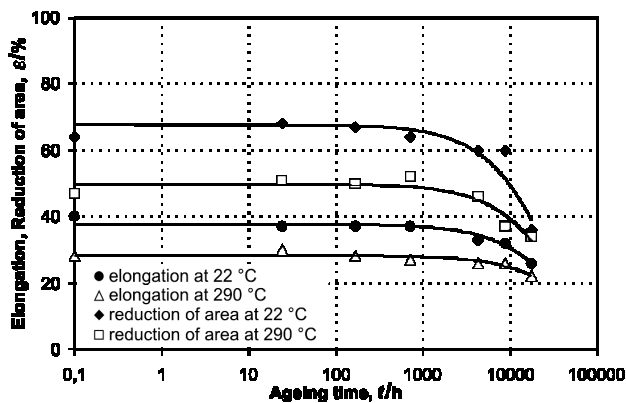


Figure 2: Effect of ageing time on the elongation and the reduction of area at room temperature and at 290 °C  
 Slika 2: Vpliv trajanja staranja na razteznost in kontrakcijo pri sobni temperaturi in pri 290 °C

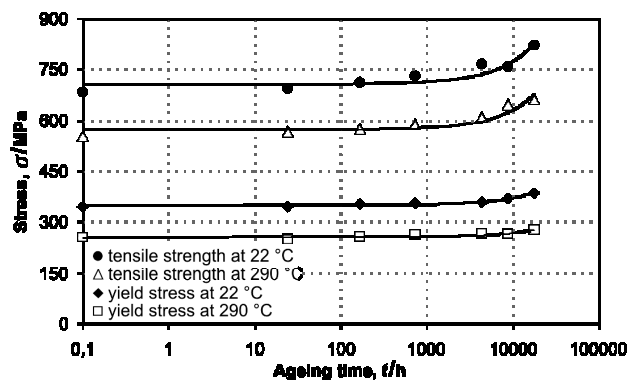
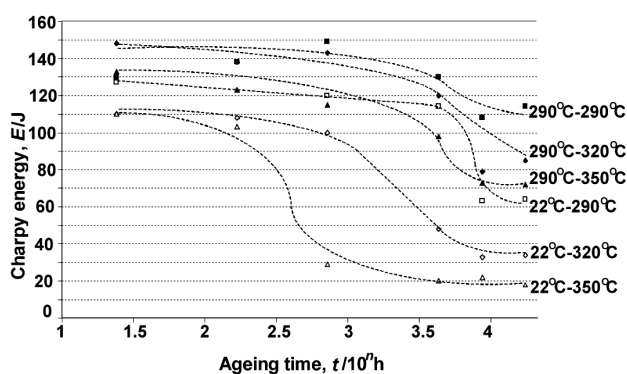


Figure 3: Effect of ageing time on the yield stress and the tensile strength at room temperature and at 290 °C  
 Slika 3: Vpliv trajanja staranja na mejo plastičnosti in razržno trdnost pri sobni temperaturi in pri 290 °C

The yield stress is increased very slightly with the increase of the ferrite hardness at both testing temperatures, and it is only about 11 % greater for both testing temperatures after the hardness of the ferrite was increased to HV 650 units. For the tensile strength, the effect of ageing time is greater, as at both testing temperatures it is increased by about 18 %. The effect of the testing temperature is greater for the yield stress, as it is decreased on average by 27 % at 290 °C, while the tensile strength is decreased by about 19 %. The changes are, in absolute values, larger with a large initial level and are of 99 MPa for the yield stress and 140 MPa for the tensile strength.

In Figure 4 the effect of ageing time at three temperatures on the notch toughness is shown for testing at room temperature and at 290 °C. When testing at room temperature, the notch toughness starts to decrease faster after ageing at 350 °C and 320 °C after the ferrite hardness has increased to about 350 units. This shows that the notch toughness is more sensitive to the effect of the ferrite's hardness increase. In<sup>11</sup> an explanation was proposed; that in the process of Charpy plastic deformation and fracturing during a rapid toughness decrease, the ferrite starts to fracture with a cleavage and that the accelerated decrease of the notch toughness is related to the cleavage of the ferrite inserts ahead of the tip of the propagating fracture. By ageing at 350 °C at a ferrite hardness of about 540 units a level of notch toughness is achieved that is not changed during any further increase of the hardness to 650 units. With a lower ageing temperature the final notch toughness level is achieved after the longest ageing time. The explanation could be either a difference in the extent of the spinodal decomposition due to the difference in the ageing temperature or that due to a level of hardness of about 450 units. It is mostly those ferrite inserts fracture with cleavage that have a favourable space orientation with regards to the plane of the propagating crack.

For the non-aged alloy the notch toughness is higher at 290 °C than at room temperature by about 20 J or 18



**Figure 4:** Effect of ageing time at three temperatures on the notch toughness at room temperature and at 290 °C

**Slika 4:** Vpliv časa staranja pri treh temperaturah na zarezno žilavost pri sobni temperaturi in pri 290 °C

%. After the longest ageing time the notch toughness at room temperature is decreased by about 82 % and much less, only by about 36 %, at a temperature of 290 °C. Accordingly, at this stage of the decomposition of the solid solution in ferrite, the difference in the notch toughness at 290 °C and room temperature is increased by about 3.5 times.

The tensile properties are lower and the notch toughness is higher when testing at 290 °C, than at room temperature. In<sup>11</sup> it is assumed that the differences between the properties at room temperature and 290 °C are probably the difference in the deformation and the fracturing behaviour of both kinds of tests due to the presence of the notch on the toughness specimens and the difference in test time, which cause a high local heating due to the very fast deformation and fracturing during the testing of the notched specimens<sup>12</sup>. A possible effect of the different strain hardening at both testing temperatures is surmised and this investigation is aimed at its experimental verification. The ageing temperature of 350 °C was selected because it results in the largest and fastest changes of ferrite hardness and notch toughness.

## 2 EXPERIMENTAL WORK

For this investigation the alloy and specimens in<sup>10,11</sup> were used, although the details on the preparation, ageing and testing of the alloys will also be summarised here. The composition of the investigated alloy was: 0.06 C, 1.68 Si, 0.67 Mn, 0.03 P, 0.01S, 9.0 Ni, 20.8 Cr and 2.46 Mo. The microstructure of the alloy is shown in **Figure 5**. The ageing temperatures were 290 °C, 320 °C and 350 °C and the ageing time was up to 17.520 h. Only specimens aged at 350 °C were used in this investigation because of the highest increase of the ferrite hardness. All the mechanical tests were performed at room temperature (22 °C) and at 290 °C. The micro-hardness was determined only at room temperature. Additional measurements of the ferrite micro-hardness were performed to

determine more accurately the hardness increase during the ageing time of the start of the rapid decrease of the notch toughness and the tensile tests were performed for specimens aged for up to the longest ageing time. Austenite does not fracture with a cleavage, and so for this reason, and according to<sup>8</sup>, the exceedingly deviating Charpy results were rejected as being due to the local, greatly increased content of ferrite in the specimen with a small section and the as-solidified microstructure.

The uniform plastic deformation was determined by measuring the lengthening of the strain on the stress-strain curves from the end of the elastic deformation to the maximum stress of the strain curves. This part of the true-stress, true-strain curve was digitalised, a linear dependence was obtained in the log-log coordinates and the approximate strain coefficient was deduced from its slope for specimens aged for different times at 350 °C.

The shape of the recorded stress-strain curves in **Figures 6** and **7** shows that the tensile behaviour of the alloy depends on the extent of the age hardening of the ferrite and of the testing temperature. In **Figures 8** and **9** the strain hardening part of the stress-strain curves between the start of the plastic deformation and the maximum tensile force are shown. The linear shape confirms that the slope of the dependence can be used as a reliable representation of the strain-hardening exponent.

Theoretically, the effect of increasing the strain on the deformation resistance is due to the increase in the number of dislocations, and it is deduced as<sup>13</sup>

$$\sigma_{\varepsilon} - \sigma_0 = \alpha G b \rho^{1/2} \quad (1)$$

where  $\sigma$  is the deformation resistance at a deformation of  $\varepsilon$ ,  $\sigma_0$  is the deformation resistance at the start of the plastic strain,  $\rho$  is the density of dislocations,  $G$  is the shear modulus and  $b$  is the Burgers vector.

The equation is not used because of the experimental complexity of determining the density of the dislocations. The strain-hardening exponent is used instead of

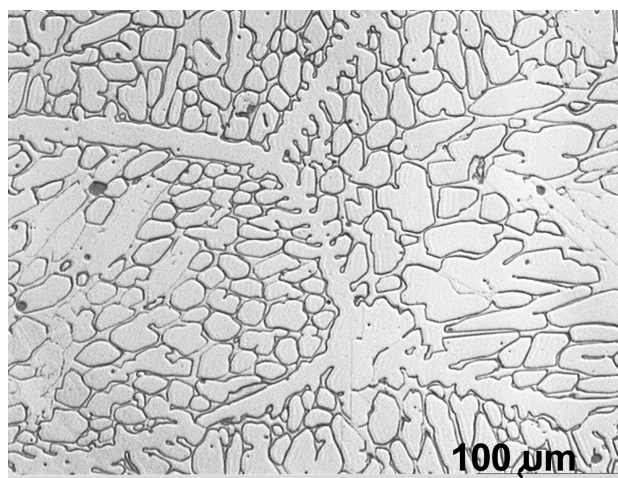


**Figure 5:** Microstructure of the investigated alloy with 27 % of ferrite  
**Slika 5:** Mikrostruktura raziskovane zlitine s 27 % ferita

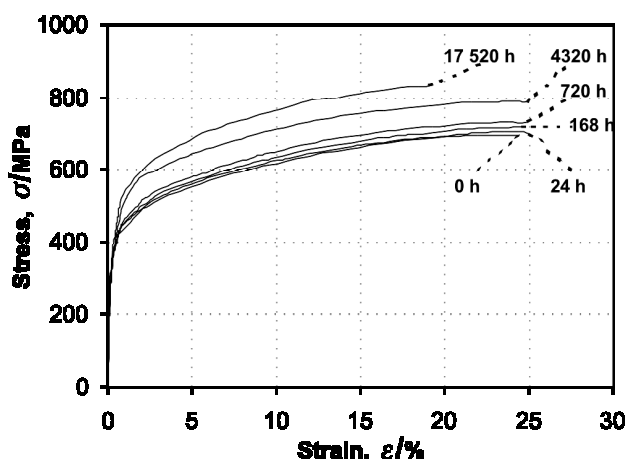


Figure 6: Strain-stress curves at room temperature for specimens aged for different times at 350 °C

Slika 6: Odvisnost napetost – deformacija pri sobni temperaturi za preizkušance, ki so bili starani različno dolgo pri 350 °C

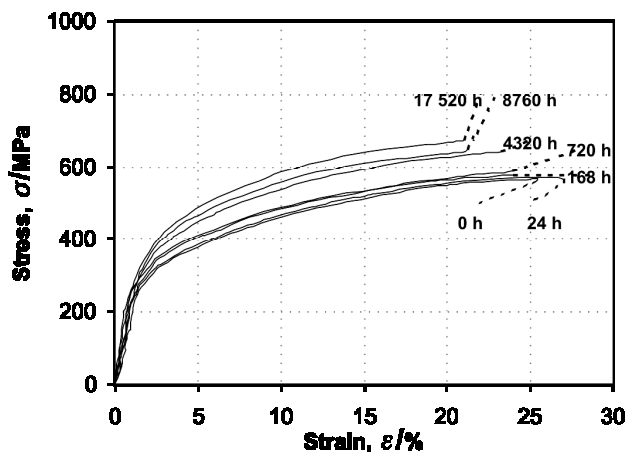


Figure 7: Strain-stress curves at 290 °C for specimens aged for different times at 350 °C

Slika 7: Odvisnost napetost – deformacija pri 290 °C za preizkušance, ki so bili starani različno dolgo pri 350 °C

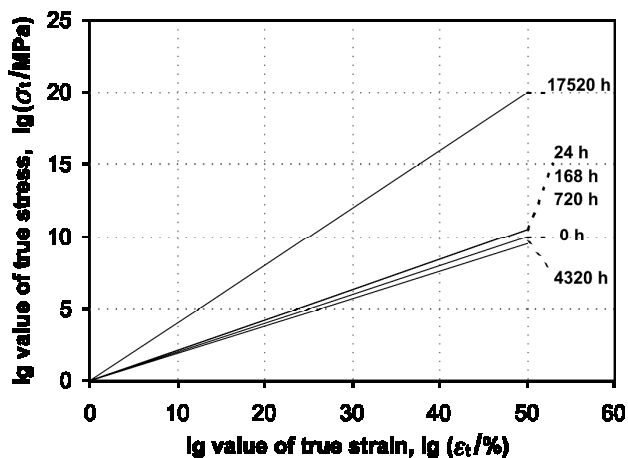


Figure 8: True-strain, true-stress dependence for the strain-hardening part of the curves in Figure 6

Slika 8: Odvisnost prave napetosti od prave deformacije za del krivulj na sliki 6 z deformacijsko utrditvijo v logaritmskih koordinatah

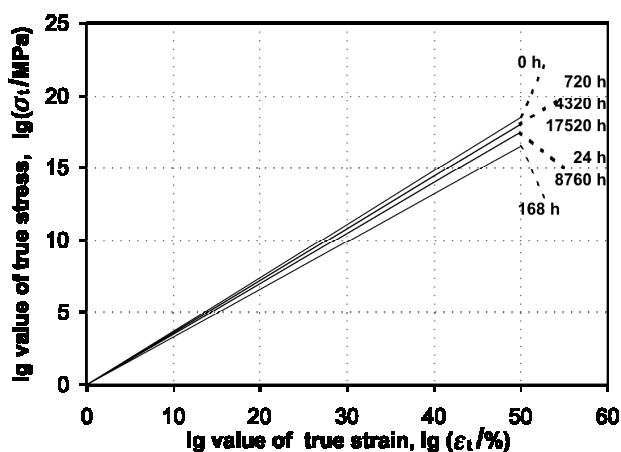


Figure 9: True-strain, true-stress dependence for the strain-hardening part of the curves in Figure 7

a measure of the effect of the plastic strain on the deformation resistance. It is deduced from equation<sup>14</sup>:

$$\sigma_e = k(\epsilon_0 + \epsilon)^n \quad (2)$$

where  $k$  is a constant,  $\epsilon_0$  is the initial strain,  $\epsilon$  is the strain increase, and  $n$  is the strain-hardening exponent.

For tensile tests  $k$  is a constant, and  $\epsilon_0 = 0$  if the strain hardening is started at the end of elastic deformation. In our case equation (2) can be written in the form  $\sigma = k \epsilon^n$ , which also describes the dependences in Figures 8 and 9. Since the value of the strain-hardening exponent was established from tests in equivalent conditions it can be used as a comparative value.

### 3 DISCUSSION

In Tables 1 and 2 the numerical data established from the stress-strain curves and the ferrite hardness are given. The ratio of the proportion to the maximum stress is, at room temperature, independent on the increase of ferrite hardness, while it increases slowly with this hardness at 290 °C. The plastic extension, a measure of the plastic strain before the start of the reduction of area, decreases very slowly with the increasing hardness of ferrite at both testing temperatures. In contrast, the approximate exponent of the deformation hardening is, for the ferrite hardness up to approximately HV 537 units, significantly lower at room temperature than at 290 °C. Above this hardness level it increases up to a value similar to that for testing at 290 °C. No similarity was found between the effect of the increase of the ferrite hardness on the coefficient of strain hardening and the notch toughness, as the toughness is greatly diminished by an unchanged strain-hardening coefficient. On the other hand, the coefficient of strain hardening is higher with a higher notch toughness at 290 °C than at room temperature. The notch toughness for ductile fracturing also depends strongly on the extent of the deformation before the crack is started at the notch tip<sup>15</sup>. All the tensile properties are higher at room temperature

**Table 1:** Characteristic parameters of the stress-strain curves in **Figures 6** and **8**. Testing at room temperature, ageing temperature 350 °C  
**Tabela 1:** Karakteristični parametri iz odvisnosti napetost deformacija na **slakah 6** in **8**. Preizkus pri sobni temperaturi, temperatura staranja 350 °C

Ageing <i>t</i> /h	$E_{pr}$ /MPa	$E_m$ /MPa	$E_{pr}/E_m$	Plastic extension	<i>n</i>	Ferrite hardness HV
0	341	708	0.48	0.27	0.20	295
24	362	703	0.51	0.25	0.21	350
168	356	720	0.49	0.24	0.21	419
720	352	729	0.49	0.25	0.21	465
4320	371	790	0.47	0.24	0.19	537
17520	376	832	0.47	0.19	0.40	648

**Table 2:** Characteristic parameters of the stress-strain curves in **Figures 7** and **9**. Testing at room temperature, ageing temperature 350 °C  
**Tabela 2:** Karakteristični parametri iz odvisnosti napetost deformacija na **slakah 6** in **7**. Preizkus pri sobni temperaturi, temperatūra staranja 350 °C

Ageing <i>t</i> /h	$E_{pr}$ /MPa	$E_m$ /MPa	$E_{pr}/E_m$	Plastic extension	<i>n</i>	Ferrite hardness HV
0	268	567	0.47	0.24	0.37	295
24	268	572	0.47	0.24	0.35	350
168	278	583	0.48	0.23	0.33	419
720	299	573	0.52	0.22	0.36	465
4320	317	646	0.49	0.22	0.36	537
8760	327	656	0.50	0.23	0.35	589
17520	350	675	0.52	0.19	0.36	648

$E_{pr}$  is the stress at the end of proportionality  $\epsilon - E$

$E_m$  is the maximum stress before the start of the reduction of area

Plastic extension is the extension between the points  $E_{pr}$  and  $E_m$

*n* is the approximate exponent of strain hardening

than at 290 °C and, as only the exponent of strain hardening is higher at 290 °C, the assumption is confirmed that the higher notch toughness is related to the share of energy consumed before the crack initiation at the notch tip,<sup>11</sup> which is greater at 290 °C than at room temperature. The difference reflects the effect the difference in the shape of the notch test specimen and the loading geometry, the asymmetrical flexion for the notch toughness test and the axial-symmetry for the tensile test.

#### 4 CONCLUSIONS

With the analysis of the stress-strain curves for specimens with a duplex austenite-ferrite microstructure and different ferrite hardnesses obtained with tests at room temperature and 290 °C it was established that with a higher temperature the strain hardening of the austenite matrix is greater than at room temperature. This finding is in agreement with the explanation that the greater share of energy consumed before the crack is opened at the notch tip is the cause of the higher notch toughness at 290 °C, although the tensile properties are higher at room temperature.

The authors are grateful to the Slovenian Research Agency and to Nuclear Power Plant Krško for their support of this investigation. The assistance of Ms B. Breskvar and D. Kmetič in the preparation of the alloy and the heat treatment of specimens is acknowledged.

#### 5 REFERENCES

- F. Vodopivec, M. Pristavec, J. Žvokelj, D. Gnidovec, F. Grešovnik: *Zeitschrift für Metallkunde*, 79 (1988), 648–653
- F. Vodopivec, D. Gnidovec, B. Arzenšek, M. Torkar, B. Breskvar: *Železarski Zbornik*, 23 (1989), 73–78
- F. Tehovnik, submitted for printing in *Materiali in Tehnologije & Materials and Technology*
- G. Slama, P. Petrequin, T. Mager: Assuring structural integrity of steel reactor pressure boundary components: SMIRT post-conference seminar, 1983, Monterey, USA, 211
- C. Jansson: Degradation of cast stainless steel elbows after 15 years of service: Fontenraud III-International Symposium, Royal Abbey of Fontenraud-Franc, September, 1990, 1/8–8/8
- H. M. Chung, T. R. Leax: *Mater. Sci. Techn.*, 6 (1990), 249
- O.K. Chopra: Estimation of mechanical properties of cast stainless steels during thermal ageing in LWR; *Trans. 13th Intern. Conf. On structural mechanics and reactor technology*, Porto Allegre, Brazil, August 1995
- S. Jayet-Gendrot, P. Ould, T. Meylogan: *Nucl. Eng. Des.*, 184 (1998), 3–11
- J. Kwom, S.Woo, Y. Lee, J-C Park, Y-W Park: *Nucl. Eng. Des.*, 206 (2001), 35–44
- J. Vojvodič-Tuma, B. Šuštaršič, F. Vodopivec: *Nucl. Eng. Des.*, 238 (2008), 1511–1517
- J. Vojvodič-Tuma, B. Šuštaršič, R. Celin, F. Vodopivec: *Materiali in Tehnologije & Materias and Technology* (in print)
- F. Vodopivec, B. Arzenšek, J. Vojvodič-Tuma, R. Celin: *Metalurgija*, 47 (2008), 173–179
- D. Mc Lean: *Trans. Metall. Soc. AIME* 242 (1968), 1193–1203
- G. E. Dieter: *Mechanical metallurgy*, McGraw-Hill, Boston, USA, 1986, 287
- F. Vodopivec, B. Arzenšek, J. Vojvodič-Tuma, R. Celin: *Metalurgija*, 47 (2008), 173–179



# IDENTIFICATION OF MATERIAL PROPERTIES OF QUASI-UNIDIRECTIONAL CARBON-EPOXY COMPOSITE USING MODAL ANALYSIS

## IDENTIFIKACIJA MATERIALNIH LASTNOSTI ZA KVAZIENOSMERNI KOMPOZIT OGLJIK-EPOKSI Z MODALNO ANALIZO

**Robert Zemčík, Radek Kottner, Vladislav Laš, Tomáš Plundrich**

Faculty of Applied Sciences, Department of Mechanics, University of West Bohemia  
Univerzitní 8, 306 14 Plzeň, Czech Republic  
zemcik@kme.zcu.cz

*Prejem rokopisa – received: 2008-10-13; sprejem za objavo – accepted for publication: 2009-04-30*

This work focuses on the identification of material parameters of carbon-epoxy composite with continuous ultrahigh modulus fibers. The tested structure is a cantilever beam with a rectangular cross-section manufactured with forming several fiber bundles together, each wrapped with transverse layer of fibers. The wrapping fibers provide additional strength in transverse loading. The eigen-frequencies of the beam are experimentally assessed using piezoelectric transducers and laser sensor. Corresponding modal analysis is performed using finite element method and the axial Young's modulus is deduced with the mathematical optimization by minimizing the difference between measured and calculated eigen-frequencies. The model is then verified with transient analysis when the piezoelectric patches are excited by harmonic signals covering the first two eigen-frequencies.

Keywords: piezoelectric, composite, identification, finite element

Težišče dela je na identifikaciji materialnih parametrov za kompozit ogljik-epoksi iz neprekinjenih vlaken z ultravelikim modulom. Preizkušena struktura je konzolni nosilec s pravokotnim prerezom, izdelan s povezavo snopov vlaken ovitih s prečnimi plastmi vlaken, ki zagotavljajo dodatno trdnost pri prečni obremenitvi. Lastne frekvence nosilca smo eksperimentalno določili z uporabo piezoelektričnih transduktorjev in laserskih senzorjev. Modalno analizo smo izvršili z uporabo končnih elementov, osni Youngov modul pa je bil določen z matematično optimizacijo z minimaliziranjem razlike med izmerjenimi in izračunanimi lastnimi frekvencami. Model je bil nato preverjen s tranzientno analizo, pri kateri so bili piezoelektrični merilniki vzbujeni s harmonskim signalom, ki je obsegal dve prvi lastni frekvenci.

Ključne besede: piezoelektrik, kompozit, identifikacija, končni elementi

## 1 INTRODUCTION

Light-weight structures are nowadays necessary components in modern state-of-the-art products in all sorts of industries. These structures usually utilize the composite materials in various form, such as shell-like laminates made from unidirectional layers or fabrics, wound or pultruded tubes and other profiles, or thick-walled components made by sandwiching composite skins and foam cores<sup>1,2,3,4</sup>.

The increasing requirements on structural performance call for the use of embedded sensors and actuators and the construction of the so-called adaptive, smart or even intelligent structures that can respond to loading conditions in real time<sup>10</sup>. This enables, for instance, to monitor the condition of the structure<sup>5</sup>, suppress vibrations or to adapt the desired shape<sup>1,8</sup>, provided that proper electronic control circuits are applied.

Commonly used types of sensors and actuators are based on piezoelectric materials. The finite element modeling of the piezoelectric materials began with the first implementation in 1970<sup>2</sup>. Many models have then been developed to simulate the piezoelectric effect,

ranging from the simples using the similarity to the theory of thermo-elasticity to models<sup>3</sup>, multi-purpose elements programmed for commercial software<sup>11,12</sup>, up to complex models with full piezoelectric coupling incorporating layerwise approach for electric potential across layers<sup>7</sup> or quadratic variation of electric potential across the layer thickness<sup>6</sup>.

The purpose of this work is to set up numerical model of composite beam with novel material structure and to use the piezoelectric actuators to identify the structural properties using experiment and the corresponding numerical simulation. This should be further extended for the application of monitoring the structural health in the future.

## 2 ANALOGY BETWEEN PIEZOELECTRICITY AND THERMAL EXPANSION

Let us consider the theory of piezoelectricity which assumes a symmetrical hexagonal piezoelectric structure and only the laminar piezoelectric effect (also called  $d_{31}$  effect, both direct and converse), i.e., the material is

polarized in the thickness direction and the electric potential varies linearly across the thickness <sup>9</sup>.

The classical stress-strain law (Hooke's law)

$$\sigma = C\varepsilon \tag{1}$$

$\sigma$  being the stress vector,  $C$  stress-strain matrix and  $\varepsilon$  the strain vector, is extended in this case by the piezoelectric coupling, hence

$$\sigma = C\varepsilon - eE \tag{2}$$

$$D = e^T \varepsilon + \epsilon E$$

where  $e$  is the piezoelectric coupling matrix,  $E$  is the electric field vector,  $D$  is the vector of electric flux density (electric displacement), and  $\epsilon$  is the dielectric permittivity matrix.

In many applications, the electric potential can be considered as known (the piezoelectric material is in the actuator mode) and, therefore, the second equation in (2) does not need to be solved for the electro-mechanical behavior. This allows to model the problem of piezoelectricity using the analogy with thermal expansion <sup>3</sup>. This can prove very helpful if the used software does not contain piezoelectric features.

The stress-strain law with thermal expansion for one-dimensional problem can be written as

$$\sigma = E(\varepsilon - \alpha\Delta T) \tag{3}$$

where  $E$  is the Young's modulus,  $\alpha$  the coefficient of thermal expansion and  $\Delta T$  the change in temperature. The corresponding piezoelectric equation is

$$\sigma = E\varepsilon - e \frac{U}{d} \tag{4}$$

with  $U$  being the voltage across electrodes and  $d$  the distance between the electrodes. The analogy is obvious and it is possible to write directly the resemblance between

$$\alpha \approx \frac{e}{E} \text{ and } \Delta T \approx \frac{U}{d} \tag{5}$$

### 3 EXPERIMENT

Experimental investigation of oscillations caused by harmonic excitations of quasi-unidirectional composite beam was carried out. The beam consists of unidirectional (0 degree) PITCH carbon fiber (K63712) sections each wrapped by 90 degree fibers and then stacked altogether. The matrix is composed of epoxy anhydride resin. The dimensions of the cross-section (see **Figure 1**) were (30 × 20) mm and the density was assessed to be  $\rho = 1838 \text{ kg/m}^3$ . The beam was made by CompoTech company.

Two collocated piezoelectric patches DuraAct P876.A12 (see **Figure 2**) were glued with HBM Z70 glue to the beam upper and lower surfaces. The dimensions of the patch are (61 × 35 × 0.5) mm while, the size of the active piezoelectric material ( $E = 61.8 \text{ GPa}$ ,  $e =$

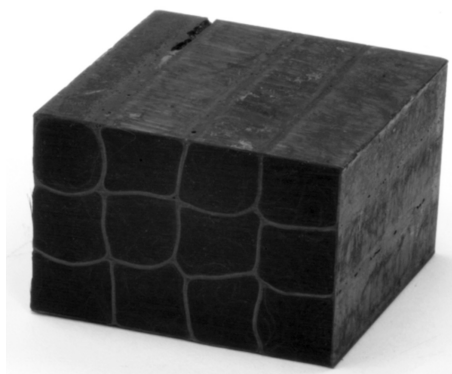


**Figure 1:** The cross-section of the composite beam showing the wrapped unidirectional sections

**Slika 1:** Prečni prerez kompozitnega nosilca, ki prikazuje ovite osne dele



**Figure 2:** Top and bottom view of the DuraAct P876.A12 piezoelectric transducers (patches)

**Slika 2:** Pogled od zgoraj in od spodaj piezoelektričnega transduktorja DuraAct P876. A12

$5.6 \text{ C/m}^2$ ,  $\rho = 7760 \text{ kg/m}^3$ ), which is enclosed in a protective foil ( $E = 8.2 \text{ GPa}$ ,  $\rho = 1528 \text{ kg/m}^3$ ), was of only (50 × 30 × 0.2) mm.

The beam of the free length of 1312 mm was clamped at one end so that the gap between the fixture and the active piezoelectric area was 10 mm. The piezoelectric patches were loaded by a sine signal from the generator ( $\pm 2\text{V}$ ) connected to voltage multiplier (50 times) with final amplitude of 100 V. The connection of patches resulted in bending of the beam. Laser sensor OptoNCDT was used to measure the deflections of the free end. The scheme of the experimental setup is shown in **Figure 3**.

The two lowest bending eigen-frequencies of the structure were found by sweeping the generator fre-

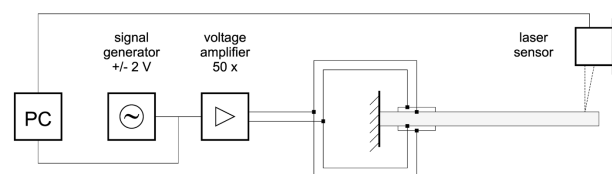


**Figure 3:** Scheme of experimental setup

**Slika 3:** Shema eksperimentalne postavitve

quency and searching for the largest steady oscillations. The values are  $f_1 = 21$  Hz and  $f_2 = 134$  Hz. The latter analysis investigated the response to frequencies around the two eigen-frequencies, namely the intervals  $\langle 15, 25 \rangle$  Hz and  $\langle 125, 140 \rangle$  Hz. The amplitudes of the steady oscillations  $A$  were measured for each frequency using the laser sensor.

*Numerical analysis*

Finite element model of the investigated structure was designed in MSC.Marc/Mentat software utilizing the analogy between piezoelectricity and thermal expansion as introduced in (5). The beam consisted of eight-node solid elements (with assumed strain option) as shown in **Figure 4**. The prescribed boundary conditions for the simulation of the clamped part are shown in **Figure 4**, also. The detail of how the materials were modeled within the structure is obvious from the cross-section displayed in **Figure 5**.

The elasticity properties of the new material structure were unknown. Since only the bending behavior was of

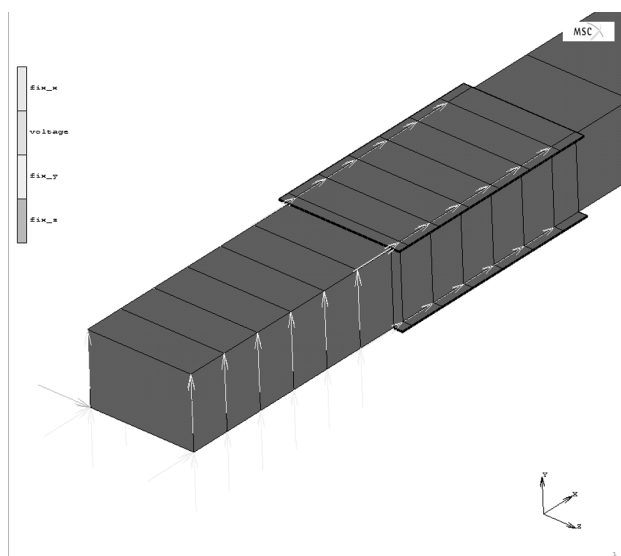


**Figure 4:** Finite element model of beam with attached piezoelectric patch and applied boundary conditions

**Slika 4:** Končnoelementni model nosilca s pritrjenimi piezoelektričnimi merilniki in uporabljene mejne vrednosti



**Figure 5:** Detail of beam and patch cross-section

**Slika 5:** Detajl prečnega prereza nosilca in merilnika

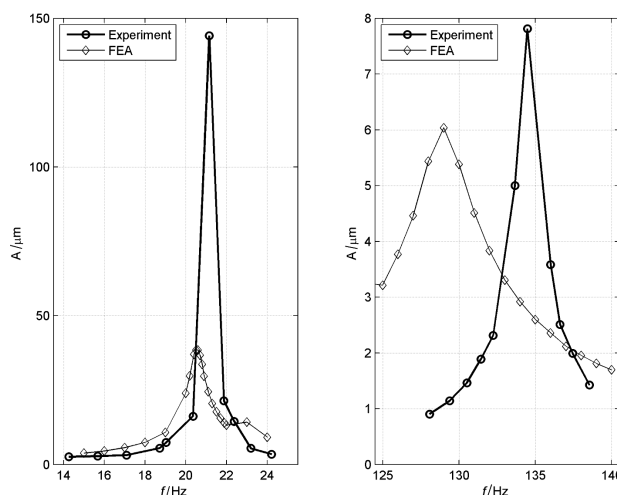


**Figure 6:** Amplitude characteristics around first two eigen-frequencies

**Slika 6:** Značilnosti amplitud okoli prvih dveh lastnih frekvenc

interest, it was possible to assume the composite and piezoelectric materials to be homogeneous and isotropic (the elasticity constants correspond to axial components, Poisson’s ratios  $\nu = 0.3$ ). The goal in this work was therefore to identify at least the Young’s modulus from the comparison of experiment and numerical model. Simple optimization loop with interval partitioning was used to minimize the error

$$\Delta = \sum_{i=1}^2 \left\{ \left( f_i^{EXP} - f_i^{FEA} \right)^2 \right\} \quad (6)$$

where  $f_i^{EXP}$  and  $f_i^{FEA}$  are the measured and calculated eigen-frequencies, respectively. The optimal value of Young’s modulus was found to be 245 GPa whereas the corresponding frequencies differed by less than 1 %.

The following investigation focused on the comparison of the measured frequency characteristics of the composite beam with the results of the numerical model. The piezoelectric material was excited by harmonic signals covering similar spectra as the experimental. The calculated and measured amplitudes of steady oscillations  $A$  are shown in **Figure 6**. The decrease in eigen-frequencies (given by the peaks in the graphs) from those obtained by modal analysis (approx. by 3 %) and in the maximum amplitudes can be explained using of the single-step Houbolt time integration scheme in MSC.Marc. The time step was set to 1/50 of the corresponding signal period.

**4 CONCLUSIONS**

The experimental analysis of frequency characteristics of hybrid composite cantilever beam was carried out. The beam consists of carbon-fibers and epoxy anhydride resin. Two collocated piezoelectric patches glued to its surface were applied to induce bending.

Corresponding finite element model was designed in MSC.Marc/Mentat software using the analogy between piezoelectricity and thermal expansion. The axial modulus of the quasi-unidirectional material was identified by modal analysis using simple optimization loop with interval partitioning. Moreover, the comparison of the calculated and measured frequency characteristics when the piezoelectric actuators were excited with harmonic signals around the first two eigen-frequencies was performed.

### Acknowledgements

The work has been supported by the research project MSM 4977751303 and by project GA CR 101/08/0299.

### 5 REFERENCES

- <sup>1</sup> Advancements and Challenges for Implementation: Structural Health Monitoring 2005. Edited by Fu-Kuo Chang, DEStech Publications Inc., 2005
- <sup>2</sup> Allik H., Hughes T. J. R., Finite element method for piezoelectric vibration. *International Journal for Numerical Methods in Engineering*, 2 (1970), 151–157
- <sup>3</sup> Benjeddou A., Advances in piezoelectric finite element modeling of adaptive structural elements: a survey. *Computers and Structures*, 76 (2000), 347–363
- <sup>4</sup> Berthelot J.-M., *Composite materials, Mechanical behavior and structural analysis*. Springer, Berlin, 1998
- <sup>5</sup> *Damage Prognosis: For Aerospace, Civil and Mechanical Systems*. Edited by D. J. Inman, C. R. Farrar, V. Lopes Jr., V. Steffen Jr., John Wiley & Sons, 2005
- <sup>6</sup> Kögl M., Bucalem M. L., Analysis of smart laminates using piezoelectric MITC plate and shell elements. *Computers and Structures*, 83 (2005), 1153–1163
- <sup>7</sup> Mitchell J. A., Reddy J. N., A refined hybrid plate theory for composite laminates with piezoelectric laminae. *Int. J. Solids Structures*, 32 (1995) 16, 2345–2367
- <sup>8</sup> *Proceedings of the Third European Workshop: Structural Health Monitoring 2006*. Edited by Alfredo Guemes, DEStech Publications Inc., 2006
- <sup>9</sup> Tzou H. S., *Piezoelectric shells. Distributed sensing and control of continua*. Kluwer Academic Publishers, 1993
- <sup>10</sup> Varadan V., Vinoy K. J., Gopalakrishnan S., *Smart Material Systems and MEMS: Design and Development Methodologies*. John Wiley & Sons, 2006
- <sup>11</sup> Zemčík R., Rolfes R., Rose M., Tessmer J., High-performance 4-node shell element with piezoelectric coupling. *Mechanics of Advanced Materials and Structures, Special Issue: Smart Composites*, Edited by J. N. Reddy and A. Benjeddou, 13 (2006) 5, 393–401
- <sup>12</sup> Zemčík R., Rolfes R., Rose M., Tessmer J., High-performance four-node shell element with piezoelectric coupling for the analysis of smart laminated structures. *Int. J. Numer. Meth. Engng.*, 70 (2007), 934–961

# RE-OXIDATION PHENOMENA DURING THE FILTRATION OF STEEL BY MEANS OF CERAMIC FILTERS

## REOKSIDACIJSKI PROCESI MED FILTRIRANJEM JEKLA S KERAMIČNIMI FILTRI

<sup>1</sup>Karel Stránský, <sup>2</sup>Jiří Bažan, <sup>2</sup>Jana Dobrovská, <sup>3</sup>Antonín Rek, <sup>2</sup>Dana Horáková

<sup>1</sup>VUT Brno, FSI, Technická 2, 616 69 Brno, Czech Republic

<sup>2</sup>VŠB-Technical University of Ostrava, Czech Republic

<sup>3</sup>ÚPT Academy of Science, Brno, Czech Republic

stransky@fme.vutbr.cz

*Prejem rokopisa – received: 2008-10-13; sprejem za objavo – accepted for publication: 2009-03-27*

This paper presents the results of experiments on the filtering of the melt of carbon steel with the use of five types of ceramic filters with direct holes, which differed in terms of their basic ceramic nature. The objective of the experiments was to determine the influence of filter ceramics on the re-oxidation reactions and the reactions between the filter ceramics and molten steel flowing through the filter capillaries. The metallurgical and metallographic cleanliness of the steel filtered through individual types of filters was also assessed.

Key-words: filtration of steel, ceramic filters, capillary tube re-oxidation, micro-cleanliness of steel

V članku so prikazani rezultati preizkusov filtriranja ogljikovega jekla s filtri iz keramike različne sestave in z neposrednimi kapilarami. Cilj preizkusov je bil ugotoviti vpliv filtne keramike na reakcije reoksidacije in naravo reakcij med to keramiko in jeklom, ki teče skozi kapilare. Metalurška in metalografska čistota jekla sta bili tudi ocenjeni.

Ključne besede: filtriranje jekla, keramični filtri, reoksidacija v filtrnih kapilarah, mikročistost jekla

## 1 INTRODUCTION

Re-oxidation processes accompany the de-oxidised steel from the furnace or from the ladle till its final

solidification in the mould or in the ingot-mould. The main products of re-oxidation processes are usually non-metallic oxide inclusions formed first from the elements with a higher affinity for oxygen, and progressively with the re-oxidation of elements with decreasing and finally with a very low affinity for oxygen. Among the elements present in the molten steel, iron and manganese, silicon, and chromium, etc. <sup>1-4</sup> are re-oxidised.

The paper presents the results of experiments of the filtration of molten carbon steel using five types of ceramic filters with direct holes, which differed in terms of their primary ceramic basis. The experiments and analyses of the chemical composition were aimed at determining the influence of filter ceramics on the course of re-oxidation processes and at assessing the reactions between the filter ceramics and the molten steel flowing through the filter capillaries. The aim of the experiments was also to evaluate the metallurgical and metallographic cleanliness of the steel filtered with use of individual types of filters.

## 2 CHANGES OF THE CHEMICAL COMPOSITION OF THE CAPILLARIES' CERAMIC SURFACE DURING FILTRATION

The five types of ceramic filters used for the verification of re-oxidation processes consisted of combinations of the following types of oxides: A – TiO<sub>2</sub> ·

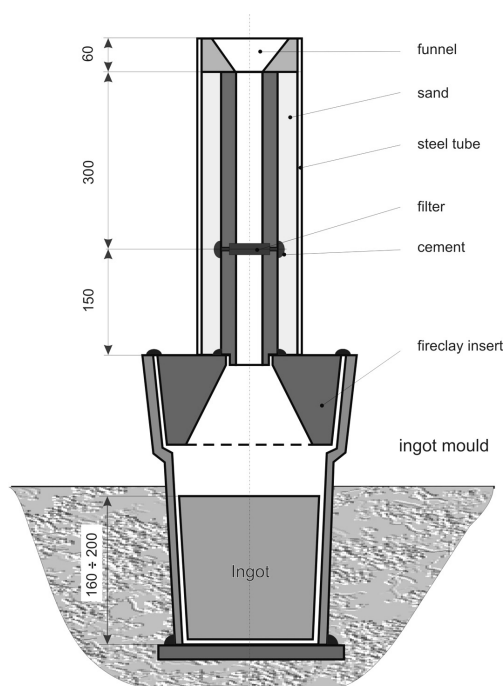


Figure 1: Design and placement of the ceramic filter

Slika 1: Shema in postavitev filtra

ZrO<sub>2</sub>; B – Al<sub>2</sub>O<sub>3</sub> · TiO<sub>2</sub>; C – MgO · Al<sub>2</sub>O<sub>3</sub>; D – Al<sub>2</sub>O<sub>3</sub> · ZrO<sub>2</sub>; E – Al<sub>2</sub>O<sub>3</sub> · SiO<sub>2</sub>. The specimens of ceramic filters were prepared in the company KERAMTECH, spol. s. r. o., Žacléř, Czech Republic. The sequence of the preparation of the experimental steel samples was melting of the steel, stabilisation at a temperature of 1650 °C, addition of pure aluminium and silicon-calcium for de-oxidation of the molten steel prior to filtration and at the same time the addition of a determined quantity of iron sulphide (FeS) into the molten steel intended to determine the reduction of sulphur content during the flow of the molten steels through the filter. Then the specimens for the determination of the initial chemical composition and filtration of the steel through individual types of filters were cast. During filtration the steel flowed through the filter and (*solidified*) above the filter, in the filter itself and in the filtered casting (sample). **Figure 1** shows the filtering scheme.

The chemical composition was determined with energy-dispersive X-ray spectral micro-analysis using the analytical systems JEOL JXA-8600/ KEVEX and JEOL JSMU 840/LINK. The results of the chemical analysis at the surface layer of the capillaries of the ceramic filters during the filtration of the initial chemical composition of the filter ceramics, which had no contact with the filtered melt, are summarised in **Table 1**. The working identification "*coating*" was used for the different chemical compositions of the surface of the ceramics after filtration. In **Table 1** the *differences* in the chemical composition of the *ceramics-coating*, (i.e., the difference between the original chemical composition of the ceramics and the chemical composition of the coating), in which the symbol (–) means decrement, and the symbol (+) means increment of an oxidic component of ceramics on the surface of the coating in mass fractions (%), are shown. The chemical composition of the

used ceramics is marked in **Table 1** in bold characters. The chemical composition of basic oxidic components of the filter ceramics and the chemical composition of the oxidic components of the coating were determined as an arithmetic mean of two measurements.

It follows from the analyses of the chemical composition in Table 1 that in the whole series of five ceramic filters, which have a different oxidic base, the processes of adsorption of the flowing molten steel occur, which are related to the formation of the coating on the surface of the filter capillaries. Physical-chemical reactions occur between the flowing molten steel and the ceramic of the filter capillaries, and the initial ceramic composition is changed and a coating is formed on the surface of the capillaries. In this coating the chemical composition of the primary thermodynamically stable oxides is reduced and particularly the share of the oxides MnO and Fe<sub>2</sub>O<sub>3</sub> is increased. The sum of the contents of both types of oxides in the capillaries' coating, i.e., MnO + Fe<sub>2</sub>O<sub>3</sub>, has a positive value for the whole series of filters A to E (see the **Table 1**). Both types of oxides are formed as a result of re-oxidation processes.

The ratios given in Table 1 are also given in a graphical representation. The changes of the chemical composition of the coating on the surface of filter capillaries were compared as a ratio of the sums of the concentrations of the decrements of the basic ceramic components for the investigated series of five filters A to E to the increments of the sums of the oxide MnO and Fe<sub>2</sub>O<sub>3</sub> contents formed in the coating as a result of re-oxidation. This comparison is shown in bar form in **Figure 2**. It can be concluded from **Figure 2** that the sum of the changes in the composition of basic oxidic components in the filter ceramics on the coating of the capillaries (which – according to the analyses in **Table 1** – always has a negative value) is in all the investigated

**Table 1:** Changes in the chemical composition of the ceramics on the surface of the walls during the coating of the filter capillaries. The symbol (–) means decrement, the symbol (+) means increment of an oxide component of ceramics on the surface of the coating (w/%)

**Tabela 1:** Sprememba sestave keramike na površini kapilar. Simbol (–) pomeni zmanjšanje, simbol (+) pa povečanje neke oksidne komponente keramike na površini kapilare.

Filter	MgO	Al <sub>2</sub> O <sub>3</sub>	SiO <sub>2</sub>	TiO <sub>2</sub>	S	K <sub>2</sub> O	CaO	ZrO <sub>2</sub>	MnO	Fe <sub>2</sub> O <sub>3</sub>	
A	ceramics	2.09	7.55	13.04	<b>41.60</b>	0.00	0.62	0.16	<b>33.42</b>	0.07	1.96
	coating	0.82	3.16	4.08	<b>35.94</b>	0.00	0.14	0.09	<b>45.14</b>	0.73	9.92
	difference	–1.27	–4.39	–8.96	<b>–5.66</b>	0.00	–0.48	–0.07	<b>+11.72</b>	+0.66	+7.96
B	ceramics	0.23	<b>48.48</b>	11.62	<b>37.17</b>	0.15	0.50	0.07	0.00	0.08	1.12
	coating	0.51	<b>48.99</b>	12.34	<b>30.55</b>	0.12	0.20	0.47	0.00	4.55	1.67
	difference	+0.28	<b>+0.51</b>	+0.72	<b>–6.62</b>	–0.03	–0.30	+0.40	0.00	+4.47	+0.55
C	ceramics	<b>21.52</b>	<b>49.50</b>	22.97	0.75	0.22	0.67	0.41	0.00	0.11	3.29
	coating	<b>20.06</b>	<b>48.80</b>	23.88	0.69	0.11	0.64	0.53	0.00	1.95	2.92
	difference	–1.46	–0.70	+0.91	–0.06	–0.11	–0.03	+0.12	0.00	+1.84	–0.37
D	ceramics	3.58	<b>54.63</b>	11.52	0.30	0.00	0.30	0.12	<b>27.41</b>	0.15	2.51
	coating	1.95	<b>27.68</b>	22.80	0.18	0.00	0.40	0.35	<b>13.15</b>	13.51	20.01
	difference	–1.63	–26.9	+11.30	–0.12	0.00	+0.10	+0.23	–14.26	+13.36	+17.50
E	ceramics	3.78	<b>31.62</b>	<b>57.17</b>	1.01	0.10	0.93	0.32	0.00	0.09	4.45
	coating	2.73	<b>34.00</b>	<b>53.47</b>	1.13	0.11	1.56	0.62	0.00	0.27	5.24
	difference	–1.05	<b>+2.38</b>	–3.70	+0.12	+0.01	+1.24	+0.30	0.00	+0.18	+0.79

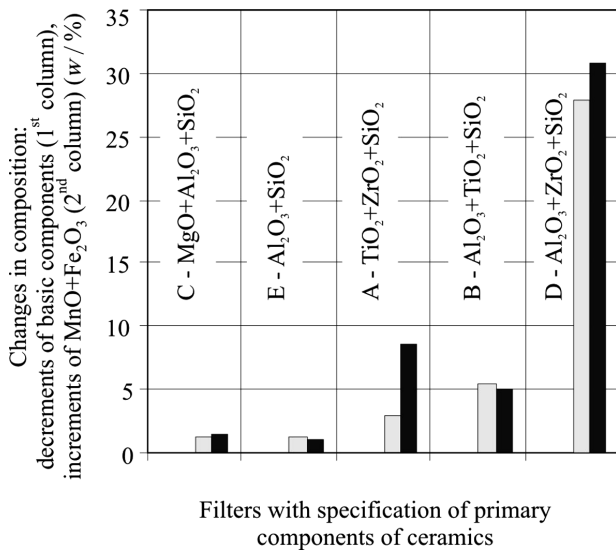


**Figure 2:** Decrements and increments of oxides in the coating of the filter capillaries

**Slika 2:** Zmanjšanje in povečanje vsebnosti oksidov v oblogi v kapilarah

types of filter compensated by an increment of the sum of the less-stable manganese and iron oxides, formed with the re-oxidation of the filtered molten steel.

The relationship between the sum of the decrements and increments in the coating can also be expressed analytically with the diagram in **Figure 3**, which corresponds to the straight-line equation

$$(\text{Increment of MnO} + \text{Fe}_2\text{O}_3) = 3.97 + 0.606 \cdot (\text{sum of the decrements in the composition of the oxides of the basis of filter ceramics}), \quad (1)$$

with a correlation coefficient of  $r = 0.9069$ , while the critical value of the same quantity for  $\nu = 5 - 2 = 3$  degrees of freedom has the confidence level  $\alpha = 0.05$  and  $r_{\text{krit}} = 0.8783$ .

The obtained results of the analyses show that the decrement of the sum of the oxides of the basic ceramics is replaced by the increment (in fact with the sum) of the oxide MnO and the iron oxides (Fe<sub>2</sub>O<sub>3</sub>) in the coating of the capillaries of individual filters. This observation is related to the physical-chemical reactions of re-oxidation processes during the filtration that should be considered during the steel filtration.

### 3 METALLURGICAL CLEANLINESS OF THE FILTERED STEEL

The results of the assessment of the metallurgical cleanliness of the molten steel filtered with the checked filters A to E are summarised in **Table 2**. The chemical composition of the non-filtered steel was determined from a sample taken above the filter, while the chemical composition of the filtered steel was determined from a sample taken from the casting below the filter.

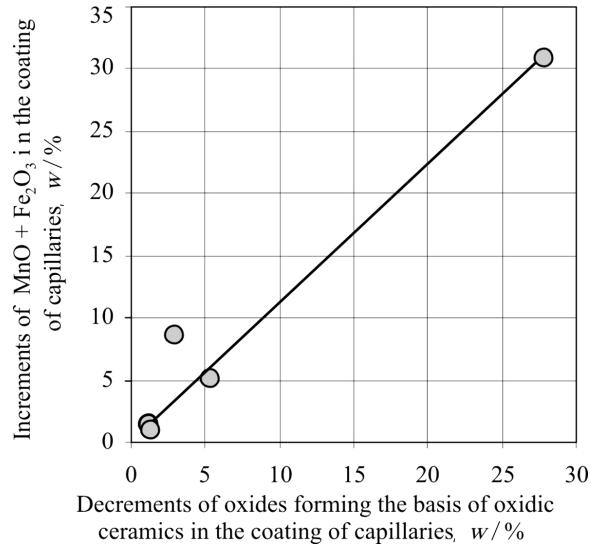


**Figure 3:** Relation between the decrements and increments of the oxides in the coating of the filter capillaries

**Slika 3:** Razmerje med zmanjšanjem vsebnosti enih in povečanjem vsebnosti drugih oksidov v oblogi v kapilarah filtrov

The table also gives an efficiency of the filtration of the individual filters. It is obvious from the data that the filtration efficiency is different for elements that form oxides – i.e., calcium, aluminium and oxygen – and for elements that form nitrides and sulphides – i.e., nitrogen and sulphur – as shown in **Figure 4**. The filtration efficiency for elements forming oxides in steel is, on average, i.e., without consideration of the type of ceramic filter (for all types of filter), approximately four times higher than for elements forming in steel nitride or sulphide inclusions.

The symbols in **Figure 4** mean the following:  $\eta$  (Ca<sub>z</sub>),  $\eta$  (Al<sub>z</sub>),  $\eta$  (O<sub>z</sub>) – average efficiencies of the whole series of five filters for the elements forming oxides, and  $\eta$  (N<sub>z</sub>) and  $\eta$  (S) – average efficiencies of the

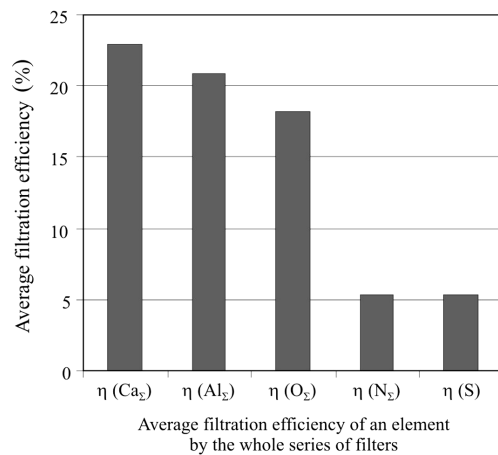


**Figure 4:** Filtration efficiency for the elements Ca, Al, O, N, S

**Slika 4:** Povprečna učinkovitost za elemente Ca, Al, O, N in S. Simboli  $\eta$  (Ca<sub>z</sub>),  $\eta$  (Al<sub>z</sub>),  $\eta$  (O<sub>z</sub>) – povprečne učinkovitosti vseh filtrov za elemente, ki tvorijo okside;  $\eta$  (N<sub>z</sub>) in  $\eta$  (S) – povprečne vseh filtrov za elemente, ki tvorijo sulfide in nitride.

**Table 2:** Metallurgical cleanliness of steel – chemical composition of steel prior to filtration and after filtration with the checked five filters w/% and the filtration efficiency  $\eta$ /%**Tabela 2:** Metalurška čistost jekla; kemična sestava jekla pred filtriranjem in po njem za vse preizkušane filtre w/% in učinkovitost filtriranja  $\eta$ /%

Element	Non-filtered	After filtration of molten steel by the given type of filter				
		A	B	C	D	E
S	0.045	0.042	0.044	0.040	0.043	0.044
Al <sub>Σ</sub>	0.189	0.163	0.128	0.164	0.134	0.159
O <sub>Σ</sub>	0.0278	0.0256	0.0240	0.0122	0.0257	0.0250
N <sub>Σ</sub>	0.0189	0.0184	0.0181	0.0168	0.0181	0.0180
Ca <sub>Σ</sub>	0.0028	0.0023	0.0021	0.0023	0.0023	0.0018
Efficiency $\eta$		A	B	C	D	E
$\eta$ (S)	–	6.7	2.2	11.1	4.4	2.2
$\eta$ (Al <sub>Σ</sub> )	–	13.8	32.3	13.2	29.1	15.9
$\eta$ (O <sub>Σ</sub> )	–	7.9	9.1	56.1	7.6	10.1
$\eta$ (N <sub>Σ</sub> )	–	2.6	4.2	11.1	4.2	4.8
$\eta$ (Ca <sub>Σ</sub> )	–	17.9	25.0	17.9	17.9	35.7
$\eta$ ( $\emptyset$ ): $s_x$	–	9.8	14.6	21.9	12.6	13.7
$s_x$	–	6.1	13.4	19.3	10.8	13.4

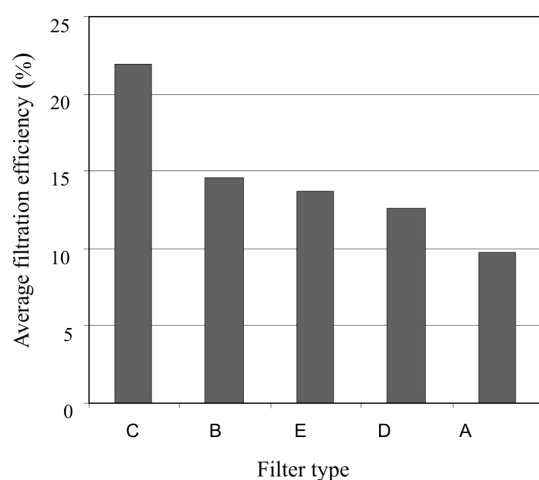
whole series of five filters for the elements forming nitrides and sulphides.

Notes: filtration efficiency

$$\eta = \frac{w(x_{\text{non-filtered}}) - w(x_{\text{filtered}})}{w(x_{\text{non-filtered}})}$$

symbol  $X_c$  means total content of the element in steel;  $x$  is the arithmetic mean; and  $s_x$  is the standard deviation.

The average filtration efficiency also depends on the type of ceramic filter (see **Table 1**) and it is different for each filter. The difference between the highest filtration efficiency of the filter C – MgO·Al<sub>2</sub>O<sub>3</sub> and lowest filtration efficiency of the filter A – TiO<sub>2</sub>·ZrO<sub>2</sub>, is more than double. The relation between the filtration efficiency of individual types of ceramic filters is shown in **Figure 5**. It is apparent from this figure that the filtration efficiency of the individual types of filters decreases in the given series of filters in the order C, B, E, D, A.

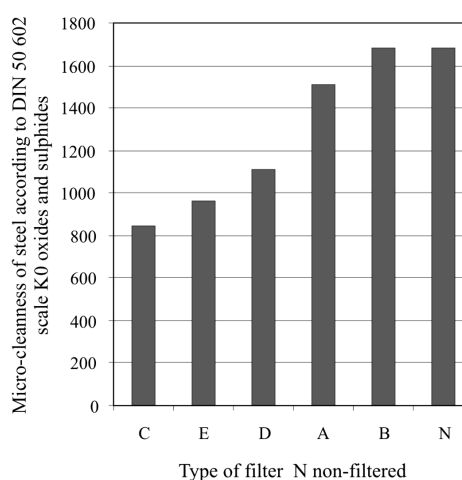
**Figure 5:** Filtration efficiency by type of filter**Slika 5:** Učinkovitost za vsak preizkušen filter

#### 4 METALLOGRAPHIC CLEANLINESS OF THE FILTERED STEEL

The assessment of the metallographic cleanliness of the filtered steel in terms of the quantity of the oxide and sulphide inclusions was performed in accordance with the standard DIN 50 602 and according to the K0 methodology, for the filtered and non-filtered steels.

A graphical representation of the metallographic cleanliness for the individual types of filters is shown in **Figure 6** and the filtration efficiency in % for the filters as an evaluation of the micro-cleanliness according to the DIN 50 602, scale K0 I, is shown in **Figure 7**.

The assessment of the metallographic micro-cleanliness of the steel according to DIN 50602, scale K0, indicates that the micro-cleanliness of the filtered steel decreases in the order C, E, D, A, B for the filters (**Figure 6**). Also, the filter efficiency – in terms of

**Figure 6:** Micro-cleanliness of filtered steel according to DIN 50 602**Slika 6:** Mikročistota filtriranega jekla po DIN 50 602

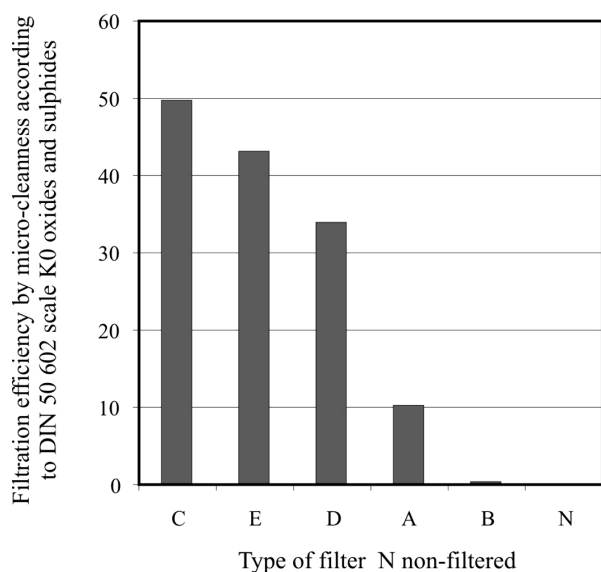


**Figure 7:** Filtration efficiency as micro-cleanliness according to DIN 50 602

**Slika 7:** Učinkovitost filtriranja po DIN 50 602

ensuring the minimum number of sulphide and oxide inclusions – decreases in the same order. Thus, the best micro-cleanliness is therefore ensured with filtration with the ceramic filter C –  $\text{MgO} \cdot \text{Al}_2\text{O}_3$ , and the lowest are the filter A –  $\text{TiO}_2 \cdot \text{ZrO}_2$  and, particularly, the filter B –  $\text{Al}_2\text{O}_3 \cdot \text{TiO}_2$ , with an efficiency of almost zero.

## 5 CONCLUSION

The paper presents results from the filtering of molten carbon steel with five types of ceramic filters with direct holes of different primary ceramic bases. The objective of the experiments was to determine the influence of filter ceramics on the re-oxidation reactions and to evaluate the reactions between the filter ceramics and the molten steel flowing through the filter capillaries. The metallurgical and metallographic clean-

liness of the steel filtered by individual types of filters was also assessed.

It was established that during the filtration of the molten steel with ceramic filters of different oxide bases of the used ceramics, the molten steel flowing through the filter reacted with the surface of the filter capillaries. The physical-chemical reactions between the molten steel and the filter ceramic form a coating on the surface of the capillaries in the coating. The chemical composition of the used ceramics is changed and it is enriched in the oxides of manganese and iron, which are formed as a result of re-oxidation processes during the filtration. The extent of the changes of the chemical composition is a function of the thermodynamic stability of the oxides forming the initial composition of the ceramic filters. The metallurgical and metallographic cleanliness of the same steel filtered through the different ceramic filters is very different.

This work was realised within the frame of the grant project reg. no. 106/06/0393 under the financial support of the Czech Grant Agency.

## 6 REFERENCES

- <sup>1</sup> Bažan, J., Stránský, K. *Flowing of the melt through ceramic filters*. Mater. Tehnol. / Materials and technology, 41 (2007) 2, 99–102. ISSN: 1580–2949
- <sup>2</sup> Stránský, K., Bažan, J., Dobrovská, J., Balcar, M., Fila, P., Martínek, L. *Application of the theory of physical similarity for the filtration of metallic melts*. Mater. Tehnol. / Materials and technology, 42, (2008) 4, 175–178. ISSN 1580–2949
- <sup>3</sup> Stránský, K., Bažan, J., Bůžek, Z., Rek, A., Belko, J. *On the Filtration of Steel by means of Different Types of Ceramics Filters*. In METAL 2001, TANGER, spol. s r.o. 10<sup>th</sup> International Metallurgical and Materials Conference. Proceedings, CD-ROM, ref. No. 123, ISBN 80-85988-56-9
- <sup>4</sup> Stránský, K., Bažan, Z., Bůžek, Z., Belko, J., Lev, P. *Príspevek k účinnosti filtrace ocelí různými typy keramických filtrů [Contribution to efficiency of steel filtration by various types of ceramic filters]*. In Hutní keramika. TANGER, spol. s r.o. and VŠB-TU Ostrava, FMML, Rožnov pod Radhoštěm 2001, pp. 123–130. ISBN 80-85988-64-X



## THE USE OF RESPONSE SURFACE METHODOLOGY FOR PREDICTION AND ANALYSIS OF SURFACE ROUGHNESS OF AISI 4140 STEEL

### UPORABA METODOLOGIJE ODGOVORA POVRŠINE ZA NAPOVED IN ANALIZO HRAPAVOSTI PRI JEKLU AISI 4140

**Funda Kahraman**

Mersin University, Tarsus Technical Education Faculty, Department of Mechanical Education, 33400 Tarsus-Mersin, Turkey

*Prejem rokopisa – received: 2009-03-23; sprejem za objavo – accepted for publication: 2009-06-08*

This paper utilizes regression modeling in turning process of AISI 4140 steel using Response Surface Methodology (RSM) with rotatable Central Composite Design (CCD). A quadratic model was developed for the prediction and analysis of the relationship between the cutting conditions and surface roughness. In the development of predictive models, cutting parameters of cutting speed, feed rate and depth of cut were considered as model variables, surface roughness were considered as a response variable. The statistical analysis showed that, cutting speed and feed rate have the most significant effect on surface roughness. The predicted values was found similar to the actual values. The alternative solutions of the optimization approach using desirability functions were used to determine the optimum processing conditions.

Keywords: turning, surface roughness, optimization, RSM (CCD)

V tem delu uporabljamo regresijsko modeliranje struženja jekla AISI 4140 po metodologiji odgovora površine (RSM) z vrtljivim središčnim kompozitnim načrtom (CCD). Kvadratičen model je bil razvit za napovedovanje in analizo odvisnosti med pogoji struženja in hrapavostjo površine. Pri razvoju napovedovalnih modelov so bili parametri struženja hitrost, podajanje in globina upoštevani kot spremenljivke modela, hrapavost površine pa kot spremenljivka odgovora. Statistična analiza je pokazala, da imata hitrost struženja in globina podajanja največji vpliv na hrapavost površine. Napovedane vrednosti so bile podobne izmerjenim. Za optimizacijo pogojev procesa so bile uporabljene alternativne želene funkcije.

Ključne besede: struženje, hrapavost površine, optimizacija, RSM (CCD)

## 1 INTRODUCTION

The surface quality is an important parameter to evaluate the productivity of machine tools as well as machined components. Hence, achieving the desired surface quality is of great importance for the functional behaviour of the mechanical parts. Surface quality is generally associated with surface roughness. The surface roughness of machined parts is known to have considerable effect on some properties such as wear resistance and fatigue strength<sup>1-3</sup>.

Several researchers have developed mathematical models to predict the surface roughness in terms of various process parameters during turning of different materials. Sahin and Motorcu<sup>1</sup> machined the hardened AISI 1040 steel with triangular and square tools in different machining conditions and modeled the surface roughness by using RSM. Sahin and Motorcu<sup>2</sup> developed the surface roughness model in terms of main cutting parameters such as cutting speed, feed rate and depth of cut using RSM. Kopac and Bahor<sup>3</sup> examined the changes in surface roughness of AISI 1060 and AISI 4140 steels and analyzed the effect of cutting parameters by using RSM. Noordin et al.<sup>4</sup> developed the empirical models such as linear and quadratic functions by using RSM to predict surface roughness and tangential force when turning AISI 1045 steel. Mansour et al.<sup>5</sup> studied a

surface roughness model that utilizing RSM for milling steel in dry condition. Arbizu and Perez<sup>6</sup> presented a surface roughness prediction model using RSM to determine surface quality in turning processes. Choudhury and El-Baradie<sup>7</sup> developed surface roughness prediction model in turning of high strength steel by factorial design of experiments. Erzurumlu and Oktem<sup>8</sup> discussed the effect of cutting parameters on surface roughness. They developed RSM and an artificial neural network (ANN) model to predict surface roughness values error on mold surfaces. Ozel and Karpat<sup>9</sup> used regression and ANN for predictive modeling of surface roughness and tool wear in hard turning. Nalbant et al.<sup>10</sup> examined Taguchi method in the optimization of cutting parameters for surface roughness in turning. Davim<sup>11</sup> studied the influence of cutting conditions on the surface finish obtained by turning, based on the techniques of Taguchi.

In this study, The Design-Expert software package was used to develop RSM model and to apply the desirability approach. RSM with CCD was adopted to obtain an empirical model of surface roughness (response) as a function of cutting speed feed rate and depth of cut (input factors). The optimum process conditions were determined by using desirability functions. Desirability function is an attractive method for industry for optimization of quality characteristic problems.

**2 EXPERIMENTAL DETAILS**

The cutting experiments were carried out a Goodway GS-280 industrial type of CNC lathe. HSS tool ( $\alpha = 8^\circ, \gamma = 14^\circ, r = 0.4 \text{ mm}$ ) was used for the machining of AISI 4140 steel bars with cutting fluid. The mean surface hardness of samples was measured as 195 HB after normalizing at 870 °C The chemical compositions of AISI 4140 steel is given in **Table 1**.

**Table 1:** Chemical composition of AISI 4140 steel in mass fractions, w/%

**Tabela 1:** Kemična sestava jekla AISI 4140

C	Mn	P	S	Si	Cr	Mo
0.38–0.43	0.75–1.00	0.035 max	0.040 max	0.15–0.30	0.80–1.10	0.15–0.25

These bars of 30 mm diameter and 200 mm in length were prepared. Test samples were trued, centered and cleaned by removing a 1 mm depth of cut ( $a_p$ ) from the outside surface, prior to actual machining tests. Three replications of each cutting conditions were conducted resulting in a total of 60 tests. A Mahr Perthometer-M1 type of portable surface roughness tester was used for measuring surface roughness. Input parameters of the models are cutting speed ( $v_c$ ), feed rate ( $f$ ) and depth of cut ( $a_p$ ). Output parameter of the models is the corresponding surface roughness ( $R_a$ ). Factors and levels for CCD are given in **Table 2**. The relationship between the coded factors and the actual factors are shown in Equations 1-3.

$$x_1 = \frac{\text{speed} - (\text{speed}_{low} + \text{speed}_{high}) / 2}{(\text{speed}_{high} - \text{speed}_{low}) / 2} \quad (1)$$

$$x_2 = \frac{\text{feed} - (\text{feed}_{low} + \text{feed}_{high}) / 2}{(\text{feed}_{high} - \text{feed}_{low}) / 2} \quad (2)$$

$$x_3 = \frac{\text{doc} - (\text{doc}_{low} + \text{doc}_{high}) / 2}{(\text{doc}_{high} - \text{doc}_{low}) / 2} \quad (3)$$

where  $x_1$  is the coded factor that represent the cutting speed,  $x_2$  is the coded variable that represent the feed rate,  $x_3$  is the coded variable that represent the depth of cut (doc).

**Table 2:** Factors and levels for CCD

**Tabela 2:** Faktorji in nivoji za CCD

Factors/Levels	-1.68	-1	0	+1	+1.68
Cutting speed ( $v_c$ )	16	47	92	137	167
Feed rate ( $f$ )	0.032	0.1	0.2	0.3	0.368
Depth of cut ( $a_p$ )	0.160	0.5	1	1.5	1.840

**3 DATA ANALYSIS AND DISCUSSION OF RESULTS**

The arrangement and the results of the 20 experiments carried out. Experimental and predicted surface

roughness values for CCD are shown in **Table 3**. The results of the model is given in **Table 4**. Significance level ( $\alpha$ ) was selected as 0.05. The value of  $p$  for the term of model is less than 0.05 indicates that the obtained model is considered to be statistically significant. This value ( $p < 0.0001$ ) showed that, the quadratic model fits well to the experimental results.

**Table 3:** Experimental and predicted surface roughness ( $R_a$ ) values for CCD

**Tabela 3:** Eksperimentalne in napovedane vrednosti za CCD

Run	Cutting speed $v_c$ / (m/min)	Feed rate $f$ / (mm/r)	Depth of cut $a_p$ / mm	Actual $R_a$ / $\mu\text{m}$	Predicted $R_a$ / $\mu\text{m}$
1	47	0.1	0.5	1.60	1.64
2	137	0.1	0.5	2.20	2.24
3	47	0.3	0.5	2.47	2.66
4	137	0.3	0.5	2.14	2.14
5	47	0.1	1.5	1.91	2.00
6	137	0.1	1.5	1.77	1.68
7	47	0.3	1.5	2.84	2.90
8	137	0.3	1.5	1.40	1.46
9	16	0.2	1	2.62	2.44
10	167	0.2	1	1.70	1.74
11	92	0.032	1	1.67	1.67
12	92	0.368	1	2.48	2.34
13	92	0.2	0.160	2.51	2.40
14	92	0.2	1.840	2.17	2.14
15	92	0.2	1	2.72	2.68
16	92	0.2	1	2.74	2.68
17	92	0.2	1	2.64	2.68
18	92	0.2	1	2.70	2.68
19	92	0.2	1	2.51	2.68
20	92	0.2	1	2.74	2.68

**Table 4:** The results of the model

**Tabela 4:** Rezultati modela

Source	Sum of Squares	df	Mean Square	F-value	p-value
Linear	1.23	3	0.41	2.44	0.102
Quadratic	1.47	3	0.35	2.81	<0.0001 suggested
Cubic	0.078	4	0.49	29.65	0.35

Quadratic regression equation was developed for predicting surface roughness ( $R_a$ ) within selected experimental conditions using RSM. Regression equation can be expressed as follows.

$$R_a = 2.68 - 0.21X_1 + 0.20X_2 - 0.078X_3 - 0.21X_1^2 - 0.24X_2^2 - 0.14X_3^2 - 0.28X_1X_2 - 0.23X_1X_3 \quad (4)$$

where  $x_1$  is cutting speed ( $v_c$ ),  $x_2$  is feed rate ( $f$ ),  $x_3$  is depth of cut ( $a_p$ ).

It is observed that cutting speed ( $v_c$ ) and depth of cut ( $a_p$ ) have negative influence, feed rate ( $f$ ) has positive influence on the surface roughness ( $R_a$ ). The surface roughness ( $R_a$ ) of AISI 4140 steel decreased with increasing cutting speed ( $v_c$ ) and depth of cut ( $a_p$ ) whereas increased with increasing feed rate ( $f$ ). The

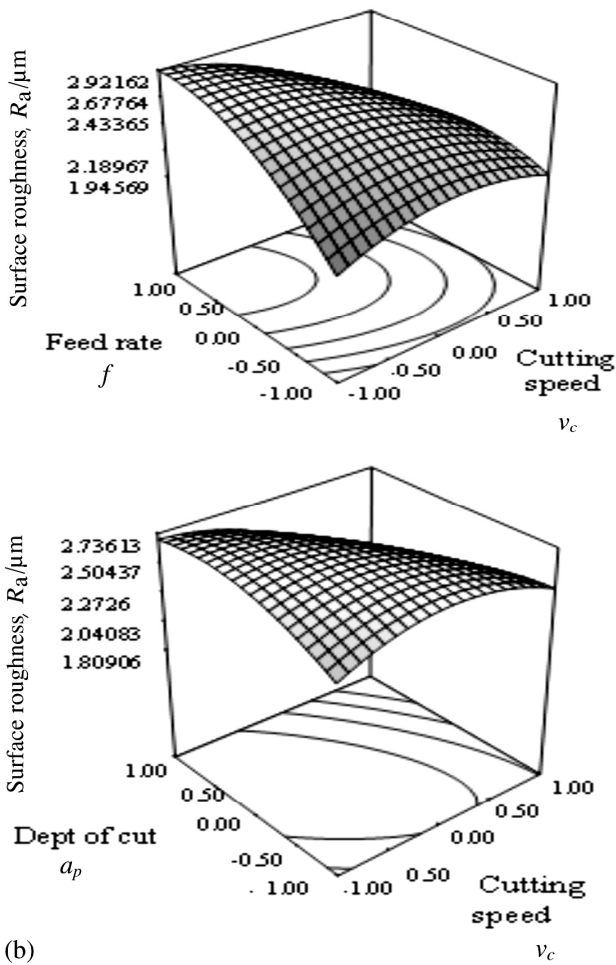


Figure 1: 3D response surface graphs for surface roughness ( $R_a$ )  
 Slika 1: 3D-graf odgovora za hrapavost površine ( $R_a$ )

Table 5: The ANOVA table for the quadratic model  
 Tabela 5: Anova tabela za kvadratičen model

Source	SS	DF	MS	F-value	p-value
Model	3.75	9	0.42	25.29	< 0.0001
$x_1$	0.60	1	0.60	36.29	< 0.0001
$x_2$	0.55	1	0.55	33.19	< 0.0002
$x_3$	0.083	1	0.083	5.01	0.0491
$x_1^2$	0.62	1	0.62	37.72	0.0001
$x_2^2$	0.81	1	0.81	49.43	< 0.0001
$x_3^2$	0.30	1	0.30	18.14	0.0017
$x_1x_2$	0.62	1	0.62	37.74	0.0001
$x_1x_3$	0.43	1	0.43	25.97	0.0005
$x_2x_3$	0.007813	1	0.007813	0.47	0.5067

relationship between cutting speed ( $v_c$ ) and feed rate ( $f$ ) is shown in Figure 1a, the relationship between cutting speed ( $v_c$ ) and depth of ( $a_p$ ) is shown in Figure 1b.

It can be realized that the combination between high cutting speed and high feed rate ( $f$ ) results in a considerable reduction in surface roughness ( $R_a$ ) and also between high cutting speed ( $v_c$ ) and high depth of cut results in a considerable reduction in surface roughness

( $R_a$ ). The response surface plot (Figure 1a) indicates that the minimum surface roughness is at about 137 m/min and 0.3 mm/r. The response surface plot (Figure 1b) indicates that the minimum surface roughness is at about 137 m/min, and 1.5 mm.

An ANOVA table is commonly used to summarize the tests performed. It was statistically studied the relative effect of each cutting parameters on the surface roughness ( $R_a$ ) by using ANOVA. The ANOVA table for response surface quadratic model for the surface roughness ( $R_a$ ) is given in Table 5.

The value of  $p$  is less than 0.05 indicates that the obtained model is considered to be statistically significant. Higher F value indicates that the variation of the process parameter makes a big changes on the surface roughness ( $R_a$ ). As seen in Table 5 cutting speed ( $v_c$ ) and feed rate ( $f$ ) is the most significant parameters, depth of cut ( $a_p$ ) is the least significant parameter. All the

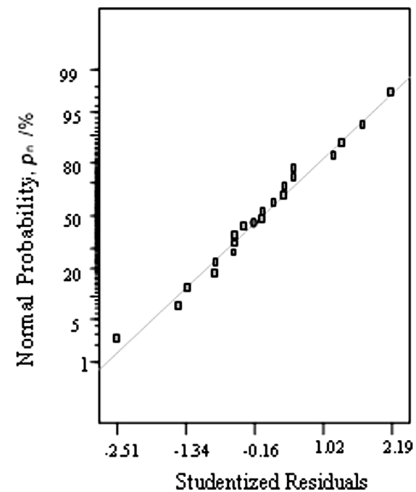


Figure 2: The normal probability plot of the residuals  
 Slika 2: Normalna verjetnost za rezidualne

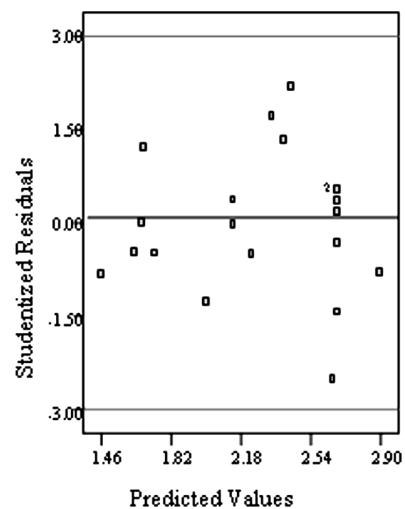


Figure 3: The standardized residual versus observation order plot  
 Slika 3: Standardni reziduali v odvisnosti od napovedanih vrednosti

squared terms and among interaction term cutting speed ( $v_c$ ) – feed rate ( $f$ ) and cutting speed ( $v_c$ ) – depth of cut ( $a_p$ ) appears to be highly significant.

We consider a measure of the model's overall performance referred to as the coefficient of determination and denoted by  $R^2$ . In the model,  $R^2$  is obtained equal to 95 %. The  $R^2$  value indicates that the cutting parameters explain 95 % of variance in surface roughness ( $R_a$ ). The normal probability plot of the residuals is shown in **Figure 2**.

The predicted values were found to be statistically similar to the actual measured values, based on the plotted probability plot. **Figure 2** shows that the residuals generally fall on a straight line implying that the errors are distributed normally. The standardized residual versus observation order plot, as shown in **Figure 3**. It shows that the model proposed is adequate.

After building the regression model, a numerical optimization technique using desirability functions can be used to optimize the response. The objective of optimization is to find the best settings that minimize a particular response<sup>12</sup>. **Table 6** shows five alternative solutions of the optimization approach used to determine the optimum processing conditions. A desirability value, where  $0 \leq d \leq 1$ . The value of  $d$  increases as the "desirability" of the corresponding response increases. The factor settings with maximum desirability are considered to be the optimal parameter conditions.

**Table 6:** Alternative solutions of optimum conditions

**Tabela 6:** Alternativne rešitve za optimalne pogoje

Solutions	Cutting speed $v_c$ / (m/min)	Feed rate $f$ / (mm/r)	Depth of cut $a_p$ / mm	$R_a$ / $\mu\text{m}$	Desirability (d)
1	137	0.3	1.5	1.46	0.957
2	47	0.1	0.5	1.63	0.835
3	137	0.26	1.5	1.64	0.830
4	47	0.1	1.5	2.00	0.580
5	137	0.3	0.67	2.10	0.509

**Table 6** revealed that highest desirability could be obtained at high level of cutting speed, feed rate and depth of cut. Five different desirable ranges of input parameters and response which gives high value of desirability are shown in the table. These are the optimal conditions to obtain high value of desirability. The achieved maximum desirability of 0.957 means that it is possible to meet surface roughness ( $R_a$ ) target. The lowest value of surface roughness ( $R_a$ ) obtained is  $R_a = 1.46\mu\text{m}$  at a cutting speed of  $v_c = 137$  m/min, a feed rate of  $f = 0.3$  mm/r and a depth of cut of  $a_p = 1.5$  mm.

#### 4 CONCLUSION

In this study, a quadratic model was developed for the prediction and analysis of the relationship between

the cutting parameters and surface roughness ( $R_a$ ) in turning process of AISI 4140 steel. It was observed that significance of the main variables is cutting speed ( $v_c$ ) and feed rate ( $f$ ). The comparisons of experimental results with the RSM predictions have been depicted in terms of percentage absolute error. In the prediction of surface roughness ( $R_a$ ) values the average absolute errors for RSM is found to be as 3.18 %. This value is sufficiently low to confirm the high predictive power of model. Experimental results show that, it can be inferred that prediction models can be applied to determine the appropriate cutting conditions, in order to achieve specific surface roughness ( $R_a$ ).

#### 5 REFERENCES

- Sahin Y, Motorcu AR. Surface roughness model for machining mild steel with coated carbide tool, *Materials&Design*, 26 (2005), 321–326
- Sahin Y, Motorcu AR. Surface roughness model in machining hardened steel with cubic boron nitride cutting tool, *Int. Journal of Refractory Metals&Hard Materials*, 26 (2008), 84–90
- Kopac J, Bahor M. Interaction of the technological history of a workpiece material and machining parameters on the desired quality of the surface roughness of a product, *Journal of Materials Processing Technology*, 92–93 (1999), 381–387
- Noordin MY, Venkatesh VC, Sharif S, Elting S, Abdullah A. Application of response surface methodology in describing the performance of coated carbide tools when turning AISI 1045 steel, *J.of Materials Processing Technology*, 145 (2004), 46–58
- Mansour A, Abdalla H, Meche F. Surface roughness model for end milling: a semi free cutting carbon casehardening steel (EN 32) in dry condition, *Journal of Materials Processing Technology*, 124 (2002), 183–191
- Arbizu I.P, Perez CJL. Surface roughness prediction by factorial design of experiments in turning processes, *Journal of Materials Processing Technology*, 143–144 (2003), 390–397
- Choudhury IA, El-Baradie MA. Surface roughness prediction in the turning of high strength steel by factorial design of experiments in turning processes, *Journal of Materials Processing Technology*, 67 (1997), 55–61
- Erzurumlu T, Oktem H. Comparison of response surface model with neural network in determining the surface quality of moulded parts, *Materials & Design*, 28 (2007), 459–465
- Ozel T, Karpat Y. Predictive modeling of surface roughness and tool wear in hard turning using regression and neural networks, *International Journal of Machine Tools & Manufacture*, 45 (2005), 467–479
- Nalbant M, Gokkaya H, Sur G. Application of Taguchi method in the optimization of cutting parameters for surface roughness in turning, *Materials&Design* (in press)
- Davim J.P. A note on the determination of optimal cutting conditions for surface finish obtained in turning using design of experiments, *Journal of Materials Processing Technology*, 116 (2001), 305–308
- Myers RH, Montgomery DC. *Response surface methodology: process and product optimization using designed experiments* NY: John Wiley & Sons Inc., 2002

## DETERMINATION OF OPTIMAL BALL BURNISHING PARAMETERS FOR SURFACE HARDNESS

### DOLOČITEV OPTIMALNIH PARAMETROV KROGLIČNEGA GLAJENJA ZA POVEČANJE TRDOTE POVRŠINE

**Aysun Sagbas, Funda Kahraman**

Mersin University, Tarsus Technical Education Faculty, Department of Mechanical Education, 33400, Tarsus-Mersin, Turkey  
asagbas@hotmail.com

*Prejem rokopisa – received: 2009-04-13; sprejem za objavo – accepted for publication: 2009-06-08*

The objective of this study is to improve surface hardness of 7178 aluminum alloy using the ball burnishing process. The effect of the main burnishing parameters on the objective function was examined using full factorial design and analysis of variance (ANOVA). The main parameters were found as burnishing force, feed rate and number of passes among four controllable factors that influence the surface hardness in ball burnishing process. Optimal ball burnishing parameters were determined after the experiments of the Taguchi's L9 orthogonal array. As result, the optimal burnishing parameters for surface hardness were the combination of the burnishing force at 200 N, number of passes at 4, feed rate at 0.25 mm/r.

**Key words:** Ball burnishing, surface hardness, Taguchi technique, factorial design, ANOVA

Cilj tega dela je bil povečati trdoto aluminijeve zalitine 7178 s krogličnim glajenjem. Vpliv glavnih parametrov glajenja na trdoto je bil opredeljen z uporabo polnega faktorialnega načrtovanja in analizo variance (ANOVA). Štirje glavni parametri glajenja, ki vplivajo na trdoto površine, so sila glajenja, hitrost podajanja in število prehodov. Optimalne parametre glajenja smo določili z ortogonalno razporeditvijo Taguchi L9. Končni rezultat so naslednji optimalni parametri: sila glajenja 200 N, število prehodov 4 in podajanje 0,25 mm/r.

**Ključne besede:** kroglično glajenje, trdota površine, Taguchijeva metoda, faktorialno načrtovanje, ANOVA

## 1 INTRODUCTION

The burnishing of metals is a cold-working process that leads to an accurate change on the surface profile of the workpiece by a minor amount of plastic deformation. In burnishing process, surface irregularities is redistributed without material loss<sup>1-2</sup>. The burnishing process gives many advantages in comparison with chip-removal processes. Burnishing increases the surface hardness of the workpiece, which in turn improves wear resistance, increases corrosion resistance, improves tensile strength, maintains dimensional stability and improves the fatigue strength by inducing residual compressive stresses in the surface of the workpiece<sup>3-6</sup>.

A survey of references shows that work on burnishing has been conducted by many researchers. Esme et al.<sup>7</sup> developed an artificial neural network model for the prediction surface roughness of AA 7075 aluminum alloy in ball burnishing process. Yan et al.<sup>8</sup> investigated the feasibility and optimization of a rotary electrical discharge machining with ball burnishing for inspecting the machinability of Al<sub>2</sub>O<sub>3</sub>/6061 Al composite using Taguchi method. Shiou and Chen<sup>9</sup> examined ball burnishing surface finish of a freeform surface plastic injection mold on a machining centre by using Taguchi techniques. Seemikery et al.<sup>10</sup> focused on the surface roughness, micro-hardness, surface integrity and fatigue life aspects of AISI 1045 work material using full factorial design of experiments. Hassan et al.<sup>11</sup> investigated

the effect of the burnishing force and number of passes on the surface roughness using Response Surface Methodology (RSM). El-Axir et al.<sup>12</sup> studied the surface finishing of 2014 aluminum alloy by using RSM with central composite design in ball burnishing process. El-Axir<sup>13</sup> determined the optimum combination of burnishing parameters to improve surface integrity for 6061 aluminum alloy applying a vertical milling machine using RSM with central composite design.

In this study, a factorial design and ANOVA were used to find out the effect of the main ball burnishing parameters. Taguchi's orthogonal array method was applied to determine the optimum levels of burnishing process parameters.

## 2 EXPERIMENTAL WORK

For experimental work, 7178 aluminum alloy was used as workpiece materials. Experiments were conducted on the different burnishing parameters and no coolant was used. The burnishing tool was mounted on tool holder of the CNC lathe. The workpiece was clamped by the three jaw chuck and tailstock centre of the machine. Three replications of each factor level combinations were conducted. Hardness measurements were made by using Zwick hardness tester.

The effect of several parameters can be determined efficiently with matrix experiments using factorial design and the analysis of variances was employed to

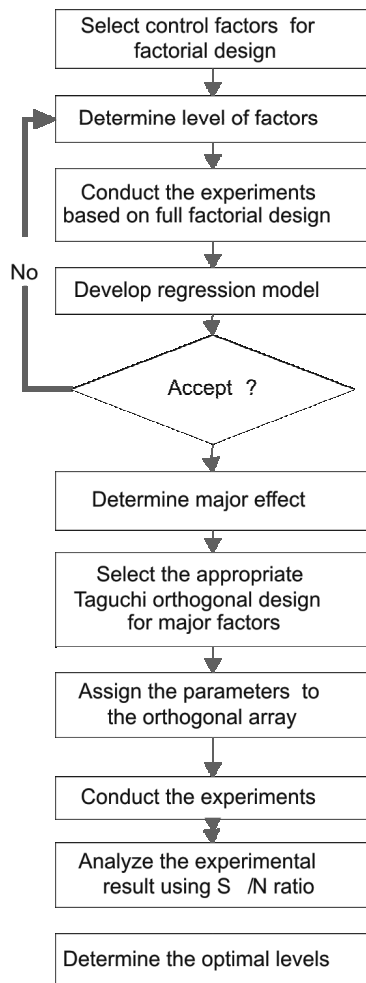


**Figure 1:** A flowchart of proposed methods  
**Slika 1:** Potek uporabljenih metod

find the significance of the factor effects. Taguchi’s design method was applied to determine the optimal levels of burnishing process. A flowchart of proposed methods is shown in **Figure 1**.

The level of the factorial design is shown in **Table 1**. Two levels of control factors are referred to as low and high. Twenty experiments constitute the  $2^4$  factorial design with an added centre point repeated four times. Surface hardness was taken as output variable and burnishing force, burnishing speed, feed rate and number of passes were taken as input parameters for maximizing the surface hardness of the 7178 aluminum alloy.

**Table 1:** Levels of the factors for factorial design  
**Tabela 1:** Nivoji faktorjev za faktorialno načrtovanje

Factors/Levels	Low (-1)	Centre (0)	High (+1)
Burnishing force/N	100	150	200
Speed/mm/min	33	52	71
Number of passes	2	3	4
Feed rate/mm/r	0,25	0,35	0,45

The Taguchi design concept a L9 mixed orthogonal arrays table was selected to conduct the matrix experi-

ments for four level factors of ball burnishing process and designated in **Table 2**.

**Table 2:** Factors and levels for Taguchi design  
**Tabela 2:** Faktorji in nivoji za Taguchijevo načrtovanje

Factors/Levels	1	2	3
Burnishing force/N	100	150	200
Number of passes	2	3	4
Feed rate/ mm/r	0.25	0.35	0.45

The optimization of the engineering design problems can be divided into the smaller-the better type, the nominal-the best type, the larger-the better type. The signal-to-noise (S/N) ratio is used as objective function for optimizing the product or process design <sup>14</sup>. The S/N ratio was chosen according to the criterion the-larger-the-better, in order to maximize the response. Based on the Taguchi method, S/N ratio is defined by the Equation 1.

$$\eta_j = -10 \lg \frac{1}{n} \sum_{i=1}^n \frac{1}{y_i^2} \quad (1)$$

where:  $n$  is the number of experiment,  $y_i$  is the observations of the quality characteristic,  $\eta_j$  is the S/N ratio.

The optimization strategy of the larger the better problem is to maximize  $\eta$  defined with Equation 1. The levels that maximize  $\eta$  will be selected for the factors that have a significant effect on  $\eta$  and the optimal conditions for ball burnishing can then be determined. The predicted  $\eta_{opt}$  under optimal conditions could be calculated by using Equation 2

$$\eta_{opt} = m + \sum (m_i - m) \quad (2)$$

where:  $\eta_{opt}$  is the S/N ratio under the optimum conditions,  $m$  is the overall mean value of  $\eta$  for the experimental region,  $m_i$  is the  $\eta$  under optimal condition.

### 3 RESULTS AND DISCUSSION

The effect of selected process parameters on the surface hardness of aluminum alloy have been determined by using  $2^4$  full factorial design. ANOVA was employed to find the significance of the factor effects based on a 95 % confidence level. The ANOVA results are shown in **Table 3**.

The ANOVA table shows that, the most significant factors are the burnishing force and the number of passes, respectively, while feed rate is the less significant parameter of the ball burnishing process.

The optimum burnishing parameter combination was obtained by using Taguchi design and analysis of S/N ratio. **Table 4** shows experimental measurements made using the L9 orthogonal array based on the Taguchi method. Also, the S/N ratios were considered to evaluate the effect of burnishing parameters. The mean S/N ratio for each level of burnishing parameters is summarized in **Table 5** and it is shown graphically in **Figure 2**.

**Table 3:** The ANOVA results  
**Tabela 3:** Rezultati ANOVA

Factor	SS	df	MS	F	P
Model	2740.	10	274.0	5.9	0.020
A	1242	1	1242.	26.	0.002
B	663.0	1	663.0	14.	0.009
C	333.0	1	333.0	7.1	0.036
D	52.56	1	52.56	1.1	0.328
AB	27.56	1	27.56	0.5	0.470
AC	45.56	1	45.56	0.9	0.359
AD	68.06	1	68.06	1.4	0.271
BC	33.06	1	33.06	0.7	0.430
BD	264.0	1	264.0	5.6	0.054
CD	10.56	1	10.56	0.2	0.650
Residual	278.3	6	46.39		
Pure error	4.50	1	4.50		
Cor total	3477	17			

A: Force, B: Speed, C: Number of passes, D: Feed rate  
SS: Sum of square, df: Degrees of freedom, MS: Mean square

**Table 4:** Experimental results for surface hardness

**Tabela 4:** Rezultati preizkusov za trdoto površine

Experiment No	Burnishing Force/N	Number of passes	Feed rate/mm/r	Surface hardness HV
1	100	2	0.25	167
2	100	3	0.35	170
3	100	4	0.45	179
4	150	2	0.45	175
5	150	3	0.25	179
6	150	4	0.35	181
7	200	2	0.35	178
8	200	3	0.45	192
9	200	4	0.25	202

**Table 5:** Mean S/N ratios for surface hardness

**Tabela 5:** Povprečna razmerja za trdoto površine

Factors/Levels	1	2	3
Burnishing Force	44.43	45.00	45.56
Number of passes	44.73	45.13	45.37
Feed rate	45.19	44.88	45.17

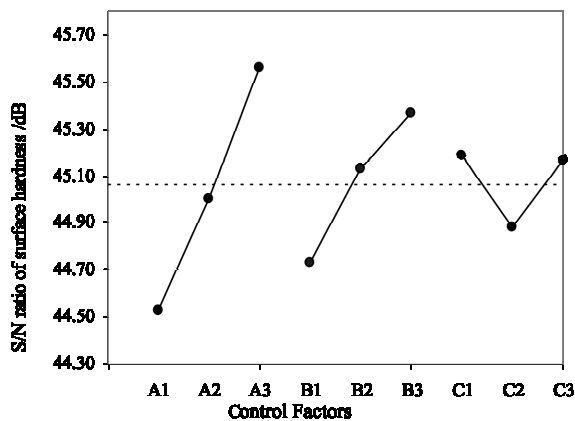


**Figure 2:** Plots of control factor effects

**Slika 2:** Grafični prikaz vpliva kontrolnih dejavnikov

The confirmation experiment was conducted at the optimum setting of the process parameters. The results of the confirmation experiment for surface hardness is given in **Table 6**.

**Tabela 6:** Rezultati potrditvenega preizkusa

**Table 6:** Results of the confirmation experiment

Level	Initial setup	Optimal condition	
		Prediction	Experiment
Hardness	A2B2C2	A3B3C1	A3B3C1
S/N ratio	175 HV	45.79 dB	202 HV
	44.89 dB	45.79 dB	46.00 dB

The estimated S/N ratio using the optimal burnishing parameters for surface hardness was calculated using Equation 2. The predicted S/N ratio (45.79) is very close to the experimental S/N ratio (46.00) under optimal burnishing conditions. Based on the result of the confirmation test, the surface hardness is increased for 1.15 times.

#### 4 CONCLUSIONS

In this experimental study, the effect "of the ball burnishing" parameters on surface hardness was examined and optimal settings of the ball burnishing parameters were obtained. The effect of several parameters can be determined efficiently with matrix experiments using factorial design. The main parameters were found as burnishing force, feed rate and number of passes among four controllable factors that affect the surface hardness in ball burnishing process. The burnishing force is the dominant factor, while, the number of passes is a major factor. The optimal burnishing parameters were determined with the Taguchi's L9 matrix experiments. The optimal parameter combination for the maximum surface hardness was obtained by using the analysis of S/N ratio. The optimal combination of experimental parameters for each factor is A3B3C1. As result, the optimal parameters for surface hardness were as follows: burnishing force at 200 N, number of passes at 4, feed rate at 0.25 mm/r.

#### 5 REFERENCES

- A. M. Hassan, Burnishing force and number of ball passes for the optimum surface finish of brass components, *Journal of Materials Processing Technology* 72 (1997), 385–391
- H. Luo, L. Wang, C. Zhang, Study on the aluminum alloy burnishing processing and the existence of the outstripping phenomenon, *J. of Materials Processing Technology*, 116 (2001), 88–90
- B. C. Yeldose, B. Ramamoorthy, An investigation into the high performance of tin-coated rollers in burnishing process, *Journal of Materials Processing Technology*, 207 (2008), 350–355
- F. J. Shiou, C. H. Chen, Determination of optimal ball burnishing parameters for plastic injection moulding steel, *Int. J. Adv. Manufacturing Technology* 3 (2003), 177–185

- <sup>5</sup>L. Luca, I. Ventzel-Marinescu, Effects of working parameters on surface finish in ball-burnishing of hardened steels, *Precision Engineering*, 29 (2005), 253–256
- <sup>6</sup>N. H. Loh, S. C. Tam, S. Miyazawa, A study of the effects of ball burnishing parameters on surface roughness using factorial design, *Journal of Mechanical Working Technology*, 18 (1989), 53–61
- <sup>7</sup>U. Esme, A. Sagbas, F. Kahraman, M. K. Kulekci, Use of ANN in ball burnishing process for the prediction of surface roughness of AA 7075 aluminum alloy, *Mater. Tehnol.*, 42 (2008), 215–219
- <sup>8</sup>B. H. Yan, C. C. Wang, H. M. Chow, Y. C. Lin, Feasibility study of rotary electrical discharge machining with ball burnishing for Al<sub>2</sub>O<sub>3</sub>/6061 Al Composite, *Int. J. of Machine Tools & Manufacture*, 40 (2000), 1403–1421
- <sup>9</sup>F. J. Shiou., C. H. Chen, Freeform Surface Finish of Plastic Injection Mold by Using Ball-Burnishing Process, *J. of Materials Processing Technology*, 140 (2003), 248–254
- <sup>10</sup>C. Y. Seemikery, P. K. Brahmanekar, S. B. Mahagaonkar, Investigation on surface integrity of AISI 1045 Using LPB Tool, *Tribology International*, 41 (2008), 724–734
- <sup>11</sup>A. M. Hassan, H. F. Al-Jalil, A. A. Ebied, Burnishing force and number of passes for the optimum surface finish of brass components, *Journal of Materials Processing Technology*, 83 (1998), 176–179
- <sup>12</sup>M. H. El-Axir, O. M. Othman, A. M. Abodiena, Study on the inner surface finishing of aluminum alloy 2014 by ball burnishing process, *J. of Materials Processing Technology* 202 (2008), 435–442
- <sup>13</sup>M. H. El-Axir, An investigation in roller burnishing, *Int. Journal of Machine Tools & Manufacture*, 40 (2000), 1603–1617
- <sup>14</sup>D. C. Montgomery, *Design and analysis of experiments*, John Wiley & Sons, Inc., NY, 1997